Development of a Rigorous and Efficient Electromagnetic Simulation Algorithm for 3-D Printed Structures in Multilayer Environment

by

Tayyar ÖNAL

A Thesis Submitted to the
Graduate School of Engineering
in Partial Fulfillment of the Requirements for
the Degree of

Master of Science

in

Electrical & Computer Engineering

Koç University

October 2005

Koç University

Graduate School of Sciences and Engineering

This is to certify that I have examined this copy of a master's thesis by

Tayyar ÖNAL

and have found that it is complete and satisfactory in all respects,
and that any and all revisions required by the final
examining committee have been made.

Committee Members:

_____

Prof. M. İrşadi Aksun (Advisor)

_____

Assistant Prof. Alper Demir

_____

Assistant Prof. Vakur B. Ertürk

Date: _____

ABSTRACT

Development of a Rigorous and Efficient Electromagnetic Simulation Algorithm for 3-D Printed Structures in Multilayer Environment

An efficient and rigorous electromagnetic simulation algorithm, based on the method of moments in conjunction with discrete complex image method (MoM-DCIM), is developed for printed structures with multiple vertical conductors extending through multilayer media. As this approach, MoM-DCIM, has already proved to be very efficient to analyze printed structures with only horizontal conductors in multilayer environment, and with horizontal and vertical conductors in single-layer media, it is extended to more general geometries with horizontal conductors and vertical conductors spanning more than one layer. Moreover, the algorithm developed in this thesis is possibly the most efficient approach to handle printed circuits with multiple vertical conductors, spanning one or more layers. Efficiency in this context refers to handling multiple vertical conductors with almost no filling cost of the MoM matrix, provided all vertical conductors have the same dependence in the vertical direction. Since the efficiency in this sense can be considered more like a by-product of employing MoM-DCIM in such structures, the proposed algorithm is presented emphasizing the steps that facilitate such an efficient implementation of multiple vertical conductors. Some realistic circuits and planar antennas, with and without multiple vertical strips are analyzed, and results are compared to those presented in the literature and obtained from the commercial software *em* by SONNET to validate the algorithm. To assess the efficiency of the proposed algorithm with additional vertical conductors, computational cost in terms of CPU time is provided as a function of additional number of vertical conductors. It is observed that additional vertical conductors have almost negligible computational cost over that of already calculated MoM matrix entries for a single vertical conductor.

Keywords: Method of Moments, 3-D Printed Structures, Vertical Conductors, Closed-Form Green's Functions, DCIM

ÖZET

Çok Katmanlı Ortamlarda 3-Boyutlu Baskılı Yapılar için Doğru ve Verimli Elektromanyetik Benzetim Algoritmasının Geliştirilmesi

Çok katmanlı ortamlarda çoklu düşey iletkenli baskılı devreler için ayrık kompleks görüntü metodu ile ilişkili moment metodu (MoM-DCIM) kullanan verimli ve doğru bir elektromanyetik benzetim algoritması geliştirilmiştir. Bu yaklaşımın yatay ve düşey iletkenler içeren tek katmanlı ortamlar ile sadece yatay iletkenler içeren çok katmanlı ortamlardaki baskılı devrelerin analizinde oldukça verimli olduğu daha önce kanıtlandığı için, bu yaklaşım birden çok katmanları kapsayan yatay ve düşey iletkenli daha genel geometriler için genişletilmiştir. Bununla birlikte, bir veya daha çok katmanları kapsayan çoklu düşey iletkenli baskılı devrelerin analizinde bu tezde geliştirilen algoritma muhtemelen en verimli yaklaşımdır. Bu bağlam içinde verimlilik, çoklu düşey iletkenlerin analizinin MoM matrisinin doldurulmasına hemen hiçbir maliyet getirmemesine işaret etmektedir. Verilen bütün düşey iletkenler dikey doğrultuda aynı bağımlılıktadır. Verimliliğin daha çok MoM-DCIM kullanımının yan ürünü olduğu düşünüldüğünden, çoklu düşey iletkenlerin verimli bir şekilde uygulanmasını kolaylaştıran aşamalar vurgulanarak önerilen algoritma sunulmuştur. Algoritmayı doğrulamak amacıyla, çoklu düşey şeritler de içeren bazı gerçekçi devreler ve düzlemsel antenler analiz edilmiş, ve elde edilen sonuçlar literatürde sunulan ve ticari olarak kullanılan *em*-SONNET yazılımının sonuçları ile karşılaştırılmıştır. Önerilen algoritmanın verimliliğinin eklenen düşey iletkenlere bağlı olarak değerlendirilmesi amacıyla, ana işlem birimi (CPU) zamanı açısından hesaplama maliyeti eklenen düşey iletken sayısının bir fonksiyonu olarak verilmiştir. Eklenen düşey iletkenlerin, hali hazırda tek bir düşey iletken için hesaplanmış olan MoM matris elemanlarına ek olarak ihmal edilebilecek bir hesap maliyeti getirdiği gözlenmiştir.

Anahtar Kelimeler: Moment Metodu, 3-Boyutlu Baskılı Yapılar, Düşey İletkenler, Kapalı Form Green Fonksiyonları, Ayrık Kompleks Görüntü Metodu

ACKNOWLEDGEMENTS

I would like to express my deepest gratitude to Prof. M. I. Aksun for his supervision, encouragement and time spent in all steps of the development of this work.

My special thanks are due to Dr. Noyan Kınayman whose helpful discussions and materials made the initiation and development of this work possible.

Many thanks to Pınar Karabulut, Turgut Öktem, Uğur Güner, Burak Öztürk, Ulaş Bağcı, Emrah Akyol, Salih Ertürk and Eray Cumbul for their friendship and support. I also would like to thank to undergraduate assistants Fatih Noyan and Umur Arpacı who gave me a great moral support during my studies.

Finally, my sincere thanks go to my family for their endless love and patience throughout my whole life.

TABLE OF CONTENTS

LIST OF TABLES

LIST OF FIGURES

NOMENCLATURE

CAD	Computer Aided Design
CPU	Central Processing Unit
DCIM	Discrete Complex Image Method
EFIE	Electric Field Integral Equation
EM	Electromagnetic
FEM	Finite Element Method
FTDT	Finite-Difference Time Domain
GPOF	Generalized Pencil of Functions
HED	Horizontal Electric Dipole
HMD	Horizontal Magnetic Dipole
LU	Lower Upper
MMIC	Monolithic Microwave Integrated Circuits
MoM	Method of Moments
MPIE	Mixed Potential Integral Equation
MFIE	Magnetic Field Integral Equation
ORGE	Order Recursive Gaussian Elimination
PEC	Perfect Electric Conductor
PIFA	Planar Inverted “F” Antenna
SIP	Sommerfeld Integral Path
TE	Transverse Electric
TM	Transverse Magnetic
VED	Vertical Electric Dipole
VMD	Vertical Magnetic Dipole

Chapter 1

Introduction

During the last three decades, the use of printed geometries has been increasing steadily, especially in the applications of antennas and monolithic microwave integrated circuits (MMIC) [1–6]. This increase can be attributed partially to the physical features of printed structures, such as, lightweight and conformable, and partially to the cost of the products (circuits), as printed circuits are cheaper to produce, easy to manufacture circuits with good reproducibility at low cost. In addition, as recent developments in communication technologies have led to circuits with smaller dimensions and complex functional operations, the use of printed circuits with vertical metallizations in layered media has become quite popular to achieve these goals [7, 8]. Since circuits distributed over multilayer environment need vertical conductors to facilitate the connectively between the layers, vertical metallizations like via holes in MMICs, shorting strips and probe feeds in microstrip antennas, have become the integral parts of high frequency circuits and/or multifunction antennas. As a result, with the use of vertical conductors, one of the major advantages of printed circuits, cited above as ”ease to manufacture”, may have to be sacrificed to achieve the goals of multi-function operations and/or miniaturization. This burden can partially be alleviated with a CAD tool that helps to analyze and design such circuits with accuracy and ease. Therefore, parallel to such fabrication requirements of real circuits, simulation tools need to be developed to efficiently and accurately design printed circuits with vertical conductors.

Plenty of methods have been proposed to analyze printed circuits; some are tuned for some specific class of printed geometries, some are rigorous enough but not computationally efficient, and some others are approximate but very efficient. These methods can be mainly classified into two groups: i) approximate but numerically efficient methods like quasi-static methods [9–11]; ii) accurate but computationally expensive methods, such as the method of moments (MoM) [12, 13], the finite-difference time domain (FDTD) method [14] and the finite element method (FEM) [15]. Although both FEM and FDTD methods are quite general and versatile, and the resulting matrices are sparse, it is widely accepted that the MoM based algorithms are the most suitable and efficient approaches for the rigorous analysis of layered printed structures [16–19]. Therefore, the main numerical technique employed in this work is based on the MoM, which, in essence, transforms an operator equation (differential, integral or integro-differential form) describing a physical problem into a matrix equation.

The MoM in EM problems is usually employed for the solution of an integral equation, which could be electric field, magnetic field or mixed potential integral equations (MPIE). Since the singularities of the Green's functions for the electric and magnetic fields are stronger than those of the vector and scalar potentials, the use of MPIE in conjunction with the spatial-domain MoM has been the preferred choice for the characterization of planar printed geometries in general [20–22]. In addition, with the introduction of an efficient approximation of the spatial-domain Green's functions for vector and scalar potentials in closed forms (also referred to as DCIM) [23], and with its improved versions [24–26], the computational efficiency of the spatial-domain MoM for the solution of MPIE for printed geometries has been significantly improved [27, 28]. Note that the DCIM provides only approximations of Green's functions in terms of complex exponentials, and hence, as it is the case for most approximation methods, it is only valid over a limited range in certain cases, depending upon the implementation of the method [29]. Further improvement in the efficiency of the solution of MPIE via MoM-DCIM combination was achieved when the MoM matrix entries, which are double integrals defined over the surface of conductors, were

evaluated analytically [30]. These improvements, when combined properly, make the algorithm very robust, rendering the method to become a powerful candidate for a general computer aided design (CAD) software for printed circuits in a planar multilayer environment [31]. Although the above review of MoM-DCIM covers its application for the analysis of printed circuits with only horizontal conductors, it has also been studied and applied to more general printed structures. An efficient formulation how to handle vertical conductors within this approach was first proposed in [32], and extended for and applied to more general geometries [35]. Meanwhile, applications of MoM-DCIM to vertical probes and to probe-fed patch antennas in layered media were proposed following a different approach [33,34]. In search for a more efficient approach for the analysis of general printed structures, in the context of MoM-DCIM, there have been some significant contributions recently [36–38]. Although it was recognized that the algorithm proposed in [35] could be extended to analyze multiple vertical metallizations very efficiently, there has been no study so far on this important issue. In this thesis, to validate the assessment, the algorithm proposed in [35] is extended to handle multiple vertical conductors, possible spanning more than one layer, very efficiently. To emphasize the contribution of the thesis, it should be stated that the method proposed here has two main contributions: i) efficient simulation of multiple vertical conductors, with almost no fill-in cost of the MoM matrix in addition to that for the same horizontal geometry with one vertical metallization; and ii) being able to handle vertical conductors extending over multiple planar layers. Efficiency concept here needs to be further emphasized that once one vertical metallization is introduced into a printed structure and analyzed using the proposed method, the computational cost of additional vertical conductors with the same length becomes almost negligible. Therefore, optimization of number and positions of vertical metallizations for predefined goals, such as dual polarization, multiple bands of operation in the case of antenna design, and low spurious radiation in the case of microwave circuits, can now be achieved very efficiently without sacrificing from the accuracy of the method.

Since the main method used throughout the thesis is the MoM in conjunction with the closed-form Green's functions to solve for MPIE, it would be instructive to show how to derive MPIE and Green's functions in spectral and spatial domains in multilayer planar environment in Chapter 2. Then, in Chapter 3, the implementation of spatial-domain MoM for the analysis of printed circuits over single-layer planar media is briefly introduced, and methods used to extract the network parameters are discussed, along with some numerical examples. In Chapter 4, the original method proposed in [35] is extended for the analysis of printed structures with vertical conductors spanning more than one layer, and it is tested over some examples. Moreover, the results are compared to those obtained from the commercial software *em* by SONNET, and to experimental results provided in the literature. This is followed, in Chapter 5, by the discussion and demonstrations of the efficiency of the method when multiple vertical conductors are used in some intuitive and realistic examples. Finally, conclusions are provided in Chapter 6.

Chapter 2

Theory – MPIE and Green's Functions

This chapter and the following chapter aim to provide a brief introduction to the background materials of the numerical technique used throughout this thesis, for the analysis of printed structures with multiple vertical strips in a multilayer planar environment. As the choice of the numerical method for such structures has been the spatial-domain MoM for the solution of MPIE, whose derivation requires a priori knowledge of Green's functions, this chapter concentrates on the derivation of MPIE, and on the derivation of Green's functions in multilayered planar structures. The MPIE is obtained by writing the electric field in terms of vector and scalar potentials, which are written as convolution integrals of Green's functions and the current density. Because the current density is the unknown function to be determined, and because it is under the convolution integral, the equation is called the integral equation, whose solution can be obtained by the MoM procedure. Once the current density is obtained as a result of the application of MoM, other circuit parameters, like impedance and scattering parameters, and the input impedance, can easily be computed from the current density.

It should be noted that the choice of MPIE as the governing equation for printed structures in multilayer planar environment is based on two facts: i) Green's functions involved with the MPIE is less singular that the ones involved in electric field integral equation (EFIE) and magnetic field integral equation (MFIE); and as a result of this ii) the Green's functions of the vector and scalar potentials can be cast into closed forms via the discrete complex image method (DCIM). Therefore, after a brief introduction of the MPIE, the main body of the chapter is dedicated to the derivation of the Green's functions in the

spectral domain, as analytical expressions, and of their spatial-domain counterparts as closed-form approximations.

2.1 Mixed-Potential Integral Equation Formulation

For the sake of illustration, a general 3-D microstrip structure in a multilayer environment is considered, as shown in Fig. 2.1. It is assumed that all layers and ground plane extend to infinity in the transverse directions and the conductors are lossless and infinitesimally thin. The permittivity and the thickness of *i*-th layer are represented by ε_i and d_i, respectively.

The MPIE formulation begins with writing the electric field in terms of scalar and vector potentials, ϕ and **A**, respectively, as

$$\mathbf{E} = -j\omega\mathbf{A} - \nabla\phi \tag{2.1}$$

where the potentials can be expressed in terms of surface current density **J** and the charge density ρ as convolution integrals:

$$\mathbf{A} = \overline{\mathbf{G}}^{A} * \mathbf{J} \tag{2.2}$$

$$\phi = G^{q} * \rho = G^{q} * \left(\frac{-1}{j\omega} \nabla \cdot \mathbf{J} \right) \tag{2.3}$$

Note that $*$ denotes the convolution integral, and the Green's function for the vector potential $\overline{\mathbf{G}}^{A}$ is in dyadic form, whereas the Green's function of the scalar potential G^q is a scalar function. In addition, since the printed structure is three-dimensional, the surface current density defined over conductors needs to be written as a three-dimensional vector $\mathbf{J} = J_x\hat{x} + J_y\hat{y} + J_z\hat{z}$. Substituting (2.2) and (2.3) in (2.1) results in the governing equation, known as MPIE, and the components of the electric field can be written explicitly as follows:

$$E_x = -j\omega G_{xx}^{A} * J_x + \frac{1}{j\omega}\frac{\partial}{\partial x}\left(G^{q} * \nabla \cdot \mathbf{J}\right) \tag{2.4}$$

$$E_y = -j\omega G_{yy}^{A} * J_y + \frac{1}{j\omega}\frac{\partial}{\partial y}\left(G^{q} * \nabla \cdot \mathbf{J}\right) \tag{2.5}$$

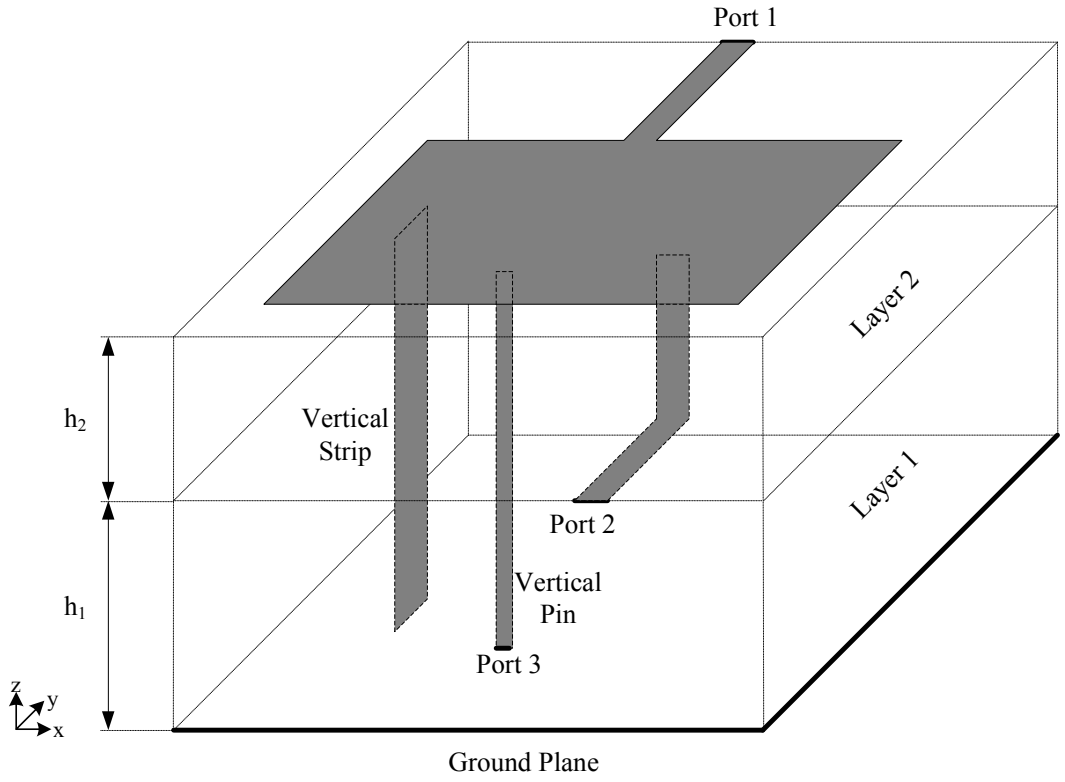

Figure 2.1: A typical 3-D multilayer microstrip structure

$$E_z = -j\omega G_{zx}^A * J_x - j\omega G_{zy}^A * J_y - j\omega G_{zz}^A * J_z + \frac{1}{j\omega}\frac{\partial}{\partial z}\left(G^q * \nabla \cdot \mathbf{J}\right) \tag{2.6}$$

where $\overline{\mathbf{G}}^{\mathbf{A}} = G_{xx}^A \hat{x}\hat{x} + G_{yy}^A \hat{y}\hat{y} + G_{zz}^A \hat{z}\hat{z} + G_{zx}^A \hat{z}\hat{x} + G_{zy}^A \hat{z}\hat{y}$ with $G_{xx}^A = G_{yy}^A$ is employed, with the corresponding two different Green's functions for the scalar potential due to horizontal and vertical dipoles in layered media. Note that the choice of the vector components of the Green's function is not unique in layered media, and this choice employed throughout the thesis is known as the traditional form [39]. The term G_{ij}^A represents the *i*-directed vector potential at **r** due to a *j*-directed electric dipole of unit strength located at $\mathbf{r}'$, and the term G^q is the scalar potential of a unit point charge associated with an electric dipole. As mentioned above, the Green's function of the scalar potential is not unique for horizontal and vertical

electric dipoles in the traditional form, therefore, the terms involving the Green's function of the scalar potential in (2.4)-(2.6) can be explicitly written as

$$G^q * \nabla \cdot \mathbf{J} = G_x^q * \frac{\partial J_x}{\partial x} + G_y^q * \frac{\partial J_y}{\partial y} + G_z^q * \frac{\partial J_z}{\partial z} \tag{2.7}$$

where $G_x^q (= G_y^q)$ and G_z^q denote the Green's functions of the scalar potential for a horizontal and vertical electric dipoles, respectively. Once the spatial-domain Green's functions are obtained, equations (2.4)-(2.6) have become the MPIE to be solved for the current density.

2.2 Green's Functions in Planarly Layered Media

As it is obvious from (2.4)-(2.6), the application of MoM for the solution of MPIE requires the spatial-domain Green's functions, which can be obtained by two-dimensional inverse Fourier transform or by one-dimensional inverse Hankel transform of their spectral-domain representations [25,40]. Although the spectral-domain Green's functions are obtained analytically for planar layered media, their inverse transform integrations, generally known as Sommerfeld integrals [41], are usually computationally very expensive due to the oscillatory nature of the kernel and the integrands.

Recently, discrete complex image method (DCIM) has been proposed to overcome this inefficiency problem in the calculation of the spatial-domain Green's functions by approximating the spectral-domain Green's functions in terms of complex exponentials [23]. Hankel transforms can be evaluated analytically for these exponentials and thus the spatial-domain Green's functions can be written in closed forms. The key point of this approach is the numerical method for the exponential approximation of the spectral-domain Green's functions, which can be performed by using the techniques such as the original Prony method [23], least square Prony method [24] or the generalized pencil of function (GPOF) method [25]. Approximation with the original Prony method was limited to thick and single layer structures due to its inadequacy. Although the least square Prony method eliminated this problem and the GPOF method further improved this approximation in the sense of

robustness and noise sensitivity, the algorithm for the exponential approximation was still computationally expensive, because all these methods require the uniform sampling of a complex-valued function along a real variable. Uniform sampling of a function with local oscillations and fast variations, like spectral-domain Green's functions, may result in taking a large number of samples. Consequently, restriction in the sampling process and decision on other approximation parameters such as maximum value of the sampling range, render the algorithm not robust and computationally expensive. Recently, to eliminate the deficiencies in numerical implementation of the exponential approximation, a more robust and efficient approach has been proposed to accomplish a piecewise uniform sampling over two or multiple consecutive regions of the approximation domain, which are two-level and multi-level sampling algorithms, respectively [26,42]. In this thesis, two-level and three-level sampling algorithms are employed in the derivation of closed-form Green's functions and for the spectral-domain functions to be transformed.

In Section 2.2.1, the spectral-domain Green's functions are introduced for planarly layered media and modifications in multilayer media are demonstrated in detail. Then, in Section 2.2.2, the method for obtaining the closed-form spatial-domain Green's functions is described.

2.2.1 Spectral-Domain Green's Functions

A general planar stratified medium is shown in Fig. 2.2, where a dipole current source, like horizontal electric dipole (HED), horizontal magnetic dipole (HMD), vertical electric dipole (VED) or vertical magnetic dipole (VMD), is assumed to be placed in layer-*i* and its fields are observed in any layer including the source layer. It is assumed that all layers extend to infinity in the horizontal plane, and the thickness, relative permittivity and the relative permeability of *i*-th layer are denoted by d_i, ε_i and μ_i, respectively. Note that layers are stratified in *z*-direction and the time convention of $e^{j\omega t}$ has been adopted and suppressed throughout the thesis.

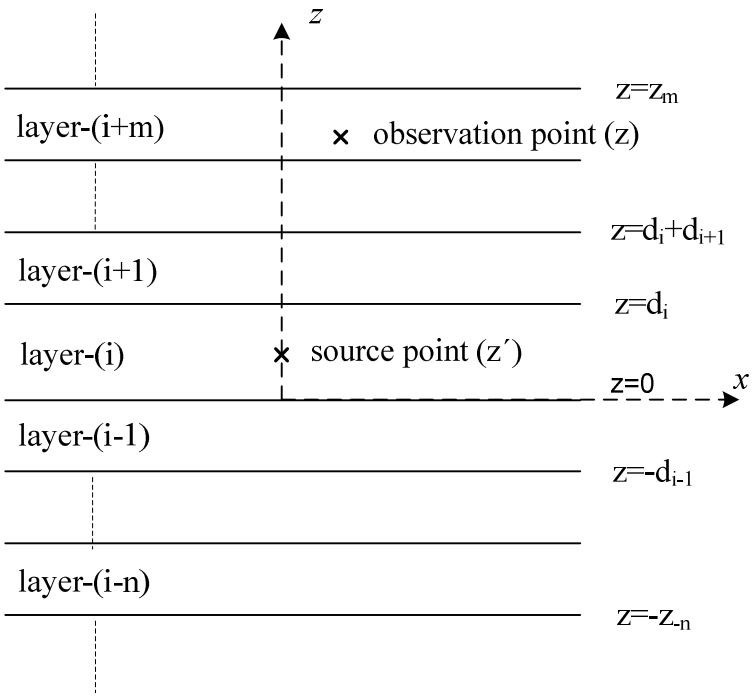

Figure 2.2: A general multilayer medium

Since the electric and magnetic fields can be written in terms of vector and scalar potentials, the Green's functions for these fields can also be obtained using the same relations from the Green's function of potentials. Therefore, for the sake of coherence of the discussion, the expressions of the electric field, (2.8), magnetic field, (2.9) and the Lorentz gauge, (2.10), are written as

$$\mathbf{E}(\mathbf{r}) = -j\omega\,\mathbf{A}(\mathbf{r}) - \nabla\phi(\mathbf{r}) \tag{2.8}$$

$$\mu\,\mathbf{H}(\mathbf{r}) = \nabla \times \mathbf{A}(\mathbf{r}) \tag{2.9}$$

$$\nabla \cdot \mathbf{A}(\mathbf{r}) = -j\omega\varepsilon\mu\,\phi(\mathbf{r}) \tag{2.10}$$

in a medium characterized by ε and μ. Substituting the scalar potential expression in terms of vector potential from the Lorentz gauge (2.10) into the electric field expression (2.8), electric field is written in terms of the vector potential as

$$\mathbf{E}(\mathbf{r}) = -j\omega\left[\bar{\mathbf{I}} + \frac{\nabla\nabla}{k^2}\right]\cdot\mathbf{A}(\mathbf{r}) \tag{2.11}$$

where $\bar{\mathbf{I}}(=\hat{x}\hat{x}+\hat{y}\hat{y}+\hat{z}\hat{z})$ is a unit dyad, and $k=\omega\sqrt{\mu\varepsilon}$ is the wave number of the medium. For an electric current dipole oriented in an arbitrary direction $\hat{\alpha}$, represented as $\mathbf{J}=\hat{\alpha}Il\,\delta(\mathbf{r}-\mathbf{r}')$, the vector potential in a homogenous and unbounded medium can be written as

$$\mathbf{A}(\mathbf{r},\mathbf{r}') = \hat{\alpha}\mu Il\frac{e^{-jk|\mathbf{r}-\mathbf{r}'|}}{4\pi|\mathbf{r}-\mathbf{r}'|} \tag{2.12}$$

where the scalar Green's function is convolved with the source term. Hence, substituting (2.12) into (2.11) and (2.9) yields the electric and magnetic fields in a homogenous and unbounded medium as

$$\mathbf{E}(\mathbf{r}) = -j\omega\left[\bar{\mathbf{I}} + \frac{\nabla\nabla}{k^2}\right]\cdot\hat{\alpha}\mu Il\frac{e^{-jk|\mathbf{r}-\mathbf{r}'|}}{4\pi|\mathbf{r}-\mathbf{r}'|} \tag{2.13}$$

$$\mathbf{H}(\mathbf{r}) = \nabla\times\hat{\alpha}Il\frac{e^{-jk|\mathbf{r}-\mathbf{r}'|}}{4\pi|\mathbf{r}-\mathbf{r}'|} \tag{2.14}$$

In cases of multilayer media, the spherical wave terms (e^{-jkr}/r) in the expressions must be modified in order to take the reflections from the layers below and above into account. The spherical wave terms can be written in terms of plane waves, by using the Weyl identity, as

$$\frac{e^{-jk|\mathbf{r}-\mathbf{r}'|}}{|\mathbf{r}-\mathbf{r}'|} = \frac{1}{\pi}\int_{-\infty}^{\infty}\int_{-\infty}^{\infty} dk_x dk_y\, e^{-jk_x(x-x')-jk_y(y-y')}\frac{e^{-jk_z|z-z'|}}{j2k_z} \tag{2.15}$$

where $k_x^2+k_y^2+k_z^2$. Once the plane wave constituents of spherical waves are explicitly written in the field expressions, TE and TM wave components in a planar stratified medium, extending infinity on *xy*-plane as shown in Fig. 2.2, can easily be extracted for the field

expressions. Therefore, starting with Fresnel's reflection and transmission coefficients for TE and TM waves, one can derive generalized reflection and transmission coefficients, and, in turn, can find the fields due to a point source in any layer. Because the fields are translational invariant on *xy*-plane, and because they have to satisfy phase matching condition at the interfaces in layered media, the propagation constants k_x and k_y have to be same in all layers. The derivation of spectral-domain Green's functions is detailed in the following sub-sections, for the sake of completeness, for an HED and VED in a planar multilayer structure depicted in Fig. 2.2. In the following discussions, the source is assumed to be located in layer-*i*, the origin of the coordinate system is set to the bottom interface of the source layer, and there are layers above and below the source layer, which are numbered in an increasing order from the bottommost layer, layer-0, to the topmost layer, layer-(N-1).

Green's Functions Due to Horizontal Electric Dipole (HED)

Derivation of spectral-domain Green's functions starts with assuming that the source HED is in a homogenous and unbounded medium with the electrical properties of layer-*i*, which implies that source and observation points are in the same layer. Since the polarization of HED is arbitrary on *xy*-plane, i.e., one can arbitrarily choose the direction of dipole, $\hat{\alpha} = \hat{x}$ has been chosen for convenience. Therefore, the longitudinal field components (*xy*-plane is transverse plane while *z*-axis is the longitudinal axis) can be written from (2.13) and (2.14) as

$$E_{zi} = -\frac{jIl}{4\pi\omega\varepsilon_i}\frac{\partial^2}{\partial z \partial x}\frac{e^{-jk_i|\mathbf{r}-\mathbf{r}'|}}{|\mathbf{r}\text{-}\mathbf{r}'|} \tag{2.16}$$

$$H_{zi} = -\frac{Il}{4\pi}\frac{\partial}{\partial y}\frac{e^{-jk_i|\mathbf{r}-\mathbf{r}'|}}{|\mathbf{r}\text{-}\mathbf{r}'|} \tag{2.17}$$

Hence, using the Weyl identity (2.15) and interchanging the order of differentiation, the longitudinal field components in (2.16) and (2.17) are expressed as integral summations of plane waves propagating in all directions as follows:

$$E_{zi} = \frac{\pm Il}{8\pi^2 \omega \varepsilon_i} \int_{-\infty}^{\infty}\int_{-\infty}^{\infty} dk_x dk_y k_x e^{-jk_x(x-x')-jk_y(y-y')} e^{-jk_{zi}|z-z'|} \tag{2.18}$$

$$H_{zi} = \frac{Il}{8\pi^2} \int_{-\infty}^{\infty}\int_{-\infty}^{\infty} dk_x dk_y k_y e^{-jk_x(x-x')-jk_y(y-y')} \frac{e^{-jk_{zi}|z-z'|}}{k_{zi}} \tag{2.19}$$

where $k_{zi} = \sqrt{k_i^2 - k_x^2 - k_y^2}$, $\pm$ is due to the derivative of $\exp(-jk_{zi}|z-z'|)$ with respect to z variable: + for $z > z'$, − for $z < z'$. As previously stated, the propagation constants along x and y directions, k_x and k_y, respectively, must be equal in all layers due to translational invariance of the fields and the phase matching conditions at the interfaces. Therefore, in case of a multilayer medium, the fields written in an unbounded medium, (2.18) and (2.19), need to be modified, only in the z-components of the exponentials, to handle the reflections from the interfaces above and below. As a result, the fields in the source layer can be written as the sum of the direct waves and the reflected waves from the boundaries:

$$E_{zi} = \frac{Il}{8\pi^2 \omega \varepsilon_i} \int_{-\infty}^{\infty}\int_{-\infty}^{\infty} dk_x dk_y \, k_x e^{-jk_x(x-x')-jk_y(y-y')} F_{TM}(z,z') \tag{2.20}$$

$$H_{zi} = \frac{Il}{8\pi^2} \int_{-\infty}^{\infty}\int_{-\infty}^{\infty} dk_x dk_y \, k_y \frac{e^{-jk_x(x-x')-jk_y(y-y')}}{k_{zi}} F_{TE}(z,z') \tag{2.21}$$

where

$$F_{TE}(z,z') = e^{-jk_{zi}|z-z'|} + A_h^e \, e^{jk_{zi}(z-z')} + C_h^e \, e^{-jk_{zi}(z-z')} \tag{2.22}$$

$$F_{TM}(z,z') = \pm e^{-jk_{zi}|z-z'|} + B_h^e \, e^{jk_{zi}(z-z')} + D_h^e \, e^{-jk_{zi}(z-z')} \tag{2.23}$$

and A_h^e, B_h^e, C_h^e, and D_h^e are the coefficients of down-going and up-going waves in layer-*i*, and subscript *h* and superscript *e* represent the source to be horizontal and electric type. Since the longitudinal field components E_{zi} and H_{zi} belong explicitly to TM-z and TE-z waves, the functions that vary with z and z' in their integral representations are referred to as F_{TM} and F_{TE}, respectively. The first terms in (2.22) and (2.23) account for the direct terms, while the

second and the third terms represent down-going and up-going waves in layer-i, respectively, due to reflections from the neighboring interfaces.

To find the coefficients in terms of some known quantities, the boundary conditions at the interfaces need to be satisfied. One way of doing this is to apply the continuity of the normal components of the displacement vector **D** and magnetic flux density **B**, that is, $\varepsilon_i E_{zi} = \varepsilon_{i+1} E_{z(i+1)}$ and $\mu_i H_{zi} = \mu_{i+1} H_{z(i+1)}$ at the interface between layer-i and layer-(i+1), and $\varepsilon_{i-1} E_{z(i-1)} = \varepsilon_i E_{zi}$ and $\mu_{i-1} H_{z(i-1)} = \mu_i H_{zi}$ at the interface between layer-i and layer-(i-1). Another way is to trace the down-going and up-going waves in layer-i as follows: the down-going wave at $z = d_i$ in the source layer is the consequence of the reflection of up-going wave at $z = d_i$, and the up-going wave at $z = 0$ is the consequence of the reflection of down-going wave at $z = 0$. Hence, for TM waves, the following expressions are obtained,

$$\underbrace{B_h^e e^{jk_{zi}(d_i - z')}}_{\substack{down-going\ wave \\ at\ z=d_i}} = \tilde{R}_{TM}^{i,i+1} \underbrace{\left(e^{-jk_{zi}(d_i - z')} + D_h^e e^{-jk_{zi}(d_i - z')} \right)}_{up-going\ wave\ at\ z=d_i} \tag{2.24}$$

$$\underbrace{D_h^e e^{jk_{zi} z'}}_{\substack{up-going\ wave \\ at\ z=0}} = \tilde{R}_{TM}^{i,i-1} \underbrace{\left(-e^{-jk_{zi} z'} + B_h^e e^{-jk_{zi} z'} \right)}_{down-going\ wave\ at\ z=0} \tag{2.25}$$

and solving them simultaneously, the unknown coefficients B_h^e and D_h^e are found as

$$B_h^e = \frac{\tilde{R}_{TM}^{i,i+1} e^{-j2k_{zi}(d_i - z')} - \tilde{R}_{TM}^{i,i+1} \tilde{R}_{TM}^{i,i-1} e^{-j2k_{zi} d_i}}{1 - \tilde{R}_{TM}^{i,i+1} \tilde{R}_{TM}^{i,i-1} e^{-j2k_{zi} d_i}} \tag{2.26}$$

$$D_h^e = \frac{-\tilde{R}_{TM}^{i,i-1} e^{-j2k_{zi} z'} + \tilde{R}_{TM}^{i,i-1} \tilde{R}_{TM}^{i,i+1} e^{-j2k_{zi} d_i}}{1 - \tilde{R}_{TM}^{i,i+1} \tilde{R}_{TM}^{i,i-1} e^{-j2k_{zi} d_i}} \tag{2.27}$$

where the tilde over the reflection coefficients R designates the generalized reflection coefficients, while R designates the Fresnel reflection coefficients. Following the same procedure for TE waves, using the expression (2.22), the coefficients A_h^e and C_h^e can be obtained as

$$A_h^e = \frac{\tilde{R}_{TE}^{i,i+1} e^{-j2k_{zi}(d_i - z')} + \tilde{R}_{TE}^{i,i+1} \tilde{R}_{TE}^{i,i-1} e^{-j2k_{zi}d_i}}{1 - \tilde{R}_{TE}^{i,i+1} \tilde{R}_{TE}^{i,i-1} e^{-j2k_{zi}d_i}} \tag{2.28}$$

$$C_h^e = \frac{\tilde{R}_{TE}^{i,i-1} e^{-j2k_{zi}z'} + \tilde{R}_{TE}^{i,i-1} \tilde{R}_{TE}^{i,i+1} e^{-j2k_{zi}d_i}}{1 - \tilde{R}_{TE}^{i,i+1} \tilde{R}_{TE}^{i,i-1} e^{-j2k_{zi}d_i}} \tag{2.29}$$

After having defined the coefficients in terms of known quantities, the longitudinal components of electric and magnetic fields in spectral domain, which are the integrands of (2.20) and (2.21), have become known field components. With the knowledge of the longitudinal field components in spectral domain, the transverse components of magnetic and electric fields can be obtained from

$$\tilde{\mathbf{H}}_t = \frac{1}{k^2 - k_z^2}\left[\frac{\partial}{\partial z}\nabla_t \tilde{H}_z + j\omega\varepsilon \nabla_t \times \hat{z}\tilde{E}_z\right] \tag{2.30}$$

$$\tilde{\mathbf{E}}_t = \frac{1}{k^2 - k_z^2}\left[\frac{\partial}{\partial z}\nabla_t \tilde{E}_z - j\omega\mu \nabla_t \times \hat{z}\tilde{H}_z\right] \tag{2.31}$$

where ~ denotes the spectral-domain representation of the corresponding field component. Hence, the spectral-domain representations of the Green's functions for the vector and scalar potentials are deduced from these field components. Using the definition of the vector potential, (2.9), its *x*-component can be written in layer-*i* as

$$\begin{aligned} A_{xi} &= -\mu_i \int H_{zi} dy \\ &= \frac{Il}{j8\pi^2} \int_{-\infty}^{\infty}\int_{-\infty}^{\infty} dk_x dk_y \frac{e^{-jk_x x - jk_y y}}{k_{zi}} F_{TE} \end{aligned} \tag{2.32}$$

then, by substituting (2.22) in (2.32) and after a little bit manipulation, the spectral-domain Green's function in the source layer for the *x*-component of the vector potential is obtained as

$$\tilde{G}_{xx}^A = \frac{\mu_i}{j2k_{zi}}\left[e^{-jk_{zi}|z-z'|} + A_h^e\, e^{jk_{zi}(z-z')} + C_h^e\, e^{-jk_{zi}(z-z')}\right] \tag{2.33}$$

As it was discussed previously, the traditional form of the Green's function for the vector potential has the *z*-component of the vector potential due to an HED, $\tilde{G}_{zx}^{A}$, in addition to $\tilde{G}_{xx}^{A}$. Therefore, following a similar procedure, Green's function $\tilde{G}_{zx}^{A}$ can be derived by writing A_z from the definition of the vector potential, and by using the expression of the field component in terms of the longitudinal field components as follows:

$$A_{zi} = \mu_i \int H_{xi} dy = \mu_i \int \frac{1}{k_\rho^2} \left[\frac{\partial^2}{\partial z \partial x} H_{zi} + j\omega\varepsilon_i \frac{\partial}{\partial y} E_{zi} \right] dy$$

$$= \frac{\mu_i I l}{8\pi^2} \int_{-\infty}^{\infty} \int_{-\infty}^{\infty} dk_x dk_y e^{-jk_x x - jk_y y} \left\{ \frac{k_x}{k_{zi} k_\rho^2} \frac{\partial}{\partial z} F_{TE} + \frac{jk_x}{k_\rho^2} F_{TM} \right\} \tag{2.34}$$

$$\Rightarrow \tilde{G}_{zx}^{A} = \frac{j\mu_i k_x}{2\left(k_i^2 - k_{zi}^2\right)} \left[\left(A_h^e + B_h^e\right) e^{jk_{zi}(z-z')} + \left(D_h^e - C_h^e\right) e^{-jk_{zi}(z-z')} \right] \tag{2.35}$$

Once the components of Green's function for the vector potential has been derived in the source layer, layer-*i*, the Green's function for the scalar potential due to an HED can be obtained from the vector potential. There are two ways to obtain the Green's functions for scalar potential. The one starts with writing the scalar potential due to an HED in terms of vector potential, via Lorentz gauge, (2.10), as follows:

$$\phi_d = -\frac{\nabla \cdot \mathbf{A}}{j\omega\mu_i\varepsilon_i} = -\frac{1}{j\omega\mu_i\varepsilon_i} \left(\frac{\partial A_x}{\partial x} + \frac{\partial A_z}{\partial z} \right) \tag{2.36}$$

where ϕ_d is the scalar potential of a dipole. Note that the MPIE formulation requires the scalar Green's function for a single charge, which is simply related to the one for a dipole as

$$\phi_d = \frac{\partial}{\partial x'} \phi_q \tag{2.37}$$

Hence, after a few algebraic manipulations, the scalar Green's function for a single charge is obtained as

$$\Rightarrow \tilde{G}_x^q = \frac{1}{j2\varepsilon_i k_\rho^2}\left[\frac{k_\rho^2}{k_{zi}} e^{-jk_{zi}|z-z'|} + \frac{k_i^2 A_h^e + k_{zi}^2 B_h^e}{k_{zi}} e^{jk_{zi}(z-z')} + \frac{k_i^2 C_h^e - k_{zi}^2 D_h^e}{k_{zi}} e^{-jk_{zi}(z-z')}\right] \tag{2.38}$$

Another way to get the scalar potential is to use the relation between the Green's functions for vector and scalar potentials, [39],

$$\frac{j\omega}{k_i^2}\nabla \cdot \overline{\mathbf{G}}^A = \frac{1}{j\omega}\nabla' G^q \tag{2.39}$$

For the scalar potential Green's function, using (2.39) together with the available components of the vector potential, the following relation is obtained in the spatial domain:

$$\frac{\partial}{\partial x'} G_x^q = \frac{-1}{\mu_i \varepsilon_i}\left[\frac{\partial}{\partial x} G_{xx}^A + \frac{\partial}{\partial z} G_{zx}^A\right] \tag{2.40}$$

Considering the spectral-domain representations of the Green's functions, with $\partial/\partial x' = -\partial/\partial x$ and $\partial/\partial x \rightarrow -jk_x$ substitutions, (2.40) can be written in the spectral domain as

$$\tilde{G}_x^q = \frac{-1}{\mu_i \varepsilon_i}\left[-\tilde{G}_{xx}^A + \frac{1}{jk_x}\frac{\partial}{\partial z}\tilde{G}_{zx}^A\right] \tag{2.41}$$

Substituting (2.33) together with (2.35) into (2.41) and re-arranging the terms, the spectral-domain Green's function of the scalar potential given in (2.38) can be obtained.

Green's Functions Due to Vertical Electric Dipole (VED)

The derivation procedure for the spectral-domain Green's function for a VED is almost the same as the one for an HED, therefore, it will be briefly given here without repeating all the details. Since the polarization of the dipole is in z-direction, i.e., $\hat{\alpha} = \hat{z}$, the longitudinal field components in the source layer, layer-i, can be written from (2.13) and (2.14) as

$$E_{zi} = -\frac{jIl\omega I_i}{4\pi k_i^2}\left(k_i^2 + \frac{\partial^2}{\partial z^2}\right)\frac{e^{-jk_i|\mathbf{r}-\mathbf{r}'|}}{|\mathbf{r}-\mathbf{r}'|} \tag{2.42}$$

$$H_{zi} = 0 \tag{2.43}$$

where having a zero longitudinal magnetic field implies the absence of TE waves for this source orientation. Using the Weyl identity (2.15) and interchanging the order of differentiation, the spherical wave terms in (2.42) and (2.43) are expressed as an integral summation of plane waves propagating in all directions as

$$E_{zi} = \frac{-Il}{8\pi^2 \omega \varepsilon_i} \int_{-\infty}^{\infty}\int_{-\infty}^{\infty} dk_x dk_y \, k_\rho^2 \, e^{-jk_x(x-x')-jk_y(y-y')} \frac{e^{-jk_{zi}|z-z'|}}{k_{zi}} \tag{2.44}$$

for a homogenous and unbounded medium. In cases of multilayer media, the plane wave constituents need to be modified to handle the reflections from the interfaces above and below, as in HED. As a result, the total longitudinal field in the source layer can be written as

$$E_{zi} = \frac{-Il}{8\pi^2 \omega \varepsilon_i} \int_{-\infty}^{\infty}\int_{-\infty}^{\infty} dk_x dk_y \, \frac{k_\rho^2}{k_{zi}} e^{-jk_x(x-x')-jk_y(y-y')} F_{TM}(z,z') \tag{2.45}$$

where

$$F_{TM}(z,z') = e^{-jk_{zi}|z-z'|} + A_v^e \, e^{jk_{zi}(z-z')} + B_v^e \, e^{-jk_{zi}(z-z')} \tag{2.46}$$

and A_v^e and B_v^e are the coefficients of down-going and up-going waves due to the reflections from layers above and below the source layer, respectively. By applying boundary conditions at the interface of the layers, these coefficients can be found as

$$A_v^e = \frac{\tilde{R}_{TM}^{i,i+1} e^{-j2k_{zi}(d_i - z')} + \tilde{R}_{TM}^{i,i+1} \tilde{R}_{TM}^{i,i-1} e^{-j2k_{zi}d_i}}{1 - \tilde{R}_{TM}^{i,i+1} \tilde{R}_{TM}^{i,i-1} e^{-j2k_{zi}d_i}} \tag{2.47}$$

$$B_v^e = \frac{\tilde{R}_{TM}^{i,i-1} e^{-j2k_{zi}z'} + \tilde{R}_{TM}^{i,i-1} \tilde{R}_{TM}^{i,i+1} e^{-j2k_{zi}d_i}}{1 - \tilde{R}_{TM}^{i,i+1} \tilde{R}_{TM}^{i,i-1} e^{-j2k_{zi}d_i}} \tag{2.48}$$

where subscript *v* and superscript *e* represent the source to be vertical and electric type. With the knowledge of the longitudinal field components in spectral domain, the transverse components of magnetic and electric fields are obtained from (2.30) and (2.31), as detailed in

HED case. Then, using the definition of the vector potential, (2.9), its z-component can be written as

$$A_{zi} = \mu_i \int H_{xi} dy = \mu_i \int \frac{1}{k_\rho^2} \left[j\omega\varepsilon_i \frac{\partial}{\partial y} E_{zi} \right] dy$$

$$= j \frac{\mu_i Il}{8\pi^2} \int_{-\infty}^{\infty} \int_{-\infty}^{\infty} dk_x dk_y e^{-jk_x x - jk_y y} \left(\frac{k^2}{k_{zi} k_\rho^2} - \frac{k_{zi}}{k_\rho^2} \right) F_{TM} \tag{2.49}$$

Then, substituting (2.46) in (2.49) and after a little bit of manipulation, the spectral-domain Green's function of vector potential is obtained as

$$\tilde{G}_{zz}^A = \frac{\mu_i}{2jk_{zi}} \left\{ e^{-jk_{zi}|z-z'|} + A_v^e e^{-jk_{zi}(z-z')} + B_v^e e^{jk_{zi}(z-z')} \right\} \tag{2.50}$$

With the use of the equation relating the Green's functions of vector and scalar potentials, (2.39), for a VED,

$$\frac{\partial}{\partial z'} \tilde{G}_z^q = -\frac{1}{\mu_i \varepsilon_i} \frac{\partial}{\partial z} \tilde{G}_{zz}^A \tag{2.51}$$

Green's function for the scalar potential is obtained as

$$\tilde{G}_z^q = \frac{1}{j2\varepsilon_i k_{zi}} \left[e^{-jk_{zi}|z-z'|} + C_v^e e^{jk_{zi}(z-z')} + D_v^e e^{-jk_{zi}(z-z')} \right] \tag{2.52}$$

The unknown coefficients in (2.50) and (2.52) are obtained following the same procedure as that for the HED case, and they all are provided in the following sub-section to summarize the available Green's functions for HED and VED sources.

Spectral-Domain Green's Functions for Electric Dipole

To summarize, the available spectral-domain Green's functions for the vector and scalar potentials due to a horizontal and vertical electrical dipoles are provided below, in the source layer, with the definition of generalized reflection coefficient and the amplitude coefficients [25]:

$$\tilde{G}_{xx}^{A} = \frac{\mu_i}{2jk_{zi}}\left[e^{-jk_{zi}|z-z'|} + A_h^e\, e^{jk_{zi}(z-z')} + C_h^e\, e^{-jk_{zi}(z-z')}\right] \tag{2.53}$$

$$\tilde{G}_{zx}^{A} = -\frac{\mu_i}{2jk_{zi}}\left[\frac{k_x k_{zi}}{k_\rho^2}\left(A_h^e + B_h^e\right)e^{jk_{zi}(z-z')} + \frac{k_x k_{zi}}{k_\rho^2}\left(D_h^e - C_h^e\right)e^{-jk_{zi}(z-z')}\right] \tag{2.54}$$

$$\tilde{G}_{x}^{q} = \frac{1}{j2\varepsilon_i k_\rho^2}\left[\frac{k_\rho^2}{k_{zi}}e^{-jk_{zi}|z-z'|} + \frac{k_i^2 A_h^e + k_{zi}^2 B_h^e}{k_{zi}}e^{jk_{zi}(z-z')} + \frac{k_i^2 C_h^e - k_{zi}^2 D_h^e}{k_{zi}}e^{-jk_{zi}(z-z')}\right] \tag{2.55}$$

$$\tilde{G}_{zz}^{A} = \frac{\mu_i}{2jk_{zi}}\left[e^{-jk_{zi}|z-z'|} + A_v^e e^{-jk_{zi}(z-z')} + B_v^e e^{jk_{zi}(z-z')}\right] \tag{2.56}$$

$$\tilde{G}_{z}^{q} = \frac{1}{2j\varepsilon_i k_{zi}}\left[e^{-jk_{zi}|z-z'|} + C_v^e\, e^{jk_{zi}(z-z')} + D_v^e\, e^{-jk_{zi}(z-z')}\right] \tag{2.57}$$

where the superscripts A and q denote the magnetic vector and electric scalar potentials, respectively. The coefficients $A_{h,v}^e, B_{h,v}^e, C_{h,v}^e$ and $D_{h,v}^e$ are the functions of generalized reflection coefficients [25,40] and are arranged and re-written as

$$A_h^e = \tilde{R}_{TE}^{i,i+1} M_i^{TE}\left[e^{-j2k_{zi}(d_i - z')} + \tilde{R}_{TE}^{i,i-1} e^{-j2k_{zi}d_i}\right] \tag{2.58}$$

$$B_h^e = \tilde{R}_{TM}^{i,i+1} M_i^{TM}\left[e^{-j2k_{zi}(d_i - z')} - \tilde{R}_{TM}^{i,i-1} e^{-j2k_{zi}d_i}\right] \tag{2.59}$$

$$C_h^e = \tilde{R}_{TE}^{i,i-1} M_i^{TE}\left[e^{-j2k_{zi}z'} + \tilde{R}_{TE}^{i,i+1} e^{-j2k_{zi}d_i}\right] \tag{2.60}$$

$$D_h^e = \tilde{R}_{TM}^{i,i-1} M_i^{TM}\left[-e^{-j2k_{zi}z'} + \tilde{R}_{TM}^{i,i+1} e^{-j2k_{zi}d_i}\right] \tag{2.61}$$

$$A_v^e = \tilde{R}_{TM}^{i,i-1} M_i^{TM}\left[e^{-j2k_{zi}z'} + \tilde{R}_{TM}^{i,i+1} e^{-j2k_{zi}d_i}\right] \tag{2.62}$$

$$B_v^e = \tilde{R}_{TM}^{i,i+1} M_i^{TM}\left[e^{-j2k_{zi}(d_i - z')} + \tilde{R}_{TM}^{i,i-1} e^{-j2k_{zi}d_i}\right] \tag{2.63}$$

$$C_v^e = \tilde{R}_{TM}^{i,i-1} M_i^{TM}\left[-e^{-j2k_{zi}z'} + \tilde{R}_{TM}^{i,i+1} e^{-j2k_{zi}d_i}\right] \tag{2.64}$$

$$D_v^e = \tilde{R}_{TM}^{i,i+1} M_i^{TM} \left[-e^{-j2k_{zi}(d_i - z')} + \tilde{R}_{TM}^{i,i-1} e^{-j2k_{zi}d_i} \right] \tag{2.65}$$

where

$$M_i^{TE,TM} = \left[1 - \tilde{R}_{TE,TM}^{i,i+1} \tilde{R}_{TE,TM}^{i,i-1} e^{-j2k_{zi}d_i} \right]^{-1} \tag{2.66}$$

$$\tilde{R}_{TE,TM}^{i,i-1} = R_{TE,TM}^{i,i-1} + \frac{T_{TE,TM}^{i,i-1} T_{TE,TM}^{i-1,i} \tilde{R}_{TE,TM}^{i-1,i-2} e^{-jk_{z(i-1)}2d_{i-1}}}{1 - \tilde{R}_{TE,TM}^{i-1,i-2} R_{TE,TM}^{i-1,i} e^{-jk_{z(i-1)}2d_{i-1}}} \tag{2.67}$$

$$\tilde{R}_{TE,TM}^{i,i+1} = R_{TE,TM}^{i,i+1} + \frac{T_{TE,TM}^{i,i+1} T_{TE,TM}^{i+1,i} \tilde{R}_{TE,TM}^{i+1,i+2} e^{-jk_{z(i+1)}2d_{i+1}}}{1 - \tilde{R}_{TE,TM}^{i+1,i+2} R_{TE,TM}^{i+1,i} e^{-jk_{z(i+1)}2d_{i+1}}} \tag{2.68}$$

and the Fresnel reflection coefficients are defined as

$$R_{TE}^{i,i-1} = \frac{\mu_{i-1}k_{zi} - \mu_i k_{z(i-1)}}{\mu_{i-1}k_{zi} + \mu_i k_{z(i-1)}};\ R_{TM}^{i,i-1} = \frac{\varepsilon_{i-1}k_{zi} - \varepsilon_i k_{z(i-1)}}{\varepsilon_{i-1}k_{zi} + \varepsilon_i k_{z(i-1)}}$$

Note that $T^{i,i\pm1} = 1 + R^{i,i\pm1}$ and $R^{i,i\pm1} = -R^{i\pm1,i}$ for both polarizations of waves, subscripts TE and TM represent the polarizations of waves, and superscripts show the layer numbers. Although the components of Green's functions due to an HED are specifically due to an *x*-polarized HED, Green's functions for *y*-polarized HED can be simply obtained from them, by setting $\tilde{G}_{yy}^A = \tilde{G}_{xx}^A$, $\tilde{G}_{zy}^A / k_y = \tilde{G}_{zx}^A / k_x$, and $\tilde{G}_y^q = \tilde{G}_x^q$.

The spectral-domain Green's functions provided above were obtained in the source layer, which means the source and the observation points are in layer-*i*. When the observation layer is different from the source layer, the amplitudes of Green's functions need to be modified by incorporating the transmissions through different layers, with the recursive use of appropriate boundary conditions, whose detail is discussed in the following sub-sections.

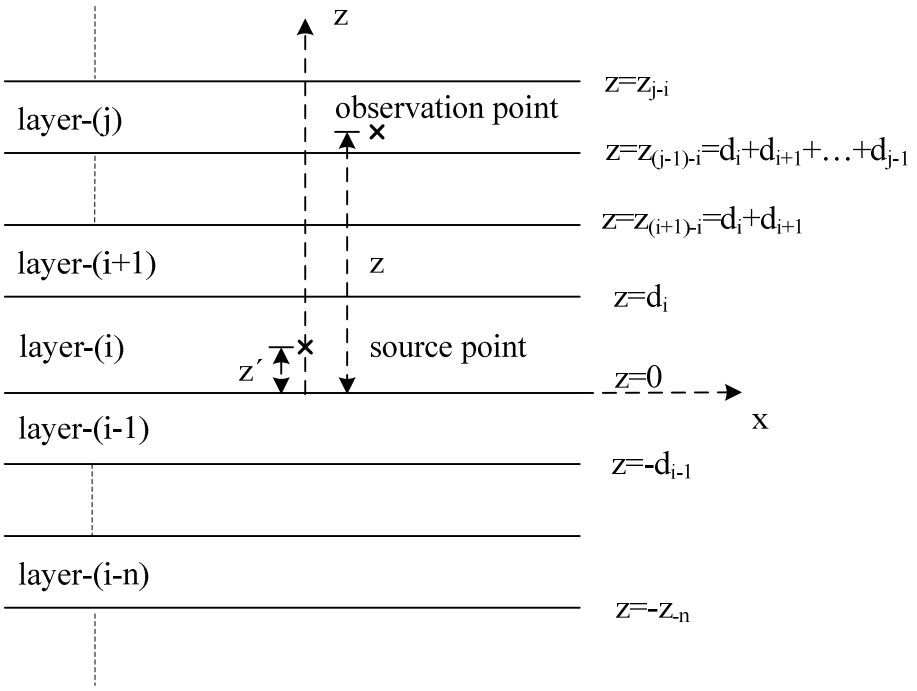

Figure 2.3: A general planar multilayer structure. Source layer = layer-(i); observation layer = layer-(j), where j > i

Green's Functions for Observation Layer above Source Layer

For the sake of illustration, a general planar stratified medium is given in Fig. 2.3, where a general source is located in layer-*i* and observation point is in layer-*j,* which is above the source layer. The field expressions (for TE and TM waves) in layer-*j* is assumed to be in the form of [43]

$$\tilde{F} = A_j \left[e^{-jk_{zj}(z-z')} + \tilde{R}^{j,j+1} e^{jk_{zj}(z-z')} e^{-jk_{zj}2(z_{j-i}-z')} \right] \tag{2.69}$$

where $\tilde{F}$ denotes the spectral-domain representation of the field expressions, A_j is the amplitude of the up-going waves in layer-*j* to be determined and z_{j-i} is the distance from the origin to the upper interface of the observation layer *j*, [40]. Starting from the amplitude of

the fields in source layer, A_i^+ for up-going waves, one can determine the amplitudes of the fields in any layer iteratively using

$$A_{i+1}\, e^{-jk_{z(i+1)}(d_i - z')} = A_i^+\, e^{-jk_{zi}(d_i - z')} \underbrace{\frac{T^{i,i+1}}{1 - \tilde{R}^{i+1,i+2} R^{i+1,i}\, e^{-jk_{z(i+1)} 2d_{i+1}}}}_{\Gamma^{i,i+1}} \tag{2.70}$$

for the layers above the source layer.

Note that the term denoted by $\Gamma^{i,i+1}$ describes the transmission from the top of layer-*i* to the bottom of layer-(*i*+1). Therefore, it is quite easy to generalize the transfer function from layer-*i* to layer-*j*, for *j*>*i*, as

$$A_j e^{-jk_{zj}(z_{(j-1)-i} - z')} = A_i^+\, e^{-jk_{zi}(d_i - z')} \underbrace{\left(\prod_{n=i}^{j-2} \Gamma^{n,n+1} e^{-jk_{z(n+1)} d_{n+1}} \right)}_{=1 \text{ for } j-2<i} \Gamma^{j-1,j} \tag{2.71}$$

where $z_{(j-1)-i} = \sum_{n=i}^{j-1} d_n$.

The spectral-domain Green's function $\tilde{G}_{xx}^A$ is used to demonstrate the working of the procedure in detail. First, the spectral-domain representation in the source layer, (2.53), needs to be cast in the form of (2.69) for $z > z'$, to obtain the explicit form of A_i^{+TE}. To do this, F_{TE} in (2.22) is written for $z > z'$ with the substitution of the amplitudes A_h^e and C_h^e from (2.58) and (2.60), respectively, as

$$\begin{aligned} F_{TE}^+ &= e^{-jk_{zi}(z-z')} + \left[e^{-jk_{zi} 2(d_i - z')} \tilde{R}_{i,i+1}^{TE} M_i^{TE} + e^{-jk_{zi} 2d_i} \tilde{R}_{i,i+1}^{TE} \tilde{R}_{i,i-1}^{TE} M_i^{TE} \right] e^{jk_{zi}(z-z')} \\ &\quad + \left[e^{-jk_{zi} 2z'} \tilde{R}_{i,i-1}^{TE} M_i^{TE} + e^{-jk_{zi} 2d_i} \tilde{R}_{i,i-1}^{TE} \tilde{R}_{i,i+1}^{TE} M_i^{TE} \right] e^{-jk_{zi}(z-z')} \end{aligned} \tag{2.72}$$

$$\begin{aligned} &= e^{-jk_{zi}(z-z')} \left[1 + e^{-jk_{zi} 2z'} \tilde{R}_{i,i-1}^{TE} M_i^{TE} + e^{-jk_{zi} 2d_i} \tilde{R}_{i,i-1}^{TE} \tilde{R}_{i,i+1}^{TE} M_i^{TE} \right] \\ &\quad + e^{jk_{zi}(z-z')} \left[e^{-jk_{zi} 2(d_i - z')} \tilde{R}_{i,i+1}^{TE} M_i^{TE} + e^{-jk_{zi} 2d_i} \tilde{R}_{i,i+1}^{TE} \tilde{R}_{i,i-1}^{TE} M_i^{TE} \right] \end{aligned}$$

Then, $e^{-jk_{zi}(z-z')}M_i^{TE}$ term, where M_i^{TE} is defined in (2.66), is added to and subtracted from the summation without changing the value of the spectral-domain representation. This leads to a further simplification in the equation as follows:

$$F_{TE}^{+} = e^{-jk_{zi}(z-z')}\left[1+e^{-jk_{zi}2z'}\tilde{R}_{i,i-1}^{TE}M_i^{TE} + M_i^{TE} - \overbrace{M_i^{TE}\left(1-e^{-jk_{zi}2d_i}\tilde{R}_{i,i-1}^{TE}\tilde{R}_{i,i+1}^{TE}\right)}^{=1}\right]$$
$$+ e^{jk_{zi}(z-z')}\left[e^{-jk_{zi}2(d_i-z')}\tilde{R}_{i,i+1}^{TE}M_i^{TE} + e^{-jk_{zi}2d_i}\tilde{R}_{i,i+1}^{TE}\tilde{R}_{i,i-1}^{TE}M_i^{TE}\right]$$

After a little bit manipulations, F_{TE}^{+} can be written in the form of (2.69) as

$$F_{TE}^{+} = \underbrace{\left(1+e^{-jk_{zi}2z'}\tilde{R}_{i,i-1}^{TE}\right)M_i^{TE}}_{A_i^{+TE}}\left[e^{-jk_{zi}(z-z')} + \tilde{R}_{i,i+1}^{TE}e^{jk_{zi}(z-z')}e^{-jk_{zi}2(d_i-z')}\right] \tag{2.73}$$

Hence, the spectral-domain Green's function $\tilde{G}_{xx}^{A}$ for observation layer-*j* can be obtained using (2.32) as

$$\tilde{G}_{xx}^{A} = \frac{\mu_j}{2jk_{zi}}A_j^{TE}\left[e^{-jk_{zj}(z-z')} + \tilde{R}_{j,j+1}^{TE}e^{jk_{zj}(z-z')}e^{-jk_{zj}2z_{j-i}}\right] \tag{2.74}$$

where A_j^{TE} can be evaluated iteratively starting from the source layer with A_i^{+TE} and using (2.70) up to the observation layer. The same procedure can be applied to other spectral-domain Green's functions by using their definitions given in (2.53)-(2.57). However, as $\tilde{G}_{xx}^{A}$ is composed of TE waves only, for Green's functions with TE and TM wave contributions, A_j should be derived for TE and TM waves separately, as demonstrated in the following example.

The spectral-domain Green's function $\tilde{G}_{zx}^{A}$ is used to demonstrate the working of the procedure whose spectral-domain representation in the source layer, (2.54), consists of both TE and TM wave components. First, the spectral domain representation in the source layer needs to be cast in the form of (2.69), to obtain the explicit forms of amplitudes of the up-going TE and TM waves, which are denoted as A_i^{+TE} and A_i^{+TM}, respectively. Since A_i^{+TE} has

already been derived in the previous example, (2.73), A_i^{+TM} can be obtained similarly using F_{TM}^{+}. To do this, F_{TM} in (2.23) is written for $z > z'$ with the substitution of the amplitudes B_h^e and D_h^e from (2.59) and (2.61), respectively, as

$$\begin{aligned} F_{TM}^{+} &= e^{-jk_{zi}(z-z')} + \left[e^{-jk_{zi}2(d_i-z')} \tilde{R}_{i,i+1}^{TM} M_i^{TM} - e^{-jk_{zi}2d_i} \tilde{R}_{i,i+1}^{TM} \tilde{R}_{i,i-1}^{TM} M_i^{TM} \right] e^{jk_{zi}(z-z')} \\ &\quad + \left[-e^{-jk_{zi}2z'} \tilde{R}_{i,i-1}^{TM} M_i^{TM} + e^{-jk_{zi}2d_i} \tilde{R}_{i,i-1}^{TM} \tilde{R}_{i,i+1}^{TM} M_i^{TM} \right] e^{-jk_{zi}(z-z')} \qquad (2.75) \\ &= -e^{-jk_{zi}(z-z')} \left[-1 + e^{-jk_{zi}2z'} \tilde{R}_{i,i-1}^{TM} M_i^{TM} - e^{-jk_{zi}2d_i} \tilde{R}_{i,i-1}^{TM} \tilde{R}_{i,i+1}^{TM} M_i^{TM} \right] \\ &\quad + e^{jk_{zi}(z-z')} \left[e^{-jk_{zi}2(d_i-z')} \tilde{R}_{i,i+1}^{TM} M_i^{TM} + e^{-jk_{zi}2d_i} \tilde{R}_{i,i+1}^{TM} \tilde{R}_{i,i-1}^{TM} M_i^{TM} \right] \end{aligned}$$

Then, $e^{-jk_{zi}(z-z')} M_i^{TM}$ term, where M_i^{TM} is defined in (2.66), is added to and subtracted from the summation without changing the value of spectral-domain representation. This leads to a further simplification in the equation as follows:

$$\begin{aligned} F_{TM}^{+} &= -e^{-jk_{zi}(z-z')} \left[-1 + e^{-jk_{zi}2z'} \tilde{R}_{i,i-1}^{TM} M_i^{TM} - M_i^{TM} + \overbrace{M_i^{TM} \left(1 - e^{-jk_{zi}2d_i} \tilde{R}_{i,i-1}^{TM} \tilde{R}_{i,i+1}^{TM} \right)}^{=1} \right] \\ &\quad + e^{jk_{zi}(z-z')} \left[e^{-jk_{zi}2(d_i-z')} \tilde{R}_{i,i+1}^{TM} M_i^{TM} + e^{-jk_{zi}2d_i} \tilde{R}_{i,i+1}^{TM} \tilde{R}_{i,i-1}^{TM} M_i^{TM} \right] \end{aligned}$$

After some algebraic manipulations, F_{TM}^{+} can be obtained in the form of (2.69) as

$$F_{TM}^{+} = \underbrace{\left(1 - e^{-jk_{zi}2z'} \tilde{R}_{i,i-1}^{TM} \right) M_i^{TM}}_{A_i^{+TM}} \left[e^{-jk_{zi}(z-z')} + \tilde{R}_{i,i+1}^{TM} e^{jk_{zi}(z-z')} e^{-jk_{zi}2(d_i-z')} \right] \qquad (2.76)$$

The spectral-domain Green's function $\tilde{G}_{zx}^{A}$ for observation layer-*j* can be obtained from (2.77) by substituting (2.78) and (2.79) as follows:

$$A_{zj} = \frac{\mu_j Il}{8\pi^2 k_{zi}} \int_{-\infty}^{\infty} \int_{-\infty}^{\infty} dk_x dk_y e^{-jk_x x - jk_y y} \left\{ \frac{k_x}{k_\rho^2} \frac{\partial}{\partial z} F_{TE} + \frac{jk_x k_{zj}}{k_\rho^2} F_{TM} \right\} \qquad (2.77)$$

$$\frac{\partial F_{TE}}{\partial z} = \left(\frac{\mu_i}{\mu_j} \right) jk_{zj} A_j^{TE} \left[-e^{-jk_{zj}(z-z')} + \tilde{R}_{j,j+1}^{TE} e^{jk_{zj}(z-z')} e^{-jk_{zj}2z_{j-i}} \right] \qquad (2.78)$$

$$F_{TM} = A_j^{TM}\left[e^{-jk_{zj}(z-z')} + \tilde{R}_{j,j+1}^{TM} e^{jk_{zj}(z-z')} e^{-jk_{zj}2z_{j-i}}\right] \tag{2.79}$$

$$\frac{-1}{jk_x}\tilde{G}_{zx}^{A} = \frac{\mu_j}{2jk_{zi}}\begin{Bmatrix} \dfrac{j}{k_\rho^2}\left[\left(\dfrac{\mu_i}{\mu_j}\right)k_{zj}A_j^{TE} - k_{zi}A_j^{TM}\right]e^{-jk_{zj}(z-z')} \\ \dfrac{-j}{k_\rho^2}\left[\left(\dfrac{\mu_i}{\mu_j}\right)k_{zj}\tilde{R}_{j,j+1}^{TE}A_j^{TE} - k_{zi}\tilde{R}_{j,j+1}^{TM}A_j^{TM}\right]e^{jk_{zj}(z-z')}e^{-jk_{zj}2z_{j-i}} \end{Bmatrix} \tag{2.80}$$

Note that (μ_i/μ_j) term in (2.78), accounts for the continuity of H_z component of the magnetic field. The spectral-domain representation of scalar potential, $\tilde{G}_x^q$, can be obtained by considering the continuity of field components between layer transitions and using (2.41),

$$\tilde{G}_x^q = \frac{1}{2j\varepsilon_j k_{zi}}\begin{Bmatrix} \left[-\dfrac{k_{zi}k_{zj}}{k_\rho^2}A_j^{TM} + \dfrac{k_j^2}{k_\rho^2}\left(\dfrac{\mu_i}{\mu_j}\right)A_j^{TE}\right]e^{-jk_{zj}(z-z')} \\ +\left[\dfrac{k_{zi}k_{zj}}{k_\rho^2}\tilde{R}_{j,j+1}^{TM}A_j^{TM} + \dfrac{k_j^2}{k_\rho^2}\left(\dfrac{\mu_i}{\mu_j}\right)\tilde{R}_{j,j+1}^{TE}A_j^{TE}\right]e^{jk_{zj}(z-z')}e^{-jk_{zj}2z_{j-i}} \end{Bmatrix} \tag{2.81}$$

where A_j^{TE} and A_j^{TM} are evaluated using (2.71) iteratively.

Spectral-domain Green's functions for vertical electric fields in layer-*j* are obtained using the same procedure as follows:

$$\tilde{G}_{zz}^{A} = \frac{\mu_j}{2jk_{zi}}A_j^{TM}\left[e^{-jk_{zj}(z-z')} + \tilde{R}_{j,j+1}^{TM}e^{jk_{zj}(z-z')}e^{-jk_{zj}2z_{j-i}}\right] \tag{2.82}$$

where A_j^{TM} is evaluated using $A_i^{+TM} = M_i^{TM}\left(1+e^{-jk_{zi}2z'}\tilde{R}_{i,i-1}^{TM}\right)$ and (2.71).

$$\tilde{G}_z^q = \frac{1}{2j\varepsilon_j k_{zi}}A_j^{TM}\left(\frac{k_{zj}}{k_{zi}}\right)\left[e^{-jk_{zj}(z-z')} - \tilde{R}_{j,j+1}^{TM}e^{jk_{zj}(z-z')}e^{-jk_{zj}2z_{j-i}}\right] \tag{2.83}$$

where A_j^{TM} is evaluated using $A_i^{+TM} = M_i^{TM}\left(1+e^{-jk_{zi}2z'}\tilde{R}_{i,i-1}^{TM}\right)$ and (2.71).

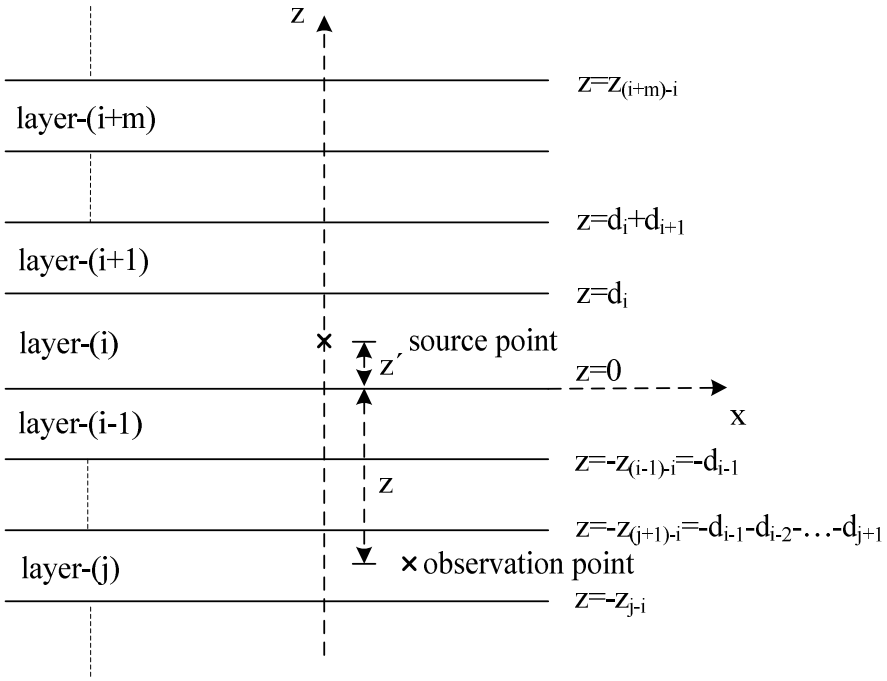

Figure 2.4: A general planar multilayer structure. Source layer = layer-(i); observation layer = layer-(j), where j < i

Green's Functions for Observation Layer below Source Layer

For the sake of illustration, a general planar stratified medium is given in Fig. 2.4, where a general source is located in layer-*i* and observation point is in layer-*j,* which is below the source layer. The field expressions (for TE and TM waves) in layer-*j* is assumed to be in the form of [43]

$$\tilde{F} = A_j \left[e^{jk_{zj}(z-z')} + \tilde{R}_{j,j-1}\, e^{-jk_{zj}(z-z')}\, e^{-jk_{zj}2(z_{j-1}+z')} \right] \tag{2.84}$$

where $\tilde{F}$ denotes the spectral-domain representation of the field expressions, A_j is the amplitude of the down-going waves in layer-*j* to be determined and z_{j-i} is the distance from the origin to the lower interface of the observation layer *j*, [40]. Starting from the amplitude

of the fields in source layer, A_i^- for down-going waves, one can determine the amplitudes of the fields in any layer iteratively using

$$A_{i-1}\, e^{-jk_{z(i-1)}z'} = A_i^- e^{-jk_{zi}z'} \underbrace{\frac{T^{i,i-1}}{1-\tilde{R}^{i-1,i-2}R^{i-1,i}\, e^{-jk_{z(i-1)}2d_{i-1}}}}_{\Gamma^{i,i-1}} \tag{2.85}$$

for the layers below the source layer.

Note that the term denoted by $\Gamma^{i,i-1}$ describes the transmission from the bottom of layer-*i* to the top of layer-(*i*-1). Therefore, it is quite easy to generalize the transfer function from layer-*i* to layer-*j*, for *j*<*i*, as

$$A_j e^{jk_{zj}(z_{(j+1)-(i-1)}-z')} = A_i^-\, e^{-jk_{zi}z'} \underbrace{\left(\prod_{n=i}^{j+2}\Gamma^{n,n-1}e^{-jk_{z(n-1)}d_{n-1}}\right)}_{=1\ for\ j+2>i}\Gamma^{j+1,j} \tag{2.86}$$

where $z_{(j+1)-(i-1)} = -\sum_{n=i-1}^{j+1} d_n$, and it is equal to zero for *j*=*i*-1.

The derivation of the spectral-domain Green's functions for this case is similar to the approach used for the case where observation layer is above the source layer, therefore without giving the details, the spectral-domain Green's functions for observation layer-*j* and associated amplitudes of the down-going wave in the source layer, layer-*i*, are obtained as follows:

$$\tilde{G}_{xx}^A = \frac{\mu_j}{2jk_{zi}}A_j^{TE}\left[e^{jk_{zj}(z-z')} + \tilde{R}_{j,j-1}^{TE}e^{-jk_{zj}(z-z')}e^{-jk_{zj}2z_{j-i}}\right] \tag{2.87}$$

$$-\frac{1}{jk_x}\tilde{G}_{zx}^A = \frac{\mu_j}{2jk_{zi}}\left\{\begin{array}{l}\dfrac{j}{k_\rho^2}\left[-\left(\dfrac{\mu_i}{\mu_j}\right)k_{zj}A_j^{TE} - k_{zi}A_j^{TM}\right]e^{jk_{zj}(z-z')} \\ +\dfrac{j}{k_\rho^2}\left[\left(\dfrac{\mu_i}{\mu_j}\right)k_{zj}\tilde{R}_{j,j-1}^{TE}A_j^{TE} - k_{zi}\tilde{R}_{j,j-1}^{TM}A_j^{TM}\right]e^{-jk_{zj}(z-z')}e^{-jk_{zj}2z_{j-i}}\end{array}\right\} \tag{2.88}$$

$$\tilde{G}_x^q = \frac{1}{2j\varepsilon_j k_{zi}} \left\{ \begin{array}{l} \left[\frac{k_{zi}k_{zj}}{k_\rho^2} A_j^{TM} + \frac{k_j^2}{k_\rho^2}\left(\frac{\mu_i}{\mu_j}\right) A_j^{TE} \right] e^{jk_{zj}(z-z')} \\ + \left[-\frac{k_{zi}k_{zj}}{k_\rho^2} \tilde{R}_{j,j-1}^{TM} A_j^{TM} + \frac{k_j^2}{k_\rho^2}\left(\frac{\mu_i}{\mu_j}\right) \tilde{R}_{j,j-1}^{TE} A_j^{TE} \right] e^{-jk_{zj}(z-z')} e^{-jk_{zj}2z_{j-i}} \end{array} \right\} \tag{2.89}$$

where A_j^{TM} is evaluated using $A_i^{-TM} = M_i^{TM}\left(-1 + e^{-jk_{zi}2(d_i - z')}\tilde{R}_{i,i+1}^{TM}\right)$ and A_j^{TE} is evaluated using $A_i^{-TE} = M_i^{TE}\left(1 + e^{-jk_{zi}2(d_i - z')}\tilde{R}_{i,i+1}^{TE}\right)$, together with (2.86).

$$\tilde{G}_{zz}^A = \frac{\mu_j}{2jk_{zi}} A_j^{TM}\left[e^{jk_{zj}(z-z')} + \tilde{R}_{j,j-1}^{TM} e^{-jk_{zj}(z-z')} e^{-jk_{zj}2z_{j-i}}\right] \tag{2.90}$$

where A_j^{TM} is evaluated using $A_i^{-TM} = M_i^{TM}\left(1 + e^{-jk_{zi}2(d_i - z')}\tilde{R}_{i,i+1}^{TM}\right)$ and (2.86).

$$\tilde{G}_z^q = \frac{1}{2j\varepsilon_j k_{zi}} A_j^{TM}\left(\frac{k_{zj}}{k_{zi}}\right)\left[e^{jk_{zj}(z-z')} - \tilde{R}_{j,j-1}^{TM} e^{-jk_{zj}(z-z')} e^{-jk_{zj}2z_{j-i}}\right] \tag{2.91}$$

where A_j^{TM} is evaluated using $A_i^{-TM} = M_i^{TM}\left(1 - e^{-jk_{zi}2(d_i - z')}\tilde{R}_{i,i+1}^{TM}\right)$ and (2.86).

2.2.2 Closed-form Spatial-Domain Green's Functions

Spatial-domain Green's functions are obtained from the inverse Hankel transform of the spectral-domain Green's functions as defined;

$$G = \frac{1}{4\pi}\int_{SIP} dk_\rho k_\rho H_0^{(2)}(k_\rho \rho)\tilde{G}(k_\rho) \tag{2.92}$$

where $k_\rho^2 = k_x^2 + k_y^2$, ρ is the variable in cylindrical coordinate system, G and $\tilde{G}$ are Green's functions in the spatial and spectral domain, respectively, $H_0^{(2)}$ is the Hankel function of the second kind and *SIP* is the Sommerfeld integration path. Note that this integral, also called Sommerfeld integral [41], can not be evaluated analytically for the spectral-domain Green's functions. They are evaluated by using asymptotic methods like the stationary phase and the method of steepest descent [40] or numerical methods [44]. Since the asymptotic methods require re-formulation of integral for different geometries, they are not appropriate for a

general purpose EM based simulators. As previously mentioned, numerical integration of the Sommerfeld integral is computationally expensive due to oscillatory nature of the integral and singularities encountered in the integration process.

To eliminate the disadvantages of asymptotic methods and numerical methods, the spectral-domain Green's functions are approximated by complex exponentials, whose Hankel transforms can be evaluated analytically, thus closed-form spatial domain Green's functions can be obtained [23,26].

In the approximation of spectral-domain Green's function, the GPOF method, which is based on uniform sampling along the range of approximation and solving a generalized eigenvalue problem, is used [45]. During the approximation process, spectral-domain Green's functions are sampled uniformly along a deformed path from the *SIP* as defined in Fig. 2.5. This path consists of three connected paths denoted as C_{ap1}, C_{ap2} and C_{ap3}, respectively, and the equations representing the paths are given as follows:

$$\text{For } C_{ap3}: \quad k_{zi} = -jk_i[T_{o1} + T_{o2} + t] \qquad 0 \le t \le T_{o3} \tag{2.93}$$

$$\text{For } C_{ap2}: \quad k_{zi} = -jk_i[T_{o1} + t] \qquad 0 \le t \le T_{o2} \tag{2.94}$$

$$\text{For } C_{ap1}: \quad k_{zi} = k_i[-jt + (T_{o1} - t) / T_{o1}] \qquad 0 \le t \le T_{o1} \tag{2.95}$$

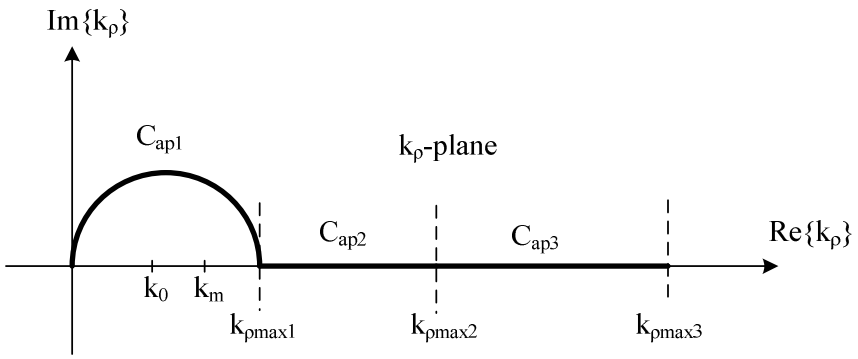

Figure 2.5: The deformed SIP path used in the approximation

where t is the running variable sampled uniformly on the corresponding ranges, T_{o1}, T_{o2} and T_{o3}. Two-level approach, which uses first and second connected paths, is sufficient to approximate smooth functions. However, spectral-domain Green's functions with fast variations locally require the use of three-level approach resulting in taking less number of samples than the samples taken in the case of two-level approach. In this thesis, both approaches are used interchangeably, depending on the behavior of the spectral-domain Green's functions [42].

Approximation process begins with fixing the parameters in the analytical formulation of spectral-domain Green's functions such as z and z' in order to get the values of the function at the sampling points. Then, GPOF method is used to obtain complex exponentials partially. In the first step, complex exponentials for third path is obtained and its contribution is extracted from the original function by simply subtracting the sum of exponentials from the original function. The same procedure is applied for the resulting function along second and first paths. Finally, three set of complex exponentials are obtained as

$$\widetilde{G} \cong \left\{ \sum_{n=1}^{N_1} a_{1n} e^{-b_{1n} k_z} + \sum_{n=1}^{N_2} a_{2n} e^{-b_{2n} k_z} + \sum_{n=1}^{N_3} a_{3n} e^{-b_{3n} k_z} \right\} \tag{2.96}$$

where N_i is the number of exponentials used in the approximation along path-i and, a_{in}'s and b_{in}'s are complex numbers in general. Then each exponential term in (2.96) is transformed to the spatial-domain, then by employing the Sommerfeld identity

$$\frac{e^{-jkr}}{r} = \frac{1}{2j} \int_{SIP} dk_\rho k_\rho H_0^{(2)}(k_\rho \rho) \frac{e^{-jk_z|z|}}{k_z} \tag{2.97}$$

spatial-domain Green's functions are obtained in their closed-forms as follows:

$$\widetilde{G} \cong \left\{ \sum_{n=1}^{N_1} a_{1n} \frac{e^{-jk_i r_{1n}}}{r_{1n}} + \sum_{n=1}^{N_{21}} a_{2n} \frac{e^{-jk_i r_{2n}}}{r_{2n}} + \sum_{n=1}^{N_3} a_{3n} \frac{e^{-jk_i r_{3n}}}{r_{3n}} \right\} \tag{2.98}$$

where $r_{in} = \sqrt{\rho^2 - b_{in}^2}$ is a complex distance and $\rho = \sqrt{x^2 + y^2}$.

Although adding the contributions of surface wave poles and real images improve the exponential approximation technique, by making spectral-domain Green's functions well-behaved and rapidly converging, their contributions are small for geometries on a thin substrate. Also it is not possible to find quasi-dynamic images for multilayer planar structures analytically except for some simple cases. In the light of these facts, for a general purpose algorithm, the closed-form spatial Green's functions are obtained for a multilayer media, without extracting the surface wave poles and real images contributions.

As an example, consider a three-layer geometry shown in Fig. 2.6 for which the Green's function of the vector and scalar potentials due to an HED and a VED at the substrate-air interface are obtained in closed forms. The magnitude plots of the spatial-domain Green's functions of vector potential, $G_{xx}^{A}, G_{zx}^{A}, G_{zz}^{A}$ and plots of the Green's functions of scalar potential, G_{x}^{q} and G_{z}^{q} are given in Figs. 2.7 and 2.8, respectively. Note that k_0 and ρ used in the figures are the free-space wave number and cylindrical spatial distance from the source, respectively.

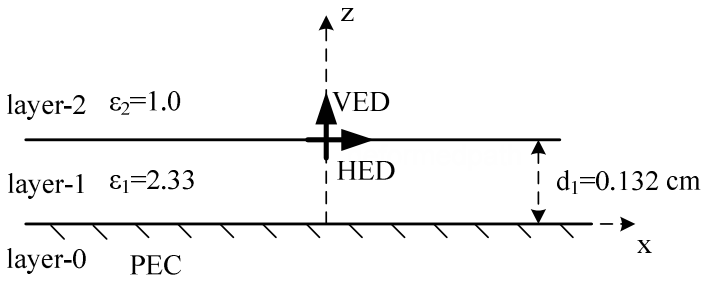

Figure 2.6: A typical 3-Layer Geometry

Since the contribution of surface wave poles are in the form of cylindrical waves and since the contributions of the real or complex images are in the form of spherical waves and dominate in the middle range, breakpoints may occur in the figures as it can be seen easily in G_{xx}^{A} plot. Those breakpoints show the transitions of the waves from spherical to cylindrical forms.

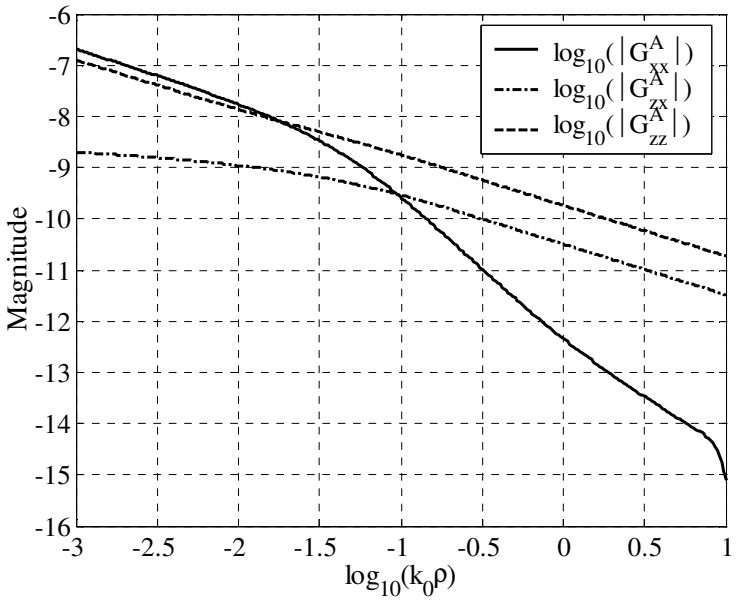

Figure 2.7: Magnitude of the Green's functions of vector potential, $G_{xx}^{A}, G_{zx}^{A}, G_{zz}^{A}$, for the geometry given in Fig. 2.6 at 1.0 GHz, Source layer = layer-1, $z = z' = 0.132$ cm

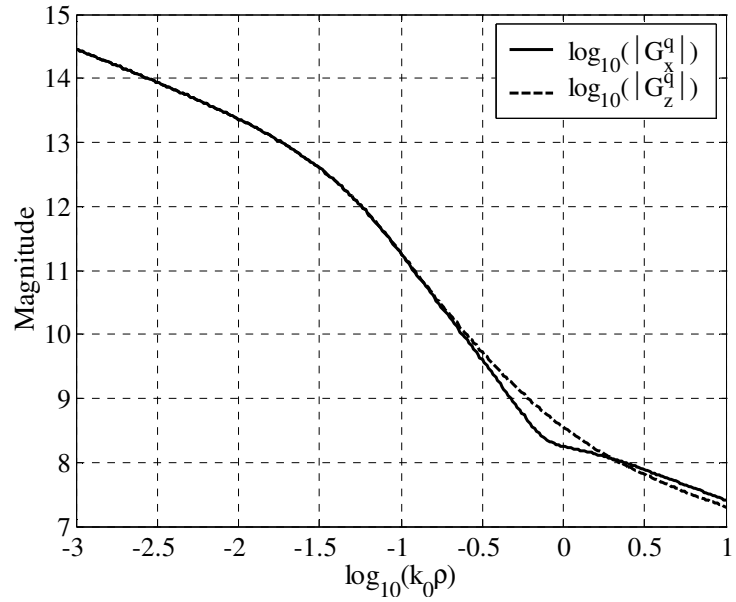

Figure 2.8: Magnitude of the Green's functions of scalar potential, G_x^q and G_z^q, for the geometry given in Fig. 2.6 at 1.0 GHz, Source layer = layer-1, $z = z' = 0.132$ cm

Chapter 3

Theory – MoM and Circuit Parameters

Since the main numerical technique used throughout the thesis is based on the spatial-domain MoM, its formulation is presented in this chapter, starting with the general procedure of MoM as applied to a general linear operator equation. Once the method is briefly reviewed in a general setting, its application to the solution of MPIE is discussed, with due emphasis to the basis functions used to represent the unknown function under the integral operator of MPIE, which is the electric current density **J** defined on the printed conductors. As the application of MoM to the governing integral equation results in the unknown surface current density, the calculation of circuit parameters from the current density are provided next. Circuit parameters refer to the port parameters of multi-port microwave circuits, like S-parameters, Z-parameters and input impedance, and to the radiation properties of antennas, like polarization and radiation patterns, beam-width and side-lobe levels. Finally, some numerical examples are provided to validate the formulations.

3.1 The Method of Moments

The method of moments, also known as weighted residue method, is a numerical tool to solve operator equations for unknown functions. It basically converts the operator equation into a set of linear algebraic equations, whose solution is much easier to obtain numerically; either by standard LU decomposition or by employing some iterative algorithms. The central idea of the MoM is to write the unknown function in terms of known functions (basis functions) with unknown coefficients, by which the domain of operator is discretized and the

operator equation is converted to algebraic equations with unknown coefficients. As an illustration, consider an inhomogeneous operator equation

$$Lf(x) = g(x) \tag{3.1}$$

where L is a linear operator, such as, differential, integral or integro-differential operator in electromagnetic problems, f is the unknown function to be determined, and g is the known forcing function, also referred to as excitation function. To solve (3.1) for the unknown function f, it is expanded in a series of linearly independent known basis functions f_1, f_2, f_3, … in the domain of L, as

$$f(x) = \sum_{n=1}^{N} \alpha_n f_n(x) \tag{3.2}$$

where α_n s are the unknown coefficients to be determined, and N is the number of basis functions employed to approximate the unknown function $f(x)$. In fact, for exact solutions N goes to infinity and the f_n form a complete set of basis functions. For approximate solutions, the summation given is usually a finite summation. By substituting (3.2) in (3.1), and using the linearity of L, the following equation is obtained.

$$\sum_{n=1}^{N} \alpha_n Lf_n(x) = g(x) \tag{3.3}$$

A suitable inner product $< f, g >$ is chosen for the problem. Then a set of linearly independent weighting (or testing) functions', w_1, w_2, w_3, … in the range of L are defined and the inner product of (3.3) whit each w_m is taken. The result is

$$\sum_{n=1}^{N} \alpha_n \langle w_m, Lf_n \rangle = \langle w_m, g \rangle \tag{3.4}$$

for $m = 1, 2, 3, \ldots$. This equation can be represented in matrix form as

$$[Z_{mn}][I_n] = [V_m] \tag{3.5}$$

where $Z_{mn} = \langle w_m, Lf_n \rangle$, $I_n = \alpha_n$ and $V_m = \langle w_m, g \rangle$. Z is called 'the MoM matrix', V is called 'the excitation vector' and I is the 'unknown current density'. When the basis and the testing

functions are the same functions, then the method is called as 'the Galerkin's method'. Note that, MoM matrices obtained with Galerkin's method are symmetric matrices.

There may be difficulties related to the method those may arise from the computation of the entries of *Z* matrix and *V* vector, the size and the realization of the condition of the *Z* matrix. One of the main tasks in these difficulties is the choice of the basis and testing functions.

3.2 MoM Formulation for the Solution of MPIE

The MPIE formulation for the analysis of printed structures in planar multilayer environment was derived in Section 2.1, and the original operational equations for the use of MoM procedure can be written as

$$E_x = -j\omega G_{xx}^A * J_x + \frac{1}{j\omega}\frac{\partial}{\partial x}\left(G^q * \nabla \cdot \mathbf{J}\right) \tag{3.6}$$

$$E_y = -j\omega G_{yy}^A * J_y + \frac{1}{j\omega}\frac{\partial}{\partial y}\left(G^q * \nabla \cdot \mathbf{J}\right) \tag{3.7}$$

$$E_z = -j\omega G_{zx}^A * J_x - j\omega G_{zy}^A * J_y - j\omega G_{zz}^A * J_z + \frac{1}{j\omega}\frac{\partial}{\partial z}\left(G^q * \nabla \cdot \mathbf{J}\right) \tag{3.8}$$

where

$$G^q * \nabla \cdot \mathbf{J} = G_x^q * \frac{\partial J_x}{\partial x} + G_y^q * \frac{\partial J_y}{\partial y} + G_z^q * \frac{\partial J_z}{\partial z} \tag{3.9}$$

Note that (3.6)-(3.8) together with (3.9) defines the integral equation, and the unknown function is the induced current density **J**. As the first step of the MoM, the unknown current density is expanded as linear combinations of suitable sub-domain basis functions;

$$J_x(x,y) = \sum_m \sum_n I_x^{(m,n)} B_x^{(m,n)}(x,y) \tag{3.10}$$

$$J_y(x,y) = \sum_m \sum_n I_y^{(m,n)} B_y^{(m,n)}(x,y) \tag{3.11}$$

$$J_z(x,y,z) = \sum_l I_z^{(l)} B_z^{(l)}(x,y,z) \tag{3.12}$$

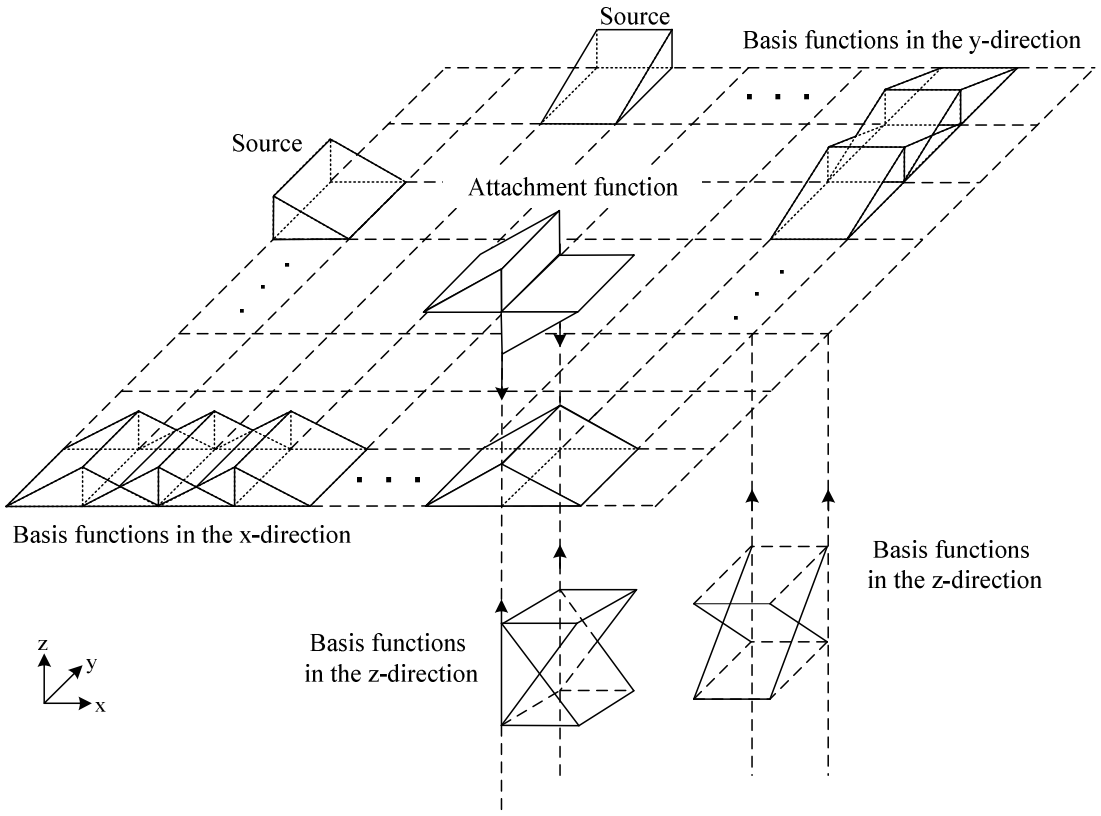

Figure 3.1: Typical basis functions used to represent current densities

where $B_x^{(m,n)}$, $B_y^{(m,n)}$ and $B_z^{(l)}$ are the basis functions with the unknown amplitudes $I_x^{(m,n)}$, $I_y^{(m,n)}$ and $I_z^{(l)}$, defined at (m, n)-th position on the subdivided horizontal conductor and at l-th position on the subdivided vertical conductor.

3.2.1 Choices of Basis Functions

In this thesis, two-dimensional rooftop functions, which are triangular functions in the longitudinal direction and uniform in the transverse direction, are chosen as the basis functions to represent the x and y components of the current density. Since sources and sinks are modeled as current filaments connected to the conductor, half-rooftop basis functions are

used to represent the induced currents at the points of connections of sources and sinks, as well as the z-component of the current density where the vertical conductors are connected to horizontal conductors or ground plane. In addition, to satisfy the charge continuity at each of the vertical and horizontal conductor intersections, saw-tooth basis (or attachment) functions are employed on the horizontal conductors. Note that the amplitudes of the attachment functions are chosen to satisfy the conservation of charges. Attachment function together with the vertical half-rooftop basis function form the basis function for the representation of the vertical current density at each of the intersection of the vertical and horizontal conductor. For the sake of illustration, the setup of discretization and the associated basis functions for a typical single layered geometry involving vertical strips are shown in Fig. 3.1.

Vertical basis functions employed in this study are either xz- or yz-spanning half-rooftop functions. In other words, they are used to represent the current density on vertical strips located at a constant y or constant x coordinate, respectively. As previously mentioned, at the intersections of each vertical and horizontal conductor, attachment functions are introduced in addition to sub-domain basis functions. Therefore, to distinguish these two types of vertical basis function and their associated attachment functions, the following expression is suggested and used throughout this work:

$$J_z(x,y,z) = \left(\sum_m \sum_l I_{z(l)}^{x(m,n)} B_{z(l)}^{x(m,n)}(y,z) + \sum_m \sum_n I_{xSP}^{(m,n)} B_{xSP}^{(m,n)}(x,y) \right) + \left(\sum_n \sum_k I_{z(k)}^{y(m,n)} B_{z(k)}^{y(m,n)}(x,z) + \sum_m \sum_n I_{ySP}^{(m,n)} B_{ySP}^{(m,n)}(x,y) \right) \quad (3.13)$$

where $B_{z(l)}^{x(m,n)}$ and $B_{xSP}^{(m,n)}$ represent the (l)-th z-directed yz-spanning basis function at $x = x_m$ and its associated (m,n)-th x-directed xy-spanning attachment function, respectively; in a similar manner, $B_{z(k)}^{y(m,n)}$ and $B_{ySP}^{(m,n)}$ represent the (k)-th z-directed xz-spanning basis function at $y = y_n$ and its associated (m,n)-th y-directed xy-spanning attachment function, respectively. Mathematical expressions for the vertical half-rooftop basis functions are given as

$$B_{z(l)}^{x(m,n)}(x,y,z)=\begin{cases}\dfrac{1}{h_y}\left(\dfrac{1}{h_z}\left|z-z_l\right|+1\right) & for\ \ z_l - h_z \le z \le z_l + h_z, x = x' = x_m, \\ & y_n - h_y \le y \le y_n + h_y \\ 0 & elsewhere\end{cases} \tag{3.14}$$

$$B_{z(k)}^{y(m,n)}(x,y,z)=\begin{cases}\dfrac{1}{h_x}\left(\dfrac{1}{h_z}\left|z-z_l\right|+1\right) & for\ \ z_k - h_z \le z \le z_k + h_z, y = y' = y_n, \\ & x_m - h_x \le x \le x_m + h_x \\ 0 & elsewhere\end{cases} \tag{3.15}$$

where h_x, h_y and h_z are the spans of the rooftop basis functions in the x and y directions and the span of the half-rooftop basis functions in the z direction respectively, as shown in Fig. 3.2.

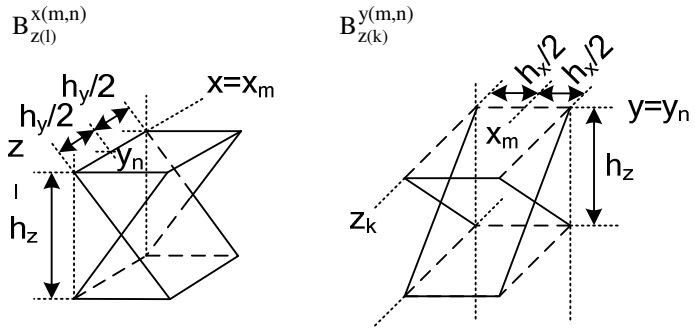

Figure 3.2: A detailed look at the vertical half rooftop basis functions

3.2.2 Charge Conservation and Current Continuity

The choice of the basis functions for the conductors of the geometries, which may involve both horizontal and vertical conductors, is quite straightforward: i) one needs to decide whether entire-domain or sub-domain basis functions are to be employed for the geometry to be analyzed; ii) if entire-domain basis functions are chosen, then include existing edge-singularities of the current density to ensure the accuracy of the current density; iii) if entire-domain basis functions are chosen, since the edge-singularities can be predicted automatically by the appropriate amplitudes of the basis functions, the convergence of the MoM matrix entries needs to be examined. However, when there are intersections of horizontal and vertical conductors, the choice of the basis functions at these junctions are not as straightforward. Continuity of the current and conservation of the charges need to be satisfied and the singularities of the basis functions denoting the horizontal and vertical current densities at these junctions needs to be examined carefully.

Basis functions are chosen to approximate the unknown current density in the formulation of MPIE. Derivatives of these functions represent the charge density due to continuity equation. Therefore, the chosen basis functions should ensure the continuity of the current as well as the conservation of the charges on the conductor.

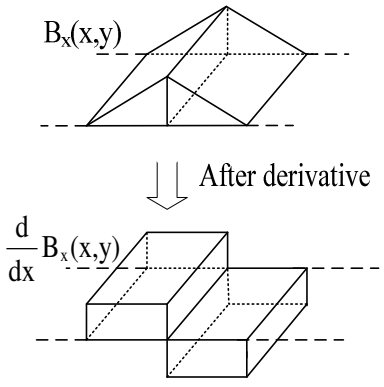

Figure 3.3: Rooftop basis function and its derivative

To see whether the chosen rooftop basis functions representing the current density over horizontal conductors are appropriate for the conservation of the charges, the function itself and its derivative is given in Fig. 3.3. Note that total charges corresponding to a rooftop basis function denoting the related part of the current along a conductor is zero, as it is observed from Fig. 3.3. Since the rooftop basis functions are defined over a rectangular cell, the current entering into and exiting from this cell are equal, and hence there is neither loss nor gain of charges in this region. Only source and sink basis functions which are chosen to be half-rooftop functions, can introduce finite total charges on the domain they are defined, provided that the impulse introduced by the differentiation of an half-rooftop basis function is ignored due to continuity of current which is shown in Fig. 3.4. Note that B_{xS} represents the *x*-directed horizontal source basis function.

After clarifying the question of what introduces the charge in the circuit, a consistent mathematical model for the basis functions at the junctions of vertical and horizontal conductors has to be developed. Starting with the basis functions defined at horizontal and vertical conductors, conservation of charges and the flow of current density is examined as shown in Fig. 3.5.

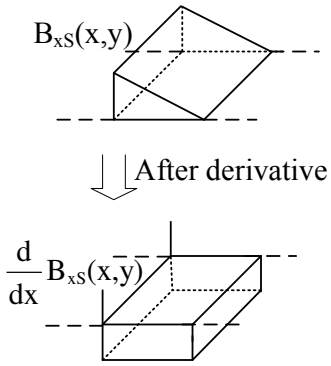

Figure 3.4: Half-rooftop basis function and its derivative

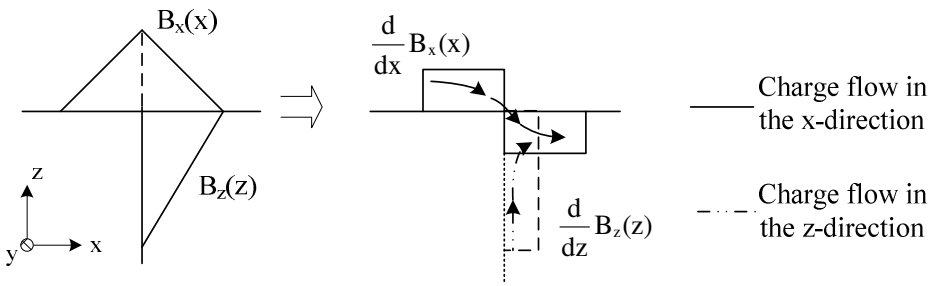

Figure 3.5: Current and charge densities for basis functions defined at junctions

It is obvious that half-rooftop vertical basis function introduces a finite amount of charge at the junction. Since only source and sink functions can inject charges in a circuit, conservation of charge, and in turn the continuity of current, is not achieved. Consequently, to achieve a flow of current between the horizontal and vertical conductors, one need to define a basis function over the domain, a part of which is on the horizontal conductor and the rest is on the vertical conductor. In addition, in order to satisfy the charge conservation, basis function defined over this domain should give birth to finite amount of charges on the vertical and horizontal conductors with opposite polarities. Examining all these requirements leads to definition of a saw-tooth basis (or attachment) function on the horizontal conductor over the same cell as the existing rooftop basis function, which is shown in Fig. 3.6. Note that, since the injection of charge is due to half-rooftop vertical basis function in the absence of attachment function, the amplitude of the attachment function should be related with the amplitude of the half-rooftop vertical basis function at the junction.

Basis functions and attachment function chosen for the current density at a junction are discontinuous right at the junction, and therefore their derivatives have impulse functions at the positions of discontinuities as shown in Fig. 3.6. These impulse functions can be interpreted as line charges in a physical manner and should be examined with utmost care for the accurate representation of the current density. In addition to these line charges, there exists a total net charge for each function. To satisfy the charge conservation at the junctions,

the amplitude of attachment function is chosen in such a way that the total net charge on the intersection due to both horizontal and vertical conductors is zero. Total net charges under the functions are proportional to the volume of derivatives of these functions and following equation can be written for the conservation of charges at the junction:

$$\left(I_{xSP}/h_x\right)2h_xh_y + \left(I_z/h_z\right)h_zh_y = 2I_{xSP} + I_z = 0 \tag{3.16}$$

Hence, to satisfy the conservation of charges at the junction, the amplitude of the saw-tooth attachment function should be chosen the negative half of the amplitude of the vertical basis function.

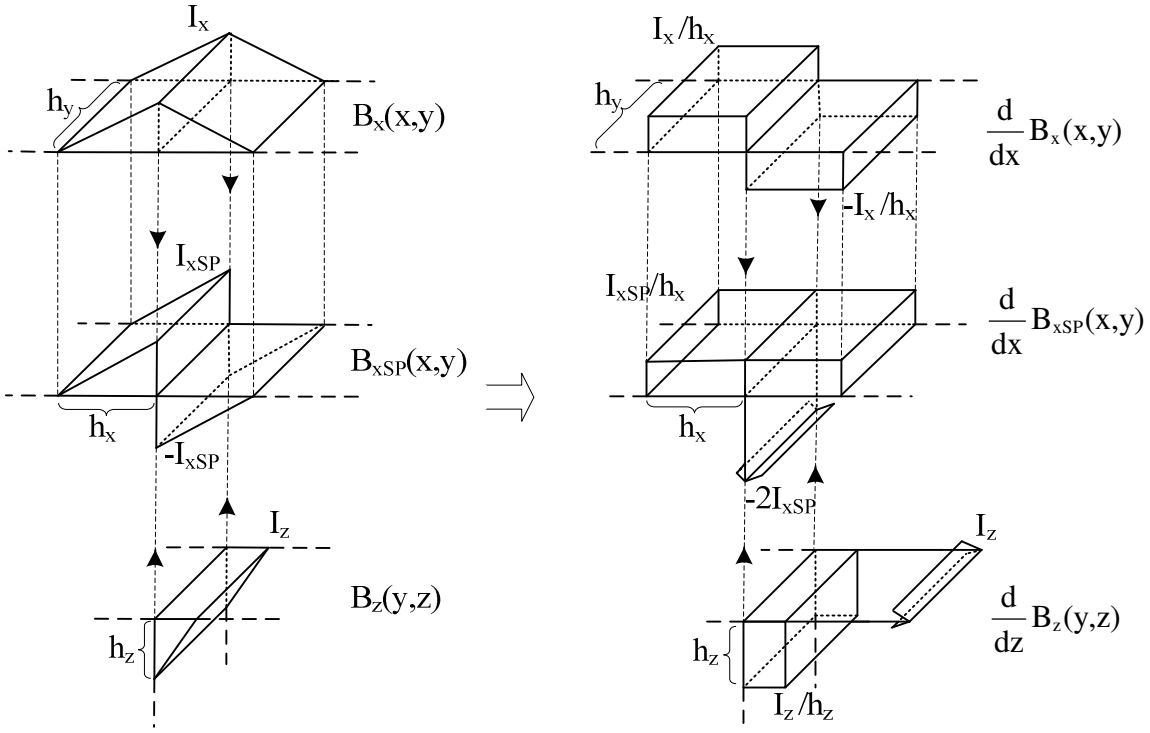

Figure 3.6: The rooftop horizontal basis function, saw-tooth attachment function and the half rooftop vertical basis function defined at the junctions of vertical and horizontal conductors

3.2.3 Testing Procedure

Once the current density is expanded in terms of known basis and attachment functions with unknown coefficients, the next step of the spatial-domain MoM is the substitution of Eqs. (3.10)-(3.12) and Eq. (3.16) into Eqs. (3.6)-(3.8), and then it is followed by the application of boundary conditions. Here the boundary conditions for the tangential components are implemented in integral sense through the well-known procedure of the MoM, where the electric field expressions are multiplied by known testing functions $T_x^{(m',n')}, T_y^{(m',n')}, T_z^{(l')}$ are integrated on the conductors and are set to zero. This leads to a matrix equation for the unknown amplitudes of the basis and attachment functions as

$$[\mathbf{Z}][\mathbf{I}] = [\mathbf{V}]$$

$$\begin{bmatrix} Z_{xx} & Z_{xy} & Z_{xz} \\ Z_{yx} & Z_{yy} & Z_{yz} \\ Z_{zx} & Z_{zy} & Z_{zz} \end{bmatrix} \begin{bmatrix} I_x \\ I_y \\ I_z \end{bmatrix} = \begin{bmatrix} V_x \\ V_y \\ V_z \end{bmatrix} \tag{3.17}$$

where, **Z** is the impedance matrix whose entries represent the mutual impedance between the basis and testing functions, **V** is the excitation vector and its elements represent the excitation voltages due to the current source(s) in the system, and finally **I** is the unknown current amplitude vector. Note that, Galerkin's method is used in this study which means testing functions are chosen to be same with the basis functions. For the sake of completeness, the typical entries of impedance matrix are given as follows:

$$Z_{xx}^{(m',n')(m,n)} = \left\langle T_x^{(m',n')}, G_{xx}^A * B_x^{(m,n)} \right\rangle + \frac{1}{\omega^2} \left\langle T_x^{(m',n')}, \frac{\partial}{\partial x} \left[G_x^q * \frac{\partial B_x^{(m,n)}}{\partial x} \right] \right\rangle \tag{3.18}$$

$$Z_{xy}^{(m',n')(m,n)} = \frac{1}{\omega^2} \left\langle T_x^{(m',n')}, \frac{\partial}{\partial x} \left[G_y^q * \frac{\partial B_y^{(m,n)}}{\partial y} \right] \right\rangle \tag{3.19}$$

$$Z_{xz}^{(m',n')(l)} = \frac{1}{\omega^2} \left\langle T_x^{(m',n')}, \frac{\partial}{\partial x} \left[G_z^q * \frac{\partial B_{z(l)}}{\partial z} \right] \right\rangle \tag{3.20}$$

$$Z_{yx}^{(m',n')(m,n)} = \frac{1}{\omega^2}\left\langle T_y^{(m',n')}, \frac{\partial}{\partial x}\left[G_x^q * \frac{\partial B_x^{(m,n)}}{\partial x} \right] \right\rangle \tag{3.21}$$

$$Z_{yy}^{(m',n')(m,n)} = \left\langle T_y^{(m',n')}, G_{yy}^A * B_y^{(m,n)} \right\rangle + \frac{1}{\omega^2}\left\langle T_y^{(m',n')}, \frac{\partial}{\partial y}\left[G_x^q * \frac{\partial B_y^{(m,n)}}{\partial y} \right] \right\rangle \tag{3.22}$$

$$Z_{yz}^{(m',n')(l)} = \frac{1}{\omega^2}\left\langle T_y^{(m',n')}, \frac{\partial}{\partial y}\left[G_z^q * \frac{\partial B_{z(l)}}{\partial z} \right] \right\rangle \tag{3.23}$$

$$Z_{zx}^{(l')(m,n)} = \left\langle T_{z(l')}, G_{zx}^A * B_x^{(m,n)} \right\rangle + \frac{1}{\omega^2}\left\langle T_{z(l')}, \frac{\partial}{\partial z}\left[G_x^q * \frac{\partial B_x^{(m,n)}}{\partial x} \right] \right\rangle \tag{3.24}$$

$$Z_{zy}^{(l')(m,n)} = \left\langle T_{z(l')}, G_{zy}^A * B_y^{(m,n)} \right\rangle + \frac{1}{\omega^2}\left\langle T_{z(l')}, \frac{\partial}{\partial z}\left[G_y^q * \frac{\partial B_y^{(m,n)}}{\partial y} \right] \right\rangle \tag{3.25}$$

$$Z_{zz}^{(l')(l)} = \left\langle T_{z(l')}, G_{zz}^A * B_{z(l')} \right\rangle + \frac{1}{\omega^2}\left\langle T_{z(l')}, \frac{\partial}{\partial z}\left[G_z^q * \frac{\partial B_{z(l')}}{\partial z} \right] \right\rangle \tag{3.26}$$

where $B_{z(l)}$ and $T_{z(l')}$ are the general representations of the basis and testing functions in the vertical directions including the associated attachment functions. According to the aforementioned definition of current density J_z in (3.13), matrix entries are rearranged in Appendix A. Note that $\langle , \rangle$ and $*$ denote the inner product and convolution operators, respectively, and their definitions are given as follows:

$$\langle f(x,y), g(x,y) \rangle = \iint dxdy f(x,y) \cdot g(x,y) \tag{3.27}$$

$$f(x,y) * g(x,y) = \iint dx'dy' f(x-x', y-y') g(x', y') \tag{3.28}$$

The entries of the excitation vector *V* have the same form; they are given in Appendix A in details. After having written the corresponding matrix entries explicitly in terms of inner product and convolution integrals, matrix entries are obtained as in the form of quadruple integrals of complex functions. In the evaluation of these quadruple integrals, analytical methods are used which were introduced by Alatan et al. [30]. Using analytical methods

instead of numerical techniques has significantly improved the computation time of matrix entries. Therefore, in Appendix B, the analytical evaluation of the matrix entries corresponding to different types of basis and/or testing functions are explained. After evaluation of inner product terms and substituting into (3.17), the current densities on the conductors are obtained by solving the matrix equation. Then, circuit parameters such as impedance parameters, scattering parameters and input impedance can be obtained from the current distribution.

In case of application of MoM to vertical metallizations, some difficulties arise. As previously discussed, line charges at the edge discontinuities significantly affect the accurate representation of current density and should be handled. Another difficulty originates from the z and z' dependency of the closed-form Green's functions for the vertical directions. Therefore in the following section, these difficulties and their solutions will be presented in details.

3.2.4 Difficulties and Solutions

The representative form of the spectral-domain Green's functions is given in Chapter 2 and it is mentioned that to be able to sample the function over the range of approximation, z and z' dependence of the functions should be fixed. Since the horizontal conductors are placed on constant z-planes, fixing z and z' is not a problem for the Green's functions to be evaluated at these planes only. However, the evaluations of the MoM matrix entries corresponding to the vertical metallizations require the integration over z and/or z'. Since these variables exist explicitly in the formulation of spectral-domain Green's functions associated with corresponding MoM matrix entries, the closed-form Green's functions, derived as described in Chapter 2, can not be used efficiently.

In this thesis, this difficulty is eliminated by simply integrating the function in spectral-domain over z and/or z', then applying the exponential approximation process. Since the z and z' dependence of the spectral-domain Green's functions is always in exponential form,

functions can be integrated analytically over z and/or z' for most basis functions. Therefore, the integration over z and z', which are due to the testing and convolution integrals along a vertical conductor, respectively, can be evaluated analytically in the spectral-domain, and then closed-form Green's functions corresponding to the result of this integrand can be obtained [46]. Resulting functions with the proposed technique are called *auxiliary functions* and the way of obtaining these functions for the corresponding spectral-domain Green's functions is demonstrated in Appendix B.

The exponential approximation with the GPOF method should be performed with the three-level approximation scheme, to handle the oscillatory behavior of the analytical integrations over z and z', as explained in Chapter 2. Note that, for the addition of multiple vertical metallizations having the same z and z' dependence does not require an additional exponential approximation, provided that all vertical metallizations employ the same number of basis functions. Moreover, there will be no additional computational cost by the addition of vertical metallizations to the system. This is because the interaction between a basis function on a horizontal or vertical conductor and a testing function on a vertical conductor is a function of horizontal coordinates, *i.e.* ρ, and the interaction between the same basis function and a testing function (or vice versa) located on another vertical conductor can be calculated by simply substituting ρ in the general formulation.

Another difficulty originates from the line charges due to discontinuities of the basis, testing and attachment functions. In this study, at the intersections of vertical and horizontal basis functions, line charges' contributions are assumed to cancel each other. In order to verify this statement, the following MoM matrix entry involving the vertical basis function and horizontal attachment function at a junction is considered:

$$Z_{yz}^{q} = -\frac{1}{2j\omega}\left\langle T_y(x,y), \frac{\partial}{\partial y}\left[G_x^q * \frac{\partial B_{ySP}(x,y)}{\partial y} \right] \right\rangle + \frac{1}{j\omega}\left\langle T_y(x,y), \frac{\partial}{\partial y}\left[G_z^q * \frac{\partial B_z(x,z)}{\partial z} \right] \right\rangle \quad (3.29)$$

where both vertical basis function B_z and horizontal attachment function B_{ySP} are discontinuous at the junction. Since the basis and attachment functions are discontinuous, their derivatives can be written as the sum of impulse and rectangular functions as follows:

$$Z_{yz}^{q} = -\frac{1}{2j\omega}\left\langle \frac{\partial}{\partial y}T_y(x,y), G_x^q * \left[\frac{\partial B_{ySP}(x,y)}{\partial y} - 2\delta_x(y-y_i, z-z_i)\right] + G_x^q * 2\delta_x(y-y_i, z-z_i)\right\rangle$$

$$+\frac{1}{j\omega}\left\langle \frac{\partial}{\partial y}T_y(x,y), G_z^q * \left[\frac{\partial B_z(y,z)}{\partial z} - \delta_x(y-y_i, z-z_i)\right] + G_z^q * \delta_x(y-y_i, z-z_i)\right\rangle \quad (3.30)$$

where $\delta_x(y-y_i, z-z_i)$ represents a line source in the *x*-direction. Once the terms are recombined, the following equation is obtained:

$$Z_{yz}^{q} = -\frac{1}{2j\omega}\left\langle \frac{\partial}{\partial y}T_y(x,y), G_x^q * \left[\frac{\partial B_{ySP}(x,y)}{\partial y} - 2\delta_x(y-y_i, z-z_i)\right]\right\rangle$$

$$+\frac{1}{j\omega}\left\langle \frac{\partial}{\partial y}T_y(x,y), G_z^q * \left[\frac{\partial B_z(y,z)}{\partial z} - \delta_x(y-y_i, z-z_i)\right]\right\rangle$$

$$+\frac{1}{j\omega}\left\langle \frac{\partial}{\partial y}T_y(x,y), \left\{G_z^q - G_x^q\right\}\right\rangle * \delta_x(y-y_i, z-z_i) \quad (3.31)$$

The last term in (3.31) can be neglected for small ρ values since $G_z^q \approx G_x^q$ at $z = z'$ as $\rho \to 0$, that is, the contribution of line charges due to discontinuities at the junctions are ignored. The behavior of the spatial-domain Green's functions of scalar potential are demonstrated in Fig. 3.7 for a substrate backed by a ground layer whose thickness is 0.132 cm and dielectric constant is 2.33 at the operating frequency of 1.0 GHz where the source is at the substrate-air interface. As it is observed from the figure, Green's functions of horizontal and vertical scalar potentials are close to each other for $\rho \to 0$.

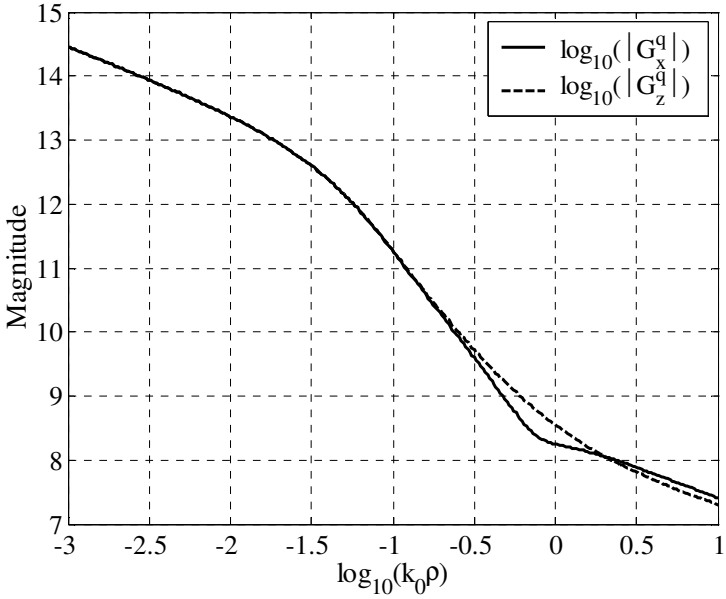

Figure 3.7: Magnitude of the Green's functions of scalar potential, G_x^q and G_z^q, for a substrate backed by a ground plane with a thickness of 0.132 cm and 2.33 dielectric constant at 1.0 GHz operation frequency

3.3 Source Models and Circuit Parameters

In this part, the problem of characterizing multiport planar microwave circuits with the MoM using two commonly encountered excitation models, the delta-gap voltage and the impressed-current source models will be studied. Impedance parameters characterizing general *M*-port planar microwave circuits will be obtained with the use of aforementioned source models.

3.3.1 Delta-Gap Voltage Source Model

This model assumes ideal voltage sources exciting each physical port of the planar circuit. The general port P_m (m=1,…, M) is excited by a voltage source of magnitude V_m^t, applied within an infinitesimally small gap of length $\delta \to 0$ and across the extended ground-plane and the tip of the mth feed-point [47], as shown in Fig. 3.8.

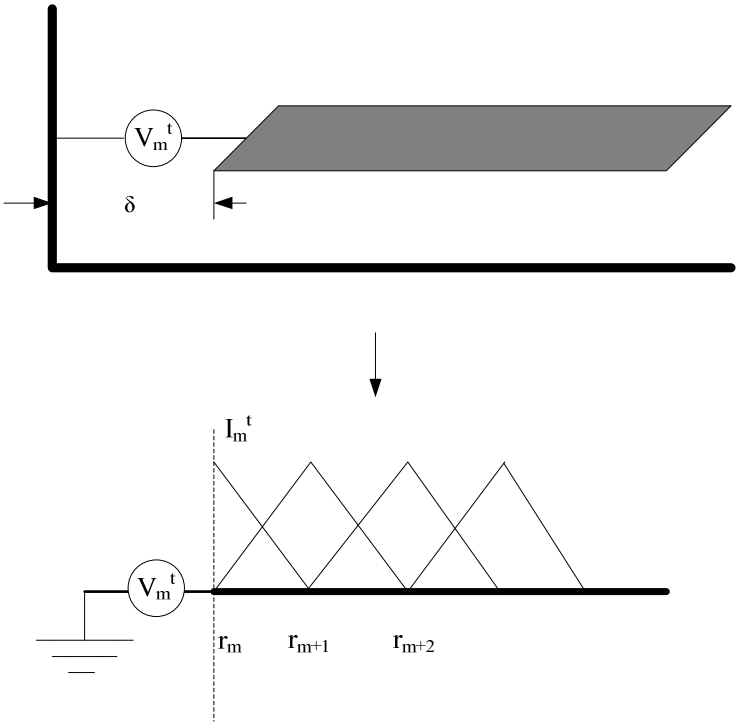

Figure 3.8: A delta-gap voltage source exciting the port #m and associated basis functions for the implementation of MoM

Corresponding basis functions to represent current densities on the conductor are also shown in Fig. 3.8. Note that current density at the terminal is also unknown since the port is excited with a voltage source. Incident field due to excitation of each port with a delta-gap source can be described as

$$\overline{E}^{inc} = V_m^t \delta(\bar{r} - \bar{r}_m)\hat{\alpha}_m \tag{3.32}$$

where $\bar{r}_m$ is the location of the port and $\hat{a}_m$ is the outward normal parallel to the corresponding feed-point. Now, within the framework of the MoM, the unknown current densities on the circuit and terminals are represented by the predefined basis functions as follows:

$$J_s(\bar{r}') = \sum_{m=1}^{M} I_m^t \bar{f}_m(\bar{r}') + \sum_{n=M+1}^{M+N} I_n^c \bar{f}_n(\bar{r}') \tag{3.33}$$

where $\overline{f}_m$ and $\overline{f}_n$ denote the basis functions for the terminal and circuit quantities with the unknown amplitudes I_m^t and I_n^c , respectively. Then, applying Galerkin's method for the testing procedure, block matrix form of the MoM matrix can be written as

$$[\mathbf{Z}][\mathbf{I}] = [\mathbf{V}]$$

$$\begin{bmatrix} Z^{tt} & Z^{tc} \\ Z^{ct} & Z^{cc} \end{bmatrix} \begin{bmatrix} I^t \\ I^c \end{bmatrix} = \begin{bmatrix} V^t \\ 0 \end{bmatrix} \tag{3.34}$$

where I^t represents the terminal currents and I^c stands for the induced current on the circuit. Current distribution on the circuit and terminals can be evaluated by solving the matrix equation (3.34). To have a better understanding, the submatrices in (3.34) are expanded as follows:

$$Z^{tt} = \begin{bmatrix} Z_{1,1} & Z_{1,2} & \cdots & Z_{1,M} \\ Z_{2,1} & Z_{2,2} & \cdots & Z_{2,M} \\ \vdots & \vdots & & \vdots \\ Z_{M,1} & Z_{M,2} & \cdots & Z_{M,M} \end{bmatrix} \qquad Z^{tc} = \begin{bmatrix} Z_{1,M+1} & Z_{1,M+2} & \cdots & Z_{1,M+N} \\ Z_{2,M+1} & Z_{2,M+2} & \cdots & Z_{2,M+N} \\ \vdots & \vdots & & \vdots \\ Z_{M,M+1} & Z_{M,M+2} & \cdots & Z_{M,M+N} \end{bmatrix}$$

$$Z^{ct} = \begin{bmatrix} Z_{M+1,1} & Z_{M+1,2} & \cdots & Z_{M+1,M} \\ Z_{M+2,1} & Z_{M+2,2} & \cdots & Z_{M+2,M} \\ \vdots & \vdots & & \vdots \\ Z_{M+N,1} & Z_{M+N,2} & \cdots & Z_{M+N,M} \end{bmatrix} \quad Z^{cc} = \begin{bmatrix} Z_{M+1,M+1} & Z_{M+1,M+2} & \cdots & Z_{M+1,M+N} \\ Z_{M+2,M+1} & Z_{M+2,M+2} & \cdots & Z_{M+2,M+N} \\ \vdots & \vdots & & \vdots \\ Z_{M+N,M+1} & Z_{M+N,M+2} & \cdots & Z_{M+N,M+N} \end{bmatrix}$$

$$I^t = \begin{bmatrix} I_1^t \\ I_2^t \\ \vdots \\ I_M^t \end{bmatrix} \qquad I^c = \begin{bmatrix} I_{M+1} \\ I_{M+2} \\ \vdots \\ I_{M+N} \end{bmatrix} \qquad V^t = \begin{bmatrix} v_1^t \\ v_2^t \\ \vdots \\ v_M^t \end{bmatrix} \qquad V^c = \begin{bmatrix} 0 \\ 0 \\ \vdots \\ 0 \end{bmatrix}$$

where $Z_{m,n}$ is the interaction between the basis-m and testing-n. Note that, since the Galerkin's method employed, resulting MoM matrix is a symmetric matrix.

The delta-gap voltage enables to get the terminal relations among the port voltages and currents directly. Indeed, if the MoM matrix is inverted as the following:

$$\begin{bmatrix} Y^{tt} & Y^{tc} \\ Y^{ct} & Y^{cc} \end{bmatrix} = \begin{bmatrix} Z^{tt} & Z^{tc} \\ Z^{ct} & Z^{cc} \end{bmatrix}^{-1} \tag{3.35}$$

Then $[Y^{tt}][V^t] = [I^t]$ and, therefore, sub-matrix $[Y^{tt}]$ is the required network admittance matrix $[Y^t]$, characterizing the given M-port circuit. Also network impedance matrix $[Z^t]$, characterizing the given M-port circuit, can be obtained as shown in below [47]

$$\begin{aligned} &Z^{tt}I^t + Z^{tc}I^c = V^t \\ &Z^{ct}I^t + Z^{cc}I^c = 0 \end{aligned} \Rightarrow \quad I^c = -\left[Z^{cc}\right]^{-1} Z^{ct} I^t \quad \Rightarrow \quad \underbrace{\left(Z^{tt} - Z^{tc}\left[Z^{cc}\right]^{-1} Z^{ct}\right)}_{Z^t} I^t = V^t$$

$$\left[Z^t\right] = \left[Z^{tt}\right] - \left[Z^{tc}\right]\left[Z^{cc}\right]^{-1}\left[Z^{ct}\right] \tag{3.36}$$

3.3.2 Impressed-Current Source Model

In the impressed-current source model, current sources with known magnitudes are assumed to be impressed at each port. The general port P_m (m=1,…, M) is excited by a current source of magnitude I_m^t, applied within an infinitesimally small gap of length $\delta \to 0$ and across the extended ground-plane and the tip of the mth feed-point [47], as shown in Fig. 3.9.

Since the current impressed at the terminals are known quantities, the induced current $\bar{J}_s$ can be expanded in terms of basis functions only for the circuit quantities. Now, within the framework of the MoM, the unknown current densities on the circuit are represented by the aforementioned basis functions as follows:

$$\bar{J}_s(\bar{r}') = \sum_{n=M+1}^{M+N} I_n^c \bar{f}_n(\bar{r}') \tag{3.37}$$

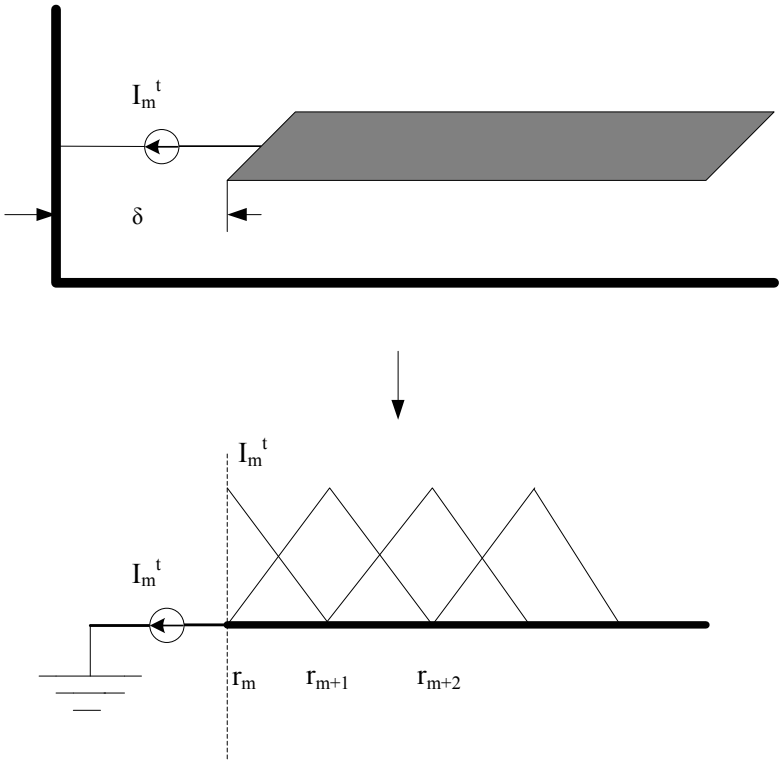

Figure 3.9: An impressed current source exciting the port #m and associated basis functions for the implementation of MoM

where $\bar{f}_n$ denote the basis functions for the circuit quantities with unknown current amplitudes I_n^c. By applying testing procedure as choosing the testing functions same with the basis functions (Galerkin's method), MoM impedance elements in matrix form are obtained:

$$\left[Z_{pq}^{cc}\right]\left[I_c^q\right] = -I_m^t\left[Z_{pm}^{ct}\right], \qquad (q,p) \in \{M+1,\ldots,M+N\} \tag{3.38}$$

where Z_{pq}^{cc} and Z_{pm}^{ct} are the same matrices with the impedance matrix **Z** whose typical entries are given in (3.18)-(3.26) and excitation matrix **V** corresponding to the general port P_m which is excited by the impressed current source I_m^t, respectively.

To determine the network impedance matrix entries, one port is excited at a time keeping the remaining ports open-circuited. Let the *n*th port be the excited one. Then the *n*th row of the network impedance matrix is determined by definition from the relation

$$Z_{mn}^{t} = \frac{V_m^t}{I_n^t} = -\frac{\int_{S_m} \overline{E}_{total}.d\bar{l}}{I_n^t} \tag{3.39}$$

where I_n^t is the impressed current at the *n*th port and V_m^t is the induced terminal voltage at the *m*th port. The field denoted as $\overline{E}_{total}$ is the tangential electric field generated by both the impressed-current $\bar{J}_n^{imp}$ and the induced circuit currents $\bar{J}_s$. To retrieve the required network impedance matrix, the induced terminal voltages have to be sampled out. This is achieved by setting the inner products between the total electric field $\overline{E}_{total}$ and the terminal testing functions, $\overline{w}_m$, which are chosen to be same as the terminal basis functions to zero everywhere, except for the location of the impressed and open-circuited current sources. Hence, following equation can be written for the induced terminal voltages [47]

$$\begin{aligned} V_m^t &= \left\langle \overline{w}_m, \overline{E}_{total} \right\rangle \\ &= Z_{mn} I_n + Z_{m,M+1} I_{M+1} + \ldots + Z_{m,M+N} I_{M+N}, \quad m = 1,\ldots,M \\ &= \left[Z^{tt}\right] I_n^t + \left[Z^{tc}\right]\left[I^c\right] \end{aligned} \tag{3.40}$$

where $Z_{m,n}$ is the mutual impedance between the basis-*m* and testing-*n*. In its more clear form, impedance parameters can be expressed as

$$Z_{(m,k)} = Z_{(m,k)}^{tt} + V^{(m)} \cdot I^{(k)}, \qquad m,k = 1,\ldots,M \tag{3.41}$$

where $Z_{(m,k)}$ is the (*m, k*)-th entry of impedance matrix, $Z_{(m,k)}^{tt}$ is the mutual impedance between the port-*m* and port-*k*, $V^{(m)}$ is the excitation vector for port-*m* and $I^{(k)}$ is the current distribution corresponding to excitation of port-*k* with a unity current source.

Scattering parameters characterizing the *M*-Port planar microwave circuit can be evaluated simply by

$$S = \left(Z^t / Z_0 - \mathbf{I}\right)\left(Z^t / Z_0 + \mathbf{I}\right)^{-1} \tag{3.42}$$

where Z_0 is the reference impedance parameter for the circuit and '**I**' is the M by M identity matrix.

3.4 Numerical Examples

In this section, the application of formulation presented in this thesis is demonstrated on several examples and results are compared with those presented in the literature and obtained from commercial EM analysis software *em* by Sonnet.

The main difference between *em* and this formulation is that *em* puts the circuit in a conducting box whose default wall conductivities are infinite [48]. The analysis of radiating structures in *em* requires adding loss to the system, but with the formulation presented here these structures can be characterized better, in the sense of accuracy.

3.4.1 Microstrip Single-stub Filter

To validate the GPOF-based approximation of Green's functions and characterizing the multiport passive microwave circuits, the formulation described in this study is first applied to a microstrip single-stub filter [47], as shown in Fig. 3.10. The bottom layer is a ground plane. The dielectric constant of the substrate, ε_r, is 2.33. The substrate thickness, h, is 0.157 cm. The microstrip lines are placed at the top of the substrate and the upper layer is free space.

Normalized (with respect to 50 Ω reference impedance) S_{AA} and S_{BA} parameters for the single-stub filter are obtained using the MoM approach and compared to the results of the commercial software package *em* by Sonnet. Figures 3.11 and 3.12 show the magnitudes of S_{AA} and S_{BA}, respectively. The results are in good agreement with each other, except for the resonance frequencies. In case of S_{BA}, there exists an approximately 8 dB difference between the plots near the resonant frequency which is about 2.8 GHz. This is likely related to the *em* by Sonnet surrounds the structure with a closed conducting box while the method proposed here solves the system in open environment.

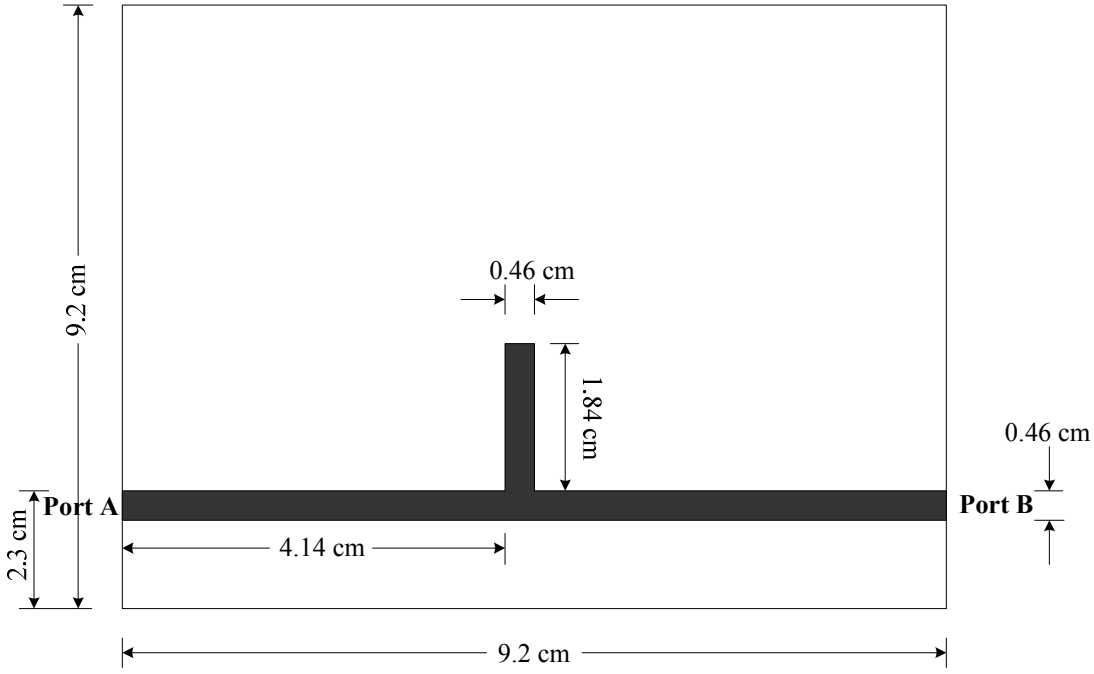

Figure 3.10: Geometry of the single-stub filter

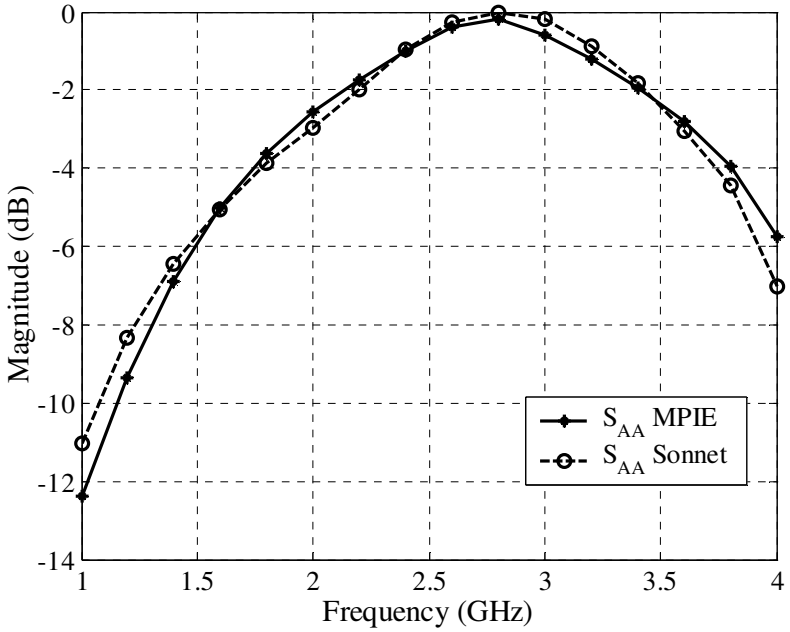

Figure 3.11: Magnitude of S_{AA} of the single-stub filter shown in Fig. 5.1

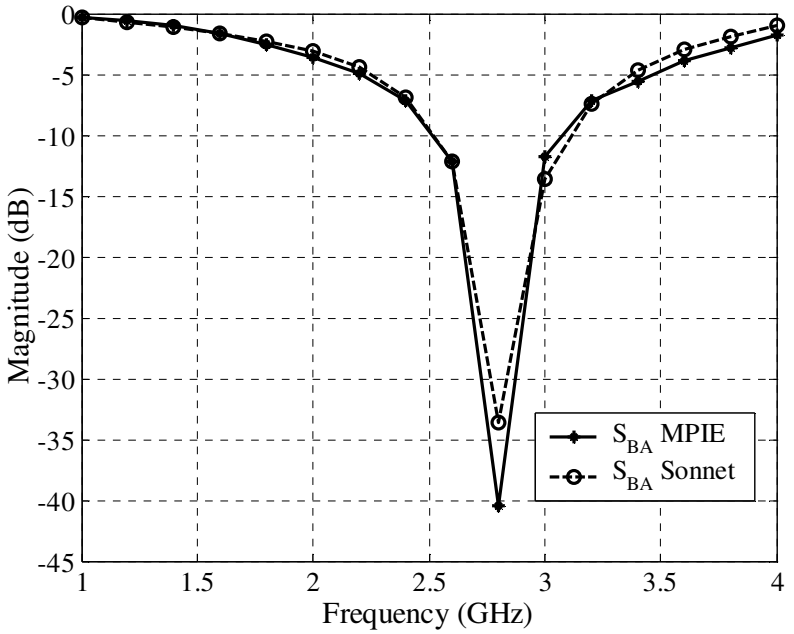

Figure 3.12: Magnitude of S_{BA} of the single-stub filter shown in Fig. 5.1

3.4.2. Probe-Fed Microstrip Patch Antenna with/without Shorting Strip

In this example, by using the method presented in this thesis, the probe-fed microstrip patch antennas are rigorously analyzed by considering the radiation, electromagnetic couplings and fringing fields.

The MoM formulation is first applied to a single layer microstrip patch antenna with wide vertical feed extended in x-direction, as shown in Fig. 3.14. The parameters for the first antenna are: a = 8.0 cm, b = 10.0 cm, x_p = 4.0 cm, y_p = 3.0 cm and d = 1.0 cm. The dielectric constant of the substrate is, ε_r, 1.0 and the thickness of the substrate is 0.6 cm. Side view of the patch antenna used in this study is shown in Fig. 3.13. For this antenna, the resonant frequency is obtained using the MoM approach, and compared to the results of the available techniques such as the cavity model and the hybrid model; and the experimental results, which are presented in [49]. The resonant frequencies obtained from the MoM solution, the techniques and experimental measurement in [49] are given in Table 3.1. For the sake of

completeness, the magnitude plot of the input reflection coefficient evaluated with MoM technique is shown in Fig. 3.15.

Table 3.1: Calculated and measured resonant frequencies for the probe-fed patch antenna

Case	f_r (GHz)	$\|\Gamma in\|$
Cavity Model	1.37	0.335
Zero Determinant	1.51	-
Hybrid Model	1.35	0.367
Experiment	1.34	0.414
MoM Solution	1.34	0.314

From these results, it is observed that the resonant frequency obtained from the MoM approach is in good agreement with those obtained from the available techniques and experimental measurement. As a comparison, the hybrid model represents the current density along the discretized vertical conductor in terms of pulse basis functions whereas the MoM formulation introduces two half rooftop basis functions on the conductor along the vertical direction. Hence, the magnitudes of the input reflection coefficients obtained from the hybrid model and the MoM solution exhibit slight differences near the resonant frequencies.

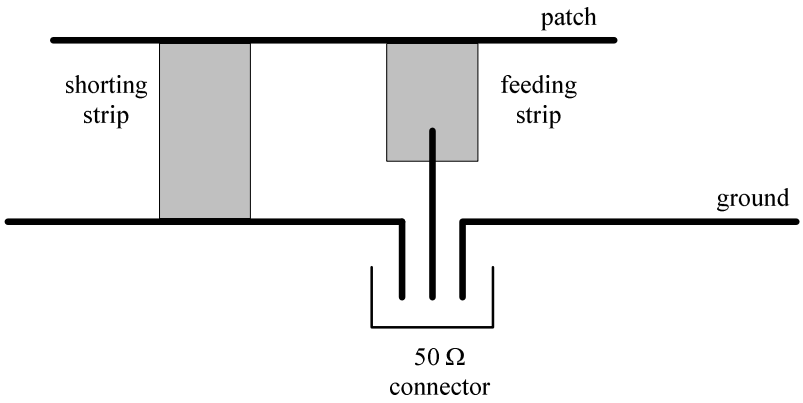

Figure 3.13: Side view of antennas used in the experiments

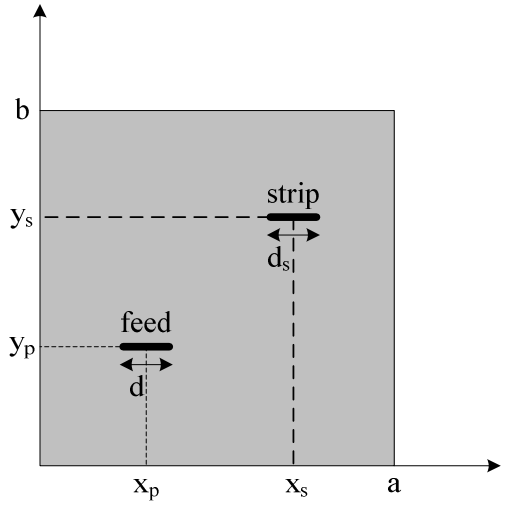

Figure 3.14: Top view of a vertical-fed patch with a shorting strip

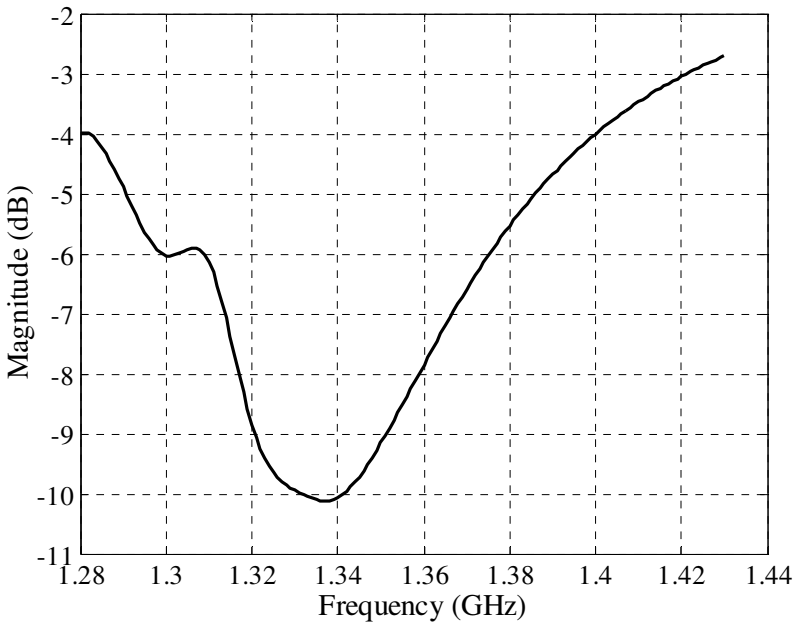

Figure 3.15: Magnitude of reflection coefficient of the patch antenna with vertical feed

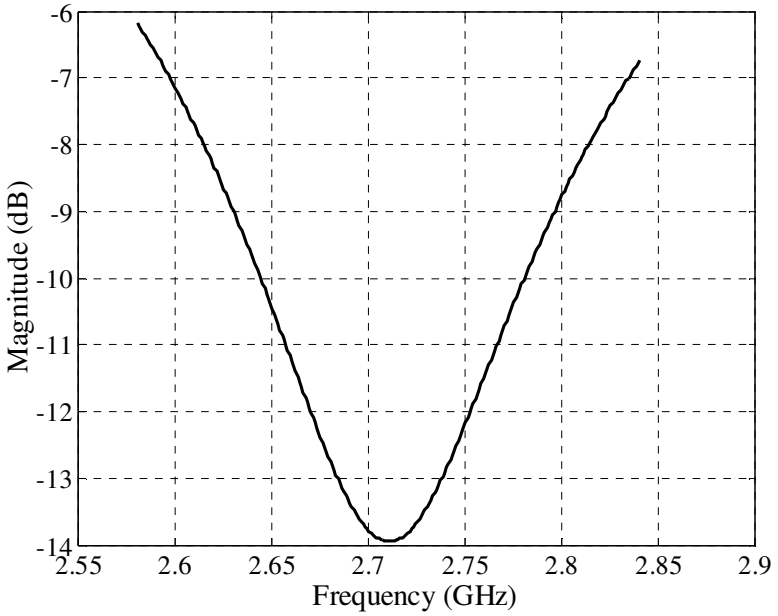

Figure 3.16: Magnitude of reflection coefficient of the patch antenna with vertical feed and shorting strip

After analyzing the probe-fed microstrip antenna, MoM solution is now applied to a microstrip antenna with wide vertical feed and a shorting strip. The parameters for the shorted antenna are: a = 5.0 cm, b = 6.0 cm, x_p = 2.4 cm, y_p = 0.0 cm, x_s = 2.5 cm, y_s = 1.0 cm, d = 0.45 cm and d_s = 1.0 cm. The dielectric constant of the substrate is, ε_r, 1.0 and the thickness of the substrate is 0.65 cm. The resonant frequencies obtained from MoM solution and those acquired from [49], are given in Table 3.2. And also the magnitude plot of the input reflection coefficient is shown in Fig. 3.16.

Table 3.2: Resonant frequencies and the corresponding reflection coefficients of the probe-fed patch antenna with shorted strip

Case	f (GHz)	$\|\Gamma in\|$
Zero Determinant	2.87	-
Hybrid Model	2.84	0.113
Experiment	2.74	0.132
MoM Solution	2.72	0.204

From the Table 3.2, it is observed that the input reflection coefficients obtained from the MoM solution and the experimental result are not in good agreement. This is because, in the solution of MoM, the vertical feeds and the shorting strips are modeled without any discretization along the *x*-direction. Therefore, the accuracy of the proposed technique for the analysis of such geometries involving wide vertical metallizations can be improved by modeling the metallizations as a set of the narrow ones, i.e. subdividing the vertical metallizations along the *x*- or *y*-directions.

3.4.3. Probe-fed Microstrip Patch Antennas

In this study, several examples on the analysis of probe-fed single layer patch antennas are carried out. Simulation results for the patches with various feed locations and parameters are compared with the experimental results which are available in [50]. For the experimental setup, the coax probes that feed the patches are referred as vertical pins. Hence, in the analysis of patches with MoM, vertical pins are modeled as thin vertical strips which are located parallel to the radiation direction. Note that, in the following cases to be analyzed, the feed locations were chosen to provide a resonant resistance that was close to 50 ohms. General geometry for the patches analyzed is shown in Fig. 3.17.

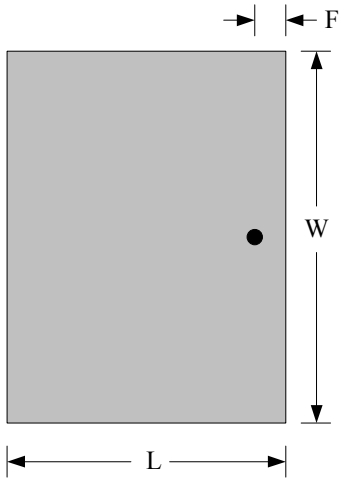

Figure 3.17: General geometry for the probe-fed patch antennas

In the first case, patch with the following parameters has been analyzed: W = 2.0 cm, L = 1.25 cm, F = 0.2 cm. The dielectric constant of the substrate is given to be 2.22 and the thickness is 0.079 cm. Vertical feed is modeled as a thin vertical strip with a width of 0.08 cm. The Smith chart plots of the impedance loci near resonance are shown in Fig. 3.18. The resonant frequency evaluated with the use of MoM is between 7.5-7.7 GHz, as it is observed from Fig. 3.18. According to experimental results, the resonant frequency is measured as 7.65 GHz. Thus, it can be stated that the resonant frequency predicted by the moment method solution is reasonably close to the measured value. However, the impedance locus of the moment solution is shifted a little with compared to the experimental result. This difference can be attributed to the effect of inductive shift which is primarily due to substrate thickness and consequent excitation of higher order modes [51,52].

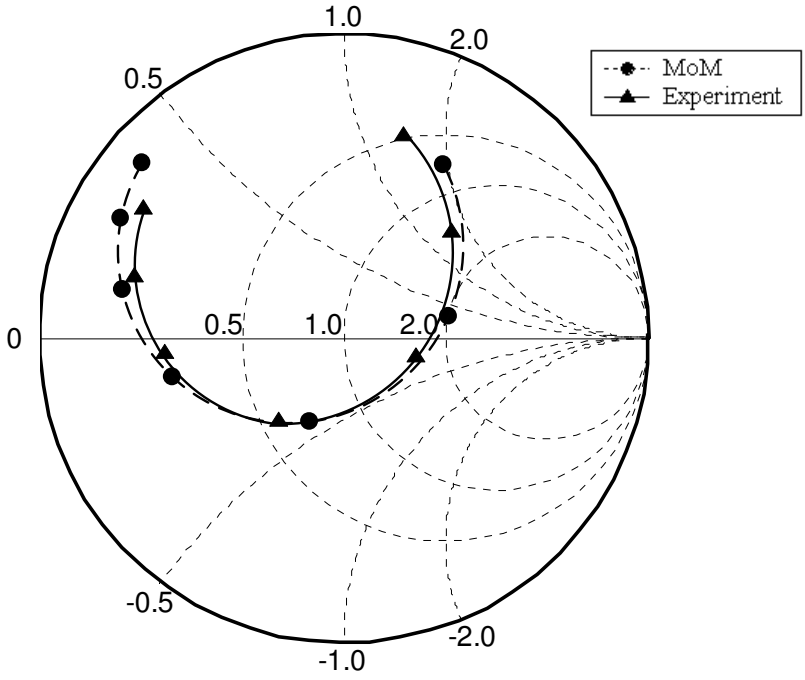

Figure 3.18: Input impedance of antenna for the first case. Frequency = 7.3-8.5 GHz Δf = 0.2

To show the substrate thickness effect on the amount of inductive shift, an experiment is performed with another patch antenna whose parameters are given as: W = 2.0 cm, L = 1.2 cm, F = 0.2 cm. The dielectric constant of the substrate is 2.22 and the thickness is 0.152 cm. Furthermore, to observe the result of modeling the vertical feed as a thin and a thick vertical strip, experiment is carried out with vertical strips having widths of 0.08 cm and 0.25 cm, respectively. The Smith chart plots of the impedance loci near resonance are shown in Fig. 3.19. As it is observed from the plot, for the experimental results and the moment method results with thin strip, the inductive shift was large enough so that the impedance loci did not cross the real axis, and so a resonant frequency could not be defined. In the case of analysis with thick vertical strip, the resonant frequency is obtained between 7.3-7.7 GHz.

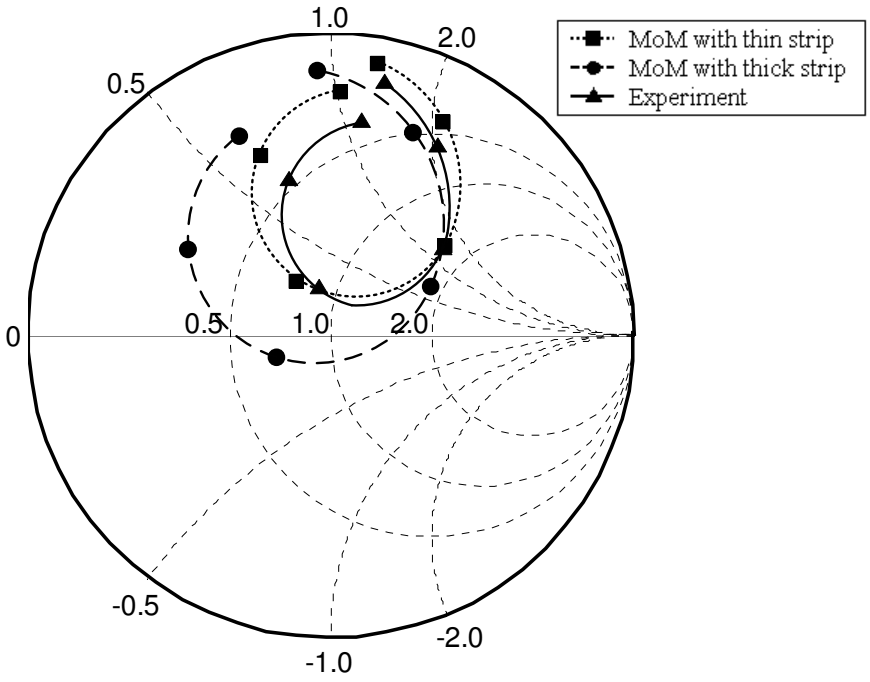

Figure 3.19: Input impedance of antenna for the second case. Frequency = 6.5-8.5 GHz
Δf = 0.4

It should be pointed out that while the measured behavior is well predicted by modeling vertical pin feed as a thin strip, results are less accurate by the use of a thick strip as a model. From this observation it can be concluded that, as the vertical strip which is used to model the vertical pin feed gets thinner, the accuracy of results improves.

Chapter 4

Multilayer Implementation

The spatial-domain MoM formulation in the solution of MPIE has been extensively used for the analysis of three-dimensional (3-D) objects in multilayered media [16,53]. In Chapter 3, we have proposed a technique based on the spatial-domain MoM in conjunction with the closed-form Green's functions in a single layer medium, and have tested for its accuracy. In this chapter, the spatial-domain MoM formulation for single layered planar geometries will be extended for multilayered geometries involving horizontal and vertical conductors. This extension includes the calculation of spatial-domain Green's functions for multilayered media. By using the DCIM, which is presented in Chapter 2, spatial-domain Green's functions can be represented in closed-form in terms of a couple of complex images. However, in the MPIE-MoM analysis of 3-D geometries in multilayered media, DCIM is not directly applied to the z and z' dependent spectral-domain Green's functions, since the evaluations of the MoM matrix entries corresponding to the vertical metallizations require the integration over z and/or z'. In the previous chapter, the way of eliminating this difficulty for a single layer medium has been discussed. Now it will be demonstrated for the analysis of multilayered geometries involving vertical conductors.

Once the closed-form spatial-domain Green's functions are obtained, multilayer implementation is followed by developing a consistent mathematical model for the basis functions at the junctions of the horizontal and vertical conductors, and along the vertical conductors traversing more than one layers. Once the basis functions are chosen to represent the current densities accurately, network parameters can be extracted with the use of the proposed technique in the previous chapter.

4.1 Difficulties and Solutions

The representative form of the spectral-domain Green's functions in a multilayer media is given in Chapter 2 and it is mentioned that to be able to sample the function over the range of approximation, z and z' dependence of the functions should be fixed. Since the horizontal conductors are placed on constant z-planes, fixing z and z' is not a problem for the Green's functions to be evaluated at these planes only. However, if the exponential approximation is directly applied to the Green's functions, since these variables exist explicitly in the formulation of spectral-domain Green's functions for the evaluation of the MoM matrix entries corresponding to the vertical metallizations, it does not exhibit an efficient technique.

For 3-D objects confined in one layer, this difficulty is eliminated by extracting the part depending upon z and z' in the spectral-domain Green's functions and integrating the function in spectral-domain over z and/or z', then applying the exponential approximation process. Now, the question is the applicability of this procedure for the Green's functions those are obtained for different source and observation layers.

As presented in Chapter 2, once the spectral-domain representation of Green's functions in the source layer is obtained in the forms of (2.69) and (2.84), field expressions for the observation layer above and below the source layer can be obtained iteratively starting from the source layer using (2.71) and (2.86), respectively. Since the z and z' dependence of the spectral-domain Green's functions in a multilayered media is always in exponential form, functions can be integrated analytically over z and/or z' for most basis functions. Therefore, the integration over z and z', which are due to the testing and convolution integrals along a vertical conductor, respectively, can be evaluated analytically in the spectral-domain, and then closed-form Green's functions corresponding to the result of this integrand can be obtained.

The spectral-domain Green's function $\tilde{G}_{zz}^{A}$ is used to demonstrate the extraction of z and z' dependent factors. Consider that the orientations of the source and observation layers are as shown in Fig. 4.1. Field expression for this orientation is obtained in Chapter 2 as follows:

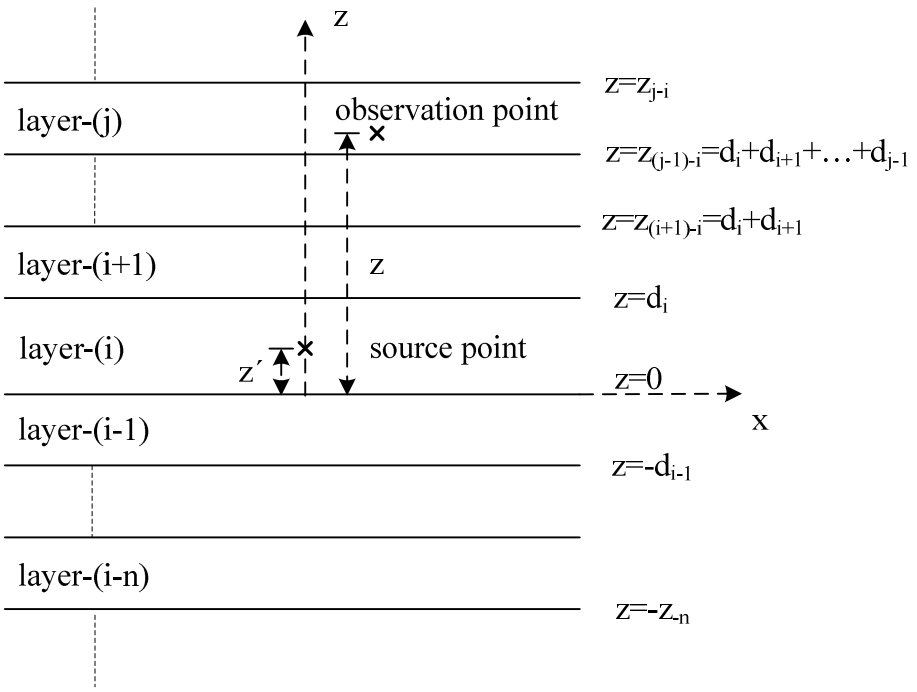

Figure 4.1: A general planar multilayer structure. Source layer = layer-(i); observation layer = layer-(j), where j > i

$$\tilde{G}_{zz}^{A} = \frac{\mu_j}{2jk_{zi}} A_j^{TM}\left[e^{-jk_{zj}(z-z')} + \tilde{R}_{j,j+1}^{TM} e^{jk_{zj}(z-z')} e^{-jk_{zj}2z_{j-i}}\right] \tag{4.1}$$

where A_j^{TM}, the amplitude of the up-going waves in layer-*j*, can be evaluated using (2.71) iteratively. Note that, z_{j-i} is the distance from the origin to the upper interface of the observation layer *j*. In order to obtain an explicit form of the above equation in terms of z and z', A_j^{TM} is rewritten here

$$A_j e^{-jk_{zj}(z_{(j-1)-i}-z')} = A_i^{+}\, e^{-jk_{zi}(d_i-z')}\underbrace{\left(\prod_{n=i}^{j-2}\boldsymbol{\Gamma}^{n,n+1} e^{-jk_{z(n+1)}d_{n+1}}\right)}_{=1 \text{ for } j-2<i}\boldsymbol{\Gamma}^{j-1,j} \tag{4.2}$$

where the term denoted by $\boldsymbol{\Gamma}^{j-1,j}$ describes the transmission from the top of layer-(j-1) to the bottom of layer-j. A_i^{+TM} has already been obtained in the source layer, layer-i, as

$$A_i^{+TM} = M_i^{TM}\left(1 + e^{-jk_{zi}2z'}\tilde{R}_{i,i-1}^{TM}\right) \tag{4.3}$$

Then, by substituting (4.3) into (4.2) the following expression is obtained:

$$A_j^{TM} = M_i^{TM}\left(1 + e^{-jk_{zj}2z'}\tilde{R}_{i,i-1}^{TM}\right)e^{-j(k_{zj}-k_{zi})z'}\underbrace{\left[\underbrace{\left(\prod_{n=i}^{j-2}\boldsymbol{\Gamma}^{n,n+1}e^{-jk_{z(n+1)}d_{n+1}}\right)}_{=1\ for\ j\text{-}2<i}\boldsymbol{\Gamma}^{j-1,j}e^{-j\left(k_{zj}d_i - k_{zj}z_{(j-1)-i}\right)}\right]}_{K(Const.)} \tag{4.4}$$

where K denotes the constant part of the above equation. Since all the terms are expressed explicitly in terms of z and z', the spectral-domain Green's function $\tilde{G}_{zz}^{A}$ in the observation layer, layer-j, can be written by substituting (4.4) into (4.1)

$$\begin{aligned}\tilde{G}_{zz}^{A} = \frac{\mu_j}{2jk_{zi}}\Big\{&M_i^{TM}Ke^{-j\left(k_{zj}z - k_{zi}z'\right)} + M_i^{TM}\tilde{R}_{j,j+1}^{TM}Ke^{-j\left(-k_{zj}z - k_{zi}z'\right)}e^{-jk_{zj}z_{j-i}} \\ &+ M_i^{TM}\tilde{R}_{i,i-1}^{TM}Ke^{-j\left(k_{zj}z + k_{zi}z'\right)} + M_i^{TM}\tilde{R}_{j,j+1}^{TM}\tilde{R}_{i,i-1}^{TM}Ke^{-j\left(-k_{zj}z + k_{zi}z'\right)}e^{-jk_{zj}z_{j-i}}\Big\}\end{aligned} \tag{4.5}$$

Hence, when the observation layer (j) is above the source layer (i), the spectral-domain Green's function $\tilde{G}_{zz}^{A}$ can be written as a summation of exponentials in which each exponential is in the form of $\exp[j(\pm k_{zj}z \pm k_{zi}z')]$, and the z and z' dependence only appears in these exponential factors. Furthermore, the similar procedure can be applied when the observation layer is located below the source layer.

4.2 Choices of Basis and Attachment Functions

As previously mentioned, the basis functions used to approximate the induced current density along the horizontal and vertical conductors of the geometry are chosen to be rooftop and half rooftop basis functions, respectively. Saw-tooth attachment functions are included to the vertical half rooftop basis functions to satisfy the current continuity at the intersections of vertical and horizontal conductors. In this thesis, the choice of basis and attachment functions

for the analysis of vertical metallizations is extended to facilitate the analysis of printed geometries in a multilayered media. Without loss of generality, basis functions used to represent the current density along the horizontal conductors are rooftop functions. However, vertical basis functions together with the associated attachment functions used at the junctions of metallizations have to be re-examined.

Attachment functions used at the junctions of horizontal conductor placed between two layers and the vertical conductors located at the top and bottom layers are chosen to be positive and negative slope saw-tooth functions respectively, as shown in Fig. 4.2a-b. It is also provided that the proposed model at the junctions satisfies the conservation of charges, and in turn the continuity of current density.

Finally, as a consequence of the verification of the current continuity at the layer interfaces, if two vertical conductors intersect at the layer interfaces, two half rooftop basis functions form a rooftop basis function, as it is observed from Fig. 4.2c. Note that, there is no attachment functions used for this case.

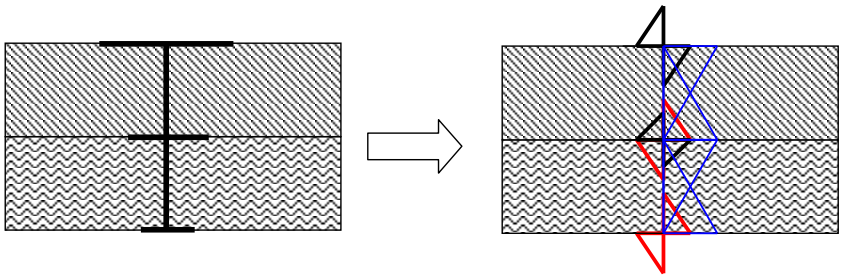

(a)

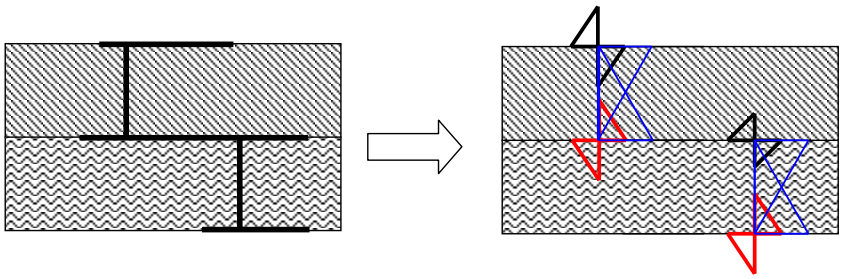

(b)

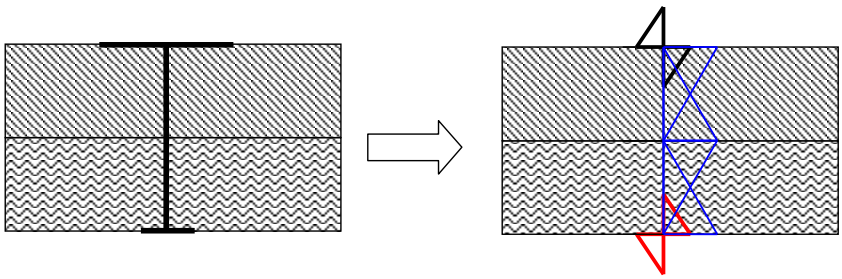

(c)

Figure 4.2: (a) Vertical conductor traversing horizontal conductor at the layer interface
(b) Vertical conductors terminate with a horizontal conductor
(c) Vertical conductor traversing two layers

4.3 Numerical Results and Discussions

The proposed technique for the analysis of three-dimensional (3-D) objects in multilayered media is demonstrated on several examples and the results are compared to those presented in the literature and obtained from commercial EM analysis software *em* by Sonnet.

4.3.1 Two-layered Microstrip Geometry with Vertical Conductors

In order to verify the technique presented in this thesis, MoM solution is applied to a multilayered 3-Port microstrip geometry having multiple vertical metallizations whose circuit parameters and layer information are shown in Fig. 4.3. Note that, throughout the explanations, horizontal metallizations planted between substrate-substrate interface and substrate-air interface are referred as bottom and top metallizations, respectively. Current distributions along the bottom and top metallizations when the Port-1 is excited with a unity current source, Port-2 is open-circuited and Port-3 is short-circuited, are calculated using the proposed method in this thesis and compared to those obtained from *em* by Sonnet, as shown

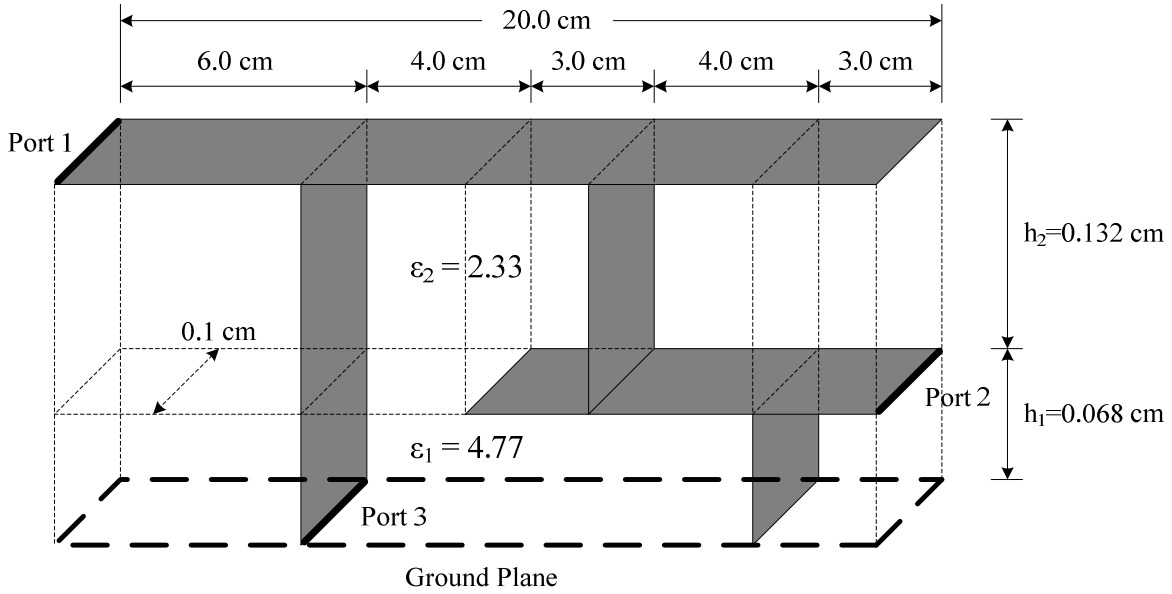

Figure 4.3: Multilayered microstrip geometry with multiple vertical metallizations

in Fig. 4.4 and 4.5, respectively. The operating frequency where the current distributions are obtained is 1 GHz. It should be noted that, there is no variation in the current density along the *y*-direction. An excellent agreement is observed, slight differences in the amplitude can be attributed to the inherent models of the approaches: *em* by Sonnet solves the problem in shielded environment while the method proposed here solves in open environment, which inevitable causes some differences on the resonant frequencies for the structures.

As a second validation, Port-3 is excited with a unity current source with all the other ports are open-circuited at an operating frequency of 1.2 GHz. The current distributions along the bottom and top metallizations are compared to those obtained from *em* by Sonnet, as shown in Fig. 4.6 and Fig. 4.7. The results of the proposed method and Sonnet are in good agreement except for the amplitudes. As previously discussed, the reason for the mismatch between the plots is the environment where the solution is obtained for the given geometry.

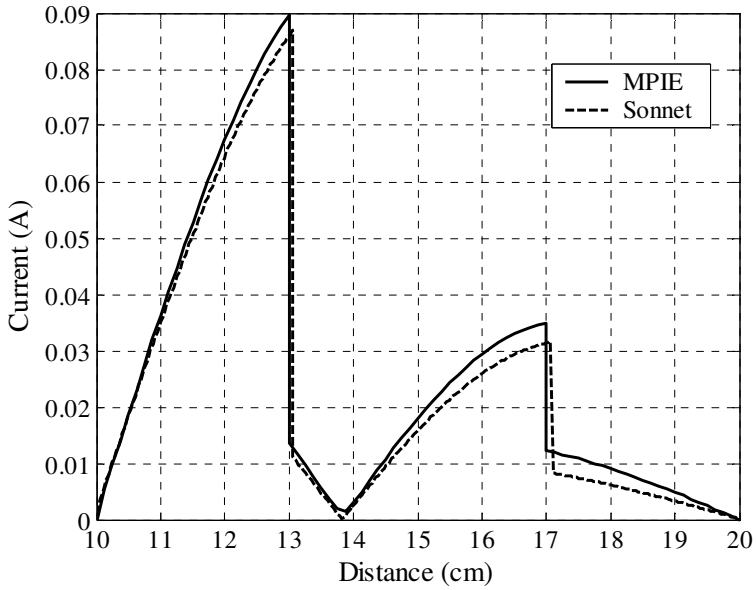

Figure 4.4: The current distributions obtained from the MPIE method described in this thesis and *em* by Sonnet on the bottom metallization when Port-1 is excited, Port-2 is open-circuited and Port-3 is short-circuited

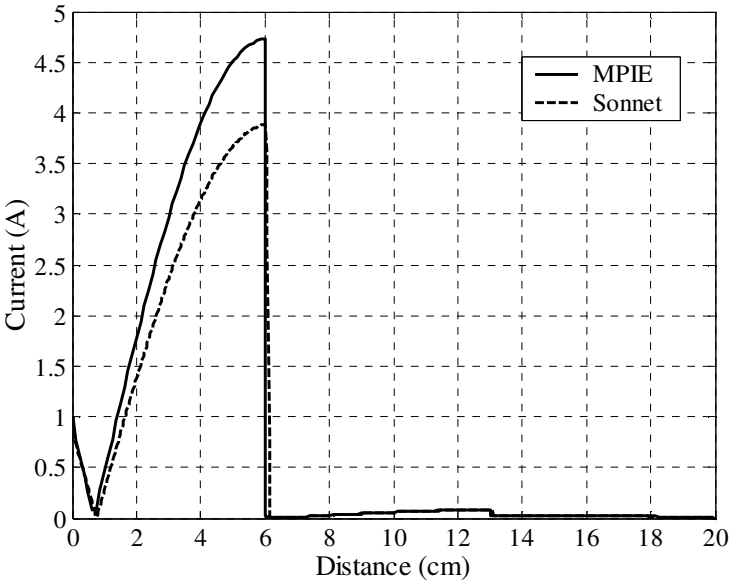

Figure 4.5: The current distributions obtained from the MPIE method described in this thesis and *em* by Sonnet on the top metallization when Port-1 is excited, Port-2 is open-circuited and Port-3 is short-circuited

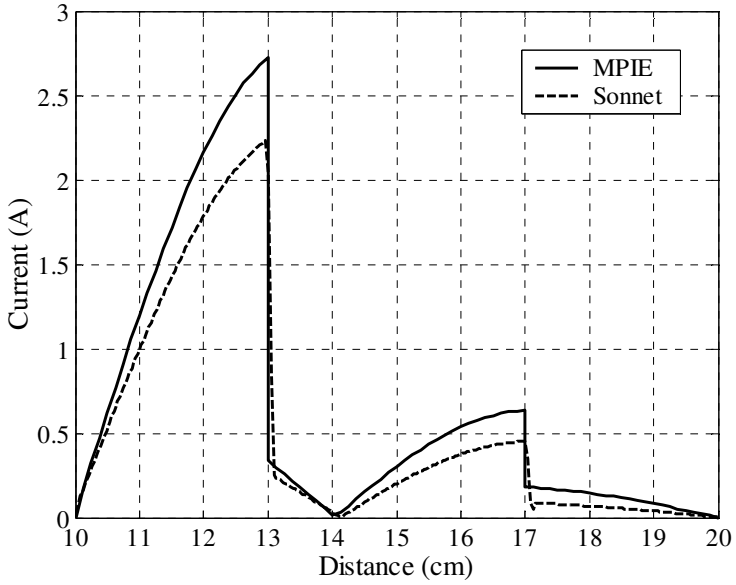

Figure 4.6: The current distributions obtained from the MPIE method described in this thesis and *em* by Sonnet on the bottom metallization when Port-3 is excited, and all the other ports are open-circuited

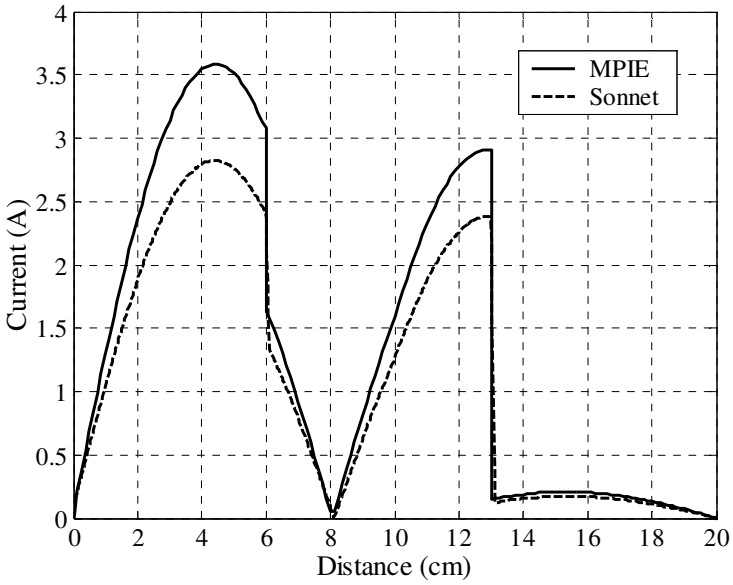

Figure 4.7: The current distributions obtained from the MPIE method described in this thesis and *em* by Sonnet on the top metallization when Port-3 is excited, and all the other ports are open-circuited

Locations of the vertical conductors inserted to geometry can be observed from the plots of current distributions where the horizontal current densities exhibit sudden falls (or rises). These are the junctions of horizontal and vertical conductors, and the continuity of the current is validated at these junctions by simply comparing the variation of the horizontal current density with the vertical current density. Thus, the proposed model at the junctions of conductors located in a multilayered media works properly.

Finally, real and imaginary parts of the scattering parameters, S_{33} and S_{13}, are evaluated with the proposed technique and results are compared to those obtained from *em* by Sonnet, as shown in Figs. 4.8-4.11. Slight differences between the plots can be attributed to the assumption made on the environment where the solution is obtained.

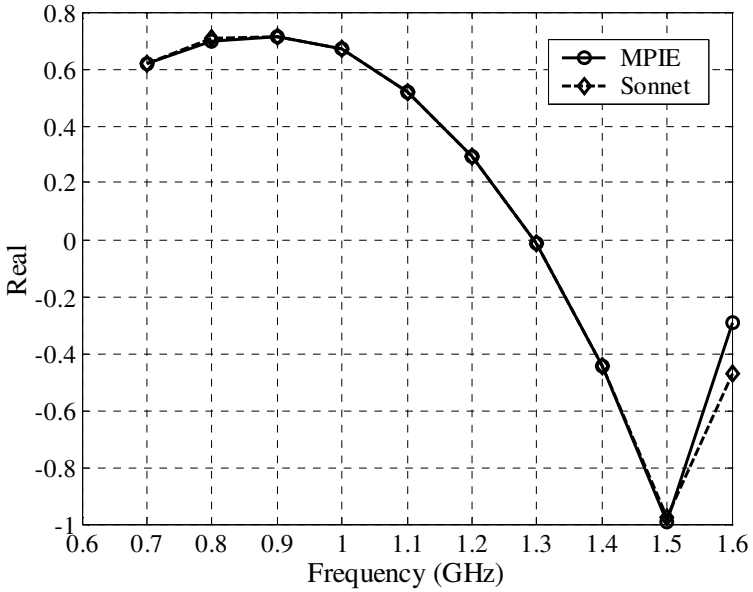

Figure 4.8: The real part of S_{33} for the microstrip geometry given in Fig. 4.3

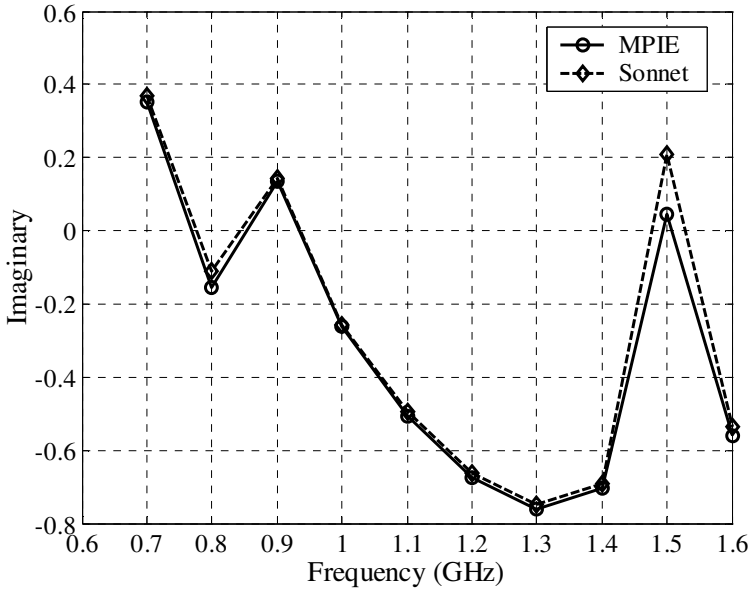

Figure 4.9: The imaginary part of S_{33} for the microstrip geometry given in Fig. 4.3

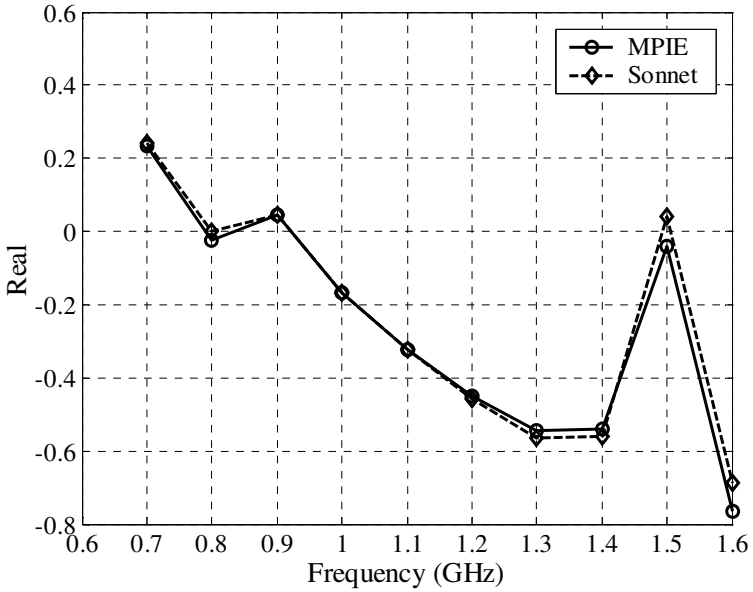

Figure 4.10: The real part of S_{13} for the microstrip geometry given in Fig. 4.3

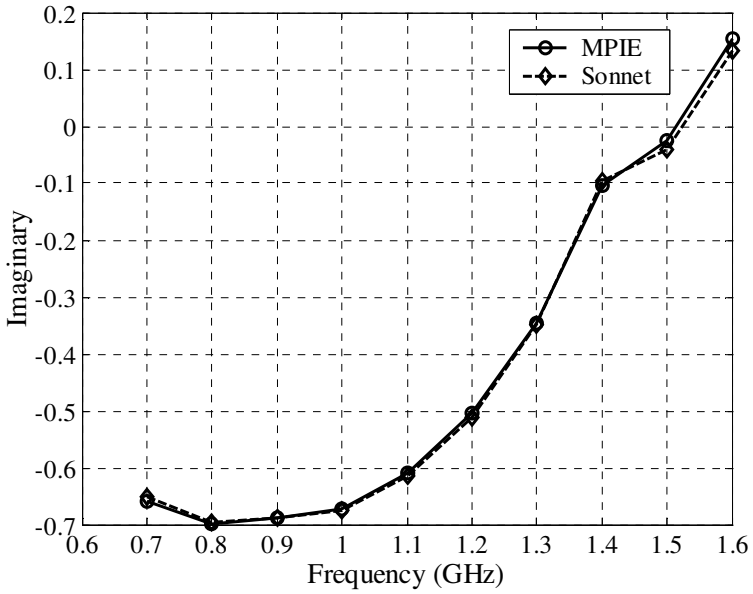

Figure 4.11: The imaginary part of S_{13} for the microstrip geometry given in Fig. 4.3

4.3.2 Microstrip Antenna on a Thick Substrate:

Microstrip geometry work in the previous example has employed electrically thin substrates. Thus, lengths of the vertical conductors were sufficiently short to represent current densities along them with two half-rooftop vertical basis functions. However, representation of the vertical current density in the analyses of microstrip geometries with significantly thick substrates may require additional basis functions. In this example, microstrip antenna with a length of 10.0 cm and width of 0.1 cm is planted over a thick substrate as shown in Fig. 4.12. The thickness and the relative permittivity of the substrate are 3.0 cm and 2.94, respectively. First, microstrip antenna is shorted at x = 3.4 cm and the geometry is analyzed by the excitation of the terminal with a unity impressed-current source. Note that, two basis functions denote the vertical current density in this analysis. To denote the vertical current density with three basis functions, single layer medium is divided into two sub regions with equal thickness and permittivity. The geometry is analyzed on this multilayered media at the frequency of operation of 1.5 GHz, and the current distribution along the horizontal conductor is compared to those obtained from the analysis in single layer medium, as it can be seen in Fig. 4.13. Furthermore, four basis functions are implemented for the vertical current density, but results are not improved significantly. Hence, three basis functions are sufficient to represent the current density along the vertical conductor.

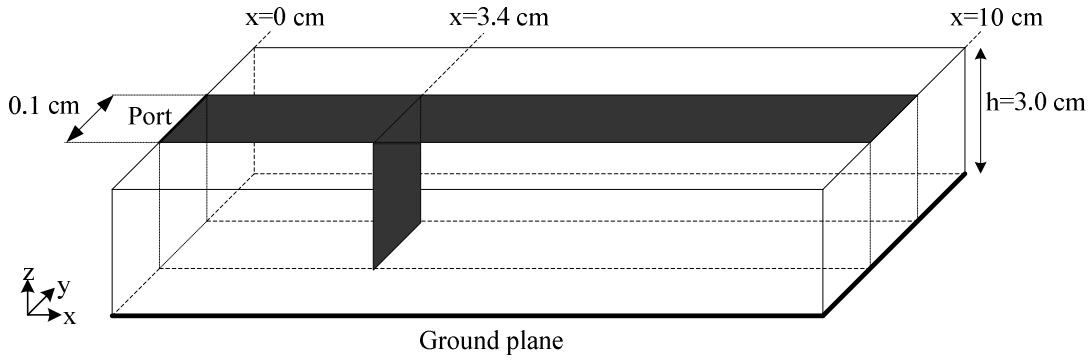

Figure 4.12: A microstrip line with a shorting strip over a thick substrate (ε_r = 2.94)

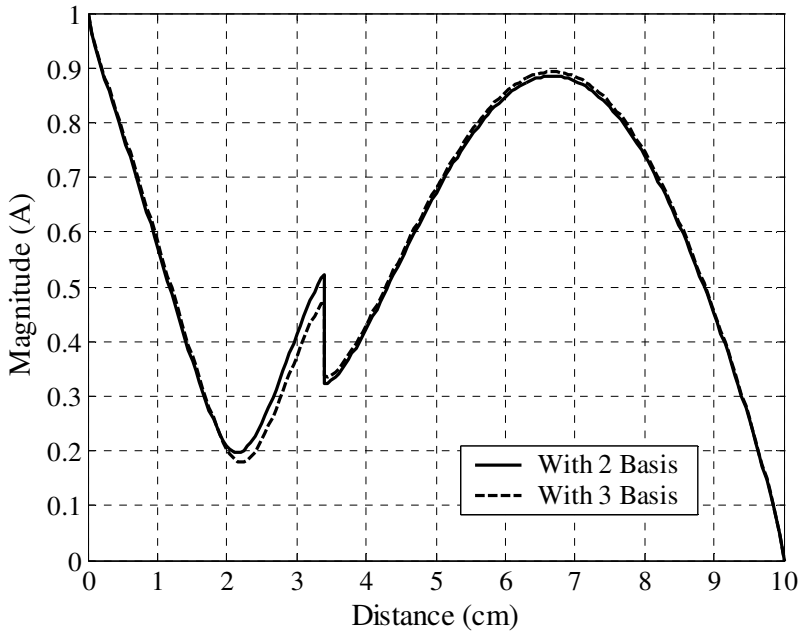

Figure 4.13: Current distribution along the microstrip line in Fig. 4.12 when the vertical current density is represented with two and three basis functions

4.3.3 Patch Antenna with Shorting Strips:

Another example demonstrating the validity of the MPIE-MoM analysis of 3-D planar structures is the patch antenna structure whose geometry and dimensions are given in Fig. 4.14b. Geometry is placed on top of a two-layered media whose parameters are given in Fig. 4.14a. In this example, the S-Parameter of the antenna is analyzed for different number of vertical shorting strips. Since the radiating structures are not accurately analyzed by *em* by Sonnet, simulation results could not be compared with the *em*. However, resonant frequencies obtained from the analysis for different number of vertical strips can be a measure for the verification of the algorithm's working procedure.

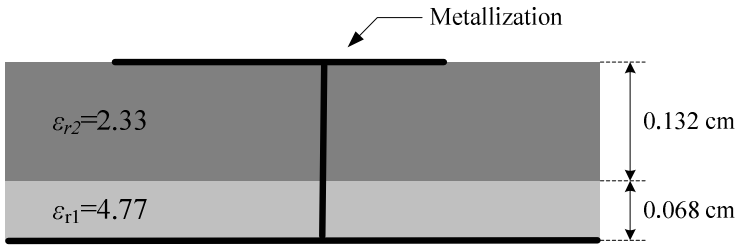

(a)

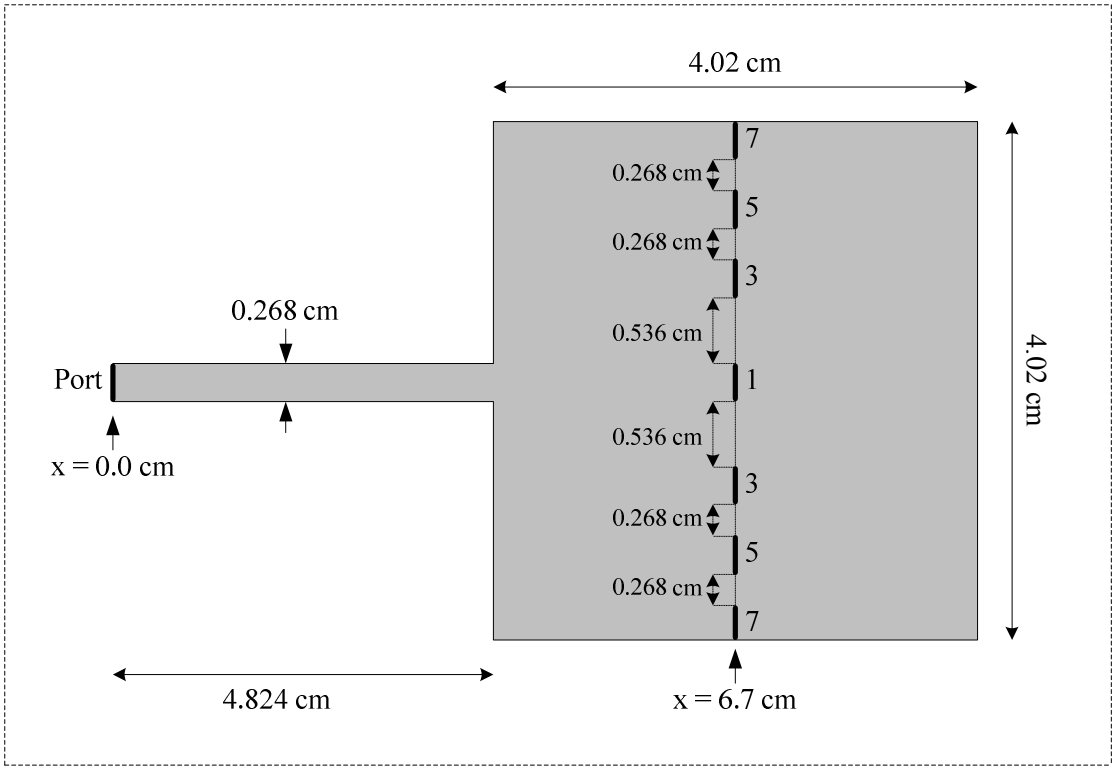

(b)

Figure 4.14: Patch antenna with shorting strips (a) Side view (b) Top view

For this example, seven different shorting strips are added on the horizontal conductor. All the vertical strips are chosen to be spanning in the *y*-direction with a width of 0.268 cm and all have the same *x*-coordinate which is x = 6.7 cm. At first, geometry is analyzed without including shorting strips and S-Parameters for this case is compared to those obtained from the analyses of geometry with one and three strips, as shown in Fig. 4.15.

S-Parameters corresponding to inclusion of seven shorting strips are also shown in Fig. 4.16. Resonant frequency for the patch when it is totally shorted at x = 6.7 cm is calculated $\left(f_s = c/4 \cdot 1.876 \cdot \sqrt{\varepsilon_{eff}}\right)$ using the formulation for the effective dielectric constant given in Appendix C as 2.53 GHz. Consequently, resonant frequencies are consistent with the included number of shorting strips. Since the inclusion of additional vertical strips shorts the circuit better, resonant frequencies get closer to the resonant frequency calculated for the completely shorted case.

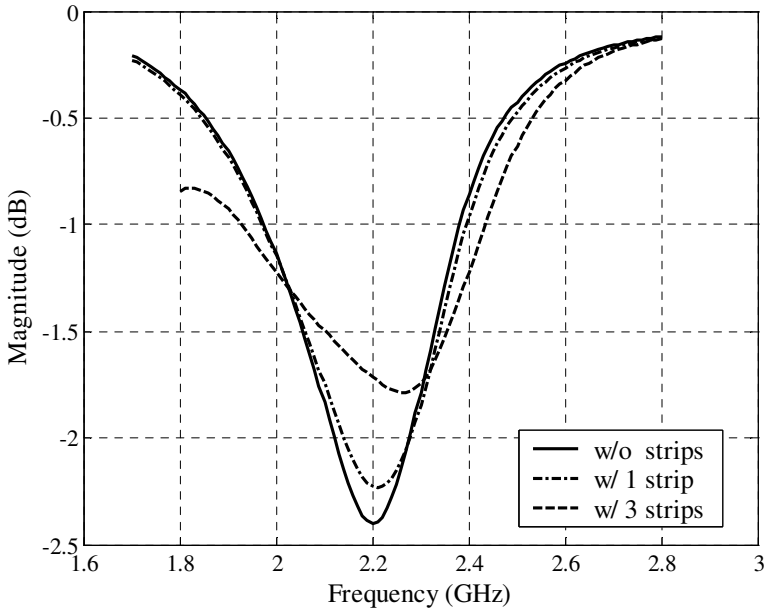

Figure 4.15: Magnitude of s_{11} for the patch in Fig. 4.14, with 0, 1 and 3 shorting strips

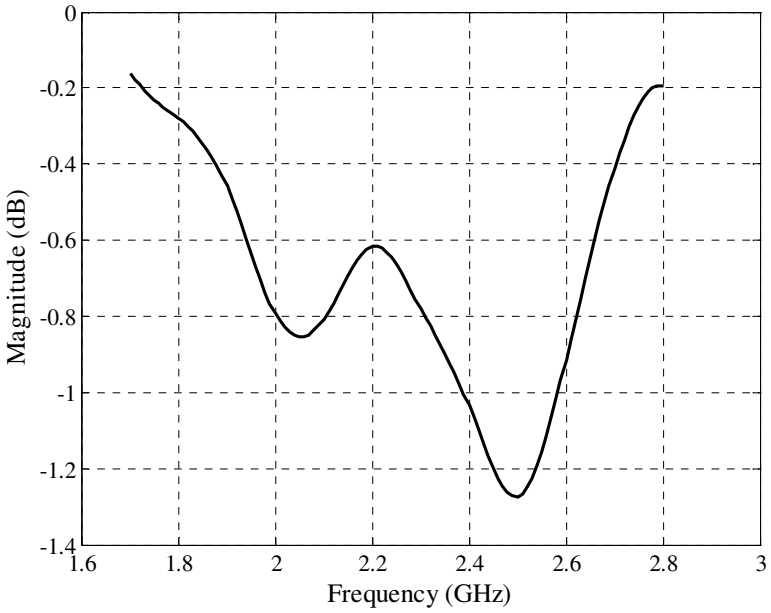

Figure 4.16: Magnitude of s_{11} for the patch in Fig. 4.14, with 7 shorting strips

4.3.4 Probe-Fed Two-Layered Patch Antenna:

To demonstrate the validity of the MoM formulation for multilayered planar geometries further, a two-layered patch antenna depicted in Fig. 4.17 has been analyzed and results are compared with the experimental results taken from [54]. In this antenna, the patch has two parts, each one at different layer interface and connected by a continuous vertical metallic wall which is modeled with multiple vertical strips.

The antenna is built using two different substrates whose parameters are given in Fig. 4.17. Input impedance of this probe-fed antenna between 1.9 and 2.3 GHz is evaluated using the proposed technique and compared with those obtained from [54], as shown in Fig. 4.18. Note here the agreement on the resonant frequencies of the proposed technique and the experimental result. However, the simulated curve is obtained as the shifted version of the experimental result. This could be due to the differences between the experimental setup and the simulation procedure for the analysis of antenna.

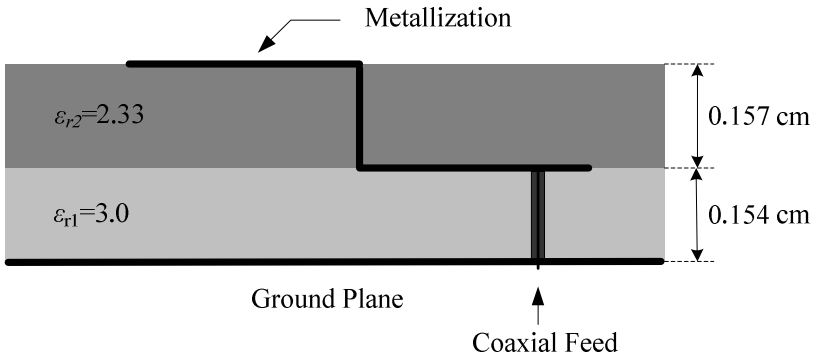

(a)

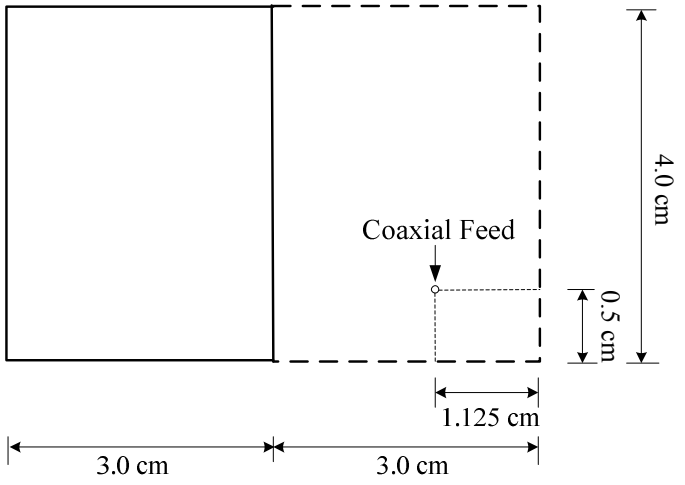

(b)

Figure 4.17: Two-layered patch antenna (a) Side view (b) Top view

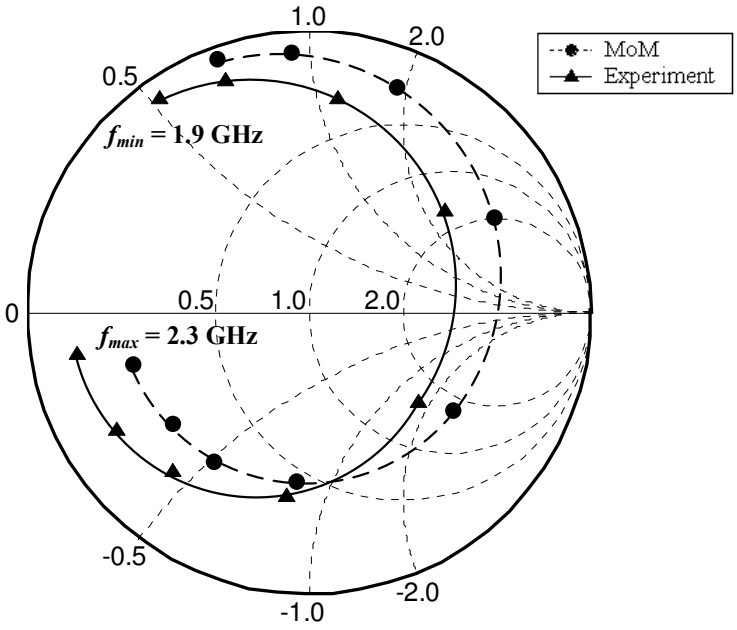

Figure 4.18: The input impedance of the two-layer microstrip patch antenna given in Fig. 4.17 (step = 0.05 GHz)

Chapter 5

Efficient Full-Wave Simulations of Multiple Vertical Conductors

In this chapter, the efficiency of the method, in the sense described in Introduction, will be discussed with the explicit definitions of the components of the method that contribute to the efficiency of the whole algorithm. In a numerical algorithm, it is inevitable to define the efficiency in terms of its computational time and the accuracy of the results. Assuming and guaranteeing that the accuracy of the algorithm used in this work is equivalent to the algorithms that the efficiency is compared, the computational time becomes the only factor in assessing the efficiency of the overall method. Of course, the accuracy of the method is not guaranteed by just words, but it is also demonstrated by comparing the results to those obtained from well-known full-wave EM simulators like *em* from SONNET. Once the criterion for the efficiency of the method is decided as the computation time, basically there are two main components that dominate the overall solution time for a geometry: Matrix fill time, which can be the dominating portion of the overall CPU time for small to moderate size geometries like those requiring several hundreds of unknowns; and, the matrix solution time that dominates for large geometries with thousands of unknowns. Therefore, any attempt to improve the efficiency of the technique should try to find better treatments for these components. Regarding the matrix fill time, the use of the closed-form Green's functions in the characterization of printed geometries with multiple vertical metallizations is formulated such that the matrix entries corresponding to the vertical strips are obtained in closed-forms. Not only these entries are cast in closed-forms, but also they include the parameter defining the location of the strip explicitly. Therefore, if the matrix entries for only one vertical

metallization are obtained, adding new vertical metallizations with the same length does not require any additional computational cost rather than evaluation of the already obtained entries at the location of the new vertical metallization(s). For the matrix solution time of the resulting matrix equation, the well-known, computationally expensive (O(n^3) operation), LU decomposition is used. Although nothing is added to LU decomposition algorithm to make it more efficient, the solution time is improved for additional vertical metallizations once the resulting matrix equation is solved for only one vertical metallization. This is because, since adding new vertical metallizations does not alter the horizontal geometry, the part of the matrix equation does not change, and therefore, the part of the original LU can be used repeatedly. This is especially important in the design process of microwave components, such as filters or antennas with prescribed characteristics, via an optimization algorithm. In this chapter, these algorithms are reviewed, and their contributions to the efficiency of the overall algorithm are assessed in terms of matrix fill and matrix solution times.

Since one of the main contributions of this work is the improvement of the matrix fill time when multiple vertical metallizations are involved, the discussion on this issue is given first in section 5.1 with theory and demonstration of the method. Then, it is followed by a brief discussion on the matrix solution time in Section 5.2. Finally, the efficiency of the method is supported via some representative examples in Section 5.3.

5.1 Discussions on MoM Matrix Fill Time

Since matrix fill time is generally the dominant part of the overall solution time for small to moderate size geometries, development of efficient matrix filling algorithms has been one of the major research topics in computational electromagnetics. In this context, the use of closed-form Green's functions together with the MoM for the solution of MPIE has significantly reduced the cost of full-wave analysis of planar geometries in layered media. However, in cases of vertical metallizations, the use of closed-form Green's functions was not as straightforward, and its advantages were not as obvious. There was no problem with

the derivation of Green's functions for a vertical electric dipole, but there were problems in incorporating them into the MoM formulation, originated from the implementation of the method that results in the closed-form Green's functions in the spatial domain. With the method proposed in [35], these difficulties have been alleviated, and as a result, the method has become an efficient method for multilayer planar geometries even with vertical metallizations. Although it was briefly mentioned in [35] that the method can be organized to handle multiple vertical metallizations very efficiently, it has not been demonstrated yet. In this chapter, the method proposed in [35] is extended to make the analysis of printed geometries with multiple vertical metallizations very efficient, with almost no additional coast to that of the analysis of the same geometry with one vertical metallization.

Prior to any discussion and comments on the effects of the technique on the matrix fill time, for the sake of coherence and completeness of this chapter, the main steps of the formulation are briefly given here as follows: i) the tangential components of the electric field, E_x, E_y and E_z, on the horizontal and vertical conductors are written in terms of current densities, J_x, J_y and J_z, with the use of the associated Green's functions; ii) the unknown current densities are expanded in terms of known basis functions with unknown coefficients; then, iii) the matrix equation for the unknown coefficients of the basis functions is obtained ([$\mathbf{Z}$] [$\mathbf{I}$] = [$\mathbf{V}$]) by applying the boundary conditions on the conductors via the testing procedure of the MoM. Note that the elements of matrix Z that correspond to horizontal conductors only are denoted by Z_{xx}, Z_{xy}, Z_{yx} and Z_{yy}, and, in cases of additional vertical conductors, Z_{xz}, Z_{zx}, Z_{yz}, Z_{zy} and Z_{zz} need to be incorporated, which are explicitly provided in [35]. It has been demonstrated in [35] that some difficulties exist for the evaluation of the terms corresponding to vertical conductors, and these difficulties are originated from the way the closed-form Green's functions are derived; namely, from the exponential approximation of the spectral-domain Green's functions, which requires fixing of z and z' for the sampling of the function. To put it another way, the exponential approximation, and in turn the resulting closed-form Green's function, is only valid for those fixed values of z and z'. Since

the horizontal conductors are always placed at constant z-planes and the MoM requires the evaluation of the Green's functions at these planes only, there is no problem for the matrix terms corresponding to horizontal conductors. But, the MoM matrix entries corresponding to vertical metallizations require the convolution and the inner-product integrals to be performed over z and/or z', which is the source of the problem. This problem has been circumvented by the method given in [35], and hence, the efficient calculation of the matrix entries has been achieved for geometries involving vertical metallizations too. The approach proposed and implemented in [35] has not only made it possible to use the closed-form Green's functions with vertical metallizations, but, in addition, it has facilitated the addition of multiple vertical metallizations with almost no computational cost, provided that all vertical strips employ the same number of basis functions with the same z and z' dependence. The working mechanism of this approach and its use with multiple vertical metallizations are the subject matters of this section. Therefore, the technique is explained in detail and demonstrated on an example where the inner-product integral is to be integrated over z-variable in the following subsections.

5.1.1 Formulation

Let us consider a general 3-D geometry, as depicted in Fig. 5.1, where there is a patch over two planar dielectric layers backed by a ground plane, and three vertical connections: two for shorting patch to the ground, one for connecting patch to a port on a different layer.

Since the subject matter of this chapter is an efficient handling of multiple vertical strips in a rigorous analysis of printed structures, matrix entries corresponding to the vertical metallizations, which involve z and/or z' integrals, require special attention. Instead of demonstrating the formulation for a general printed structure extending in three dimensions, for the sake of clarity and briefness, let us assume that the geometry supports only x- and z-components of the current density, with no loss of generality. For such circuits, there are mainly five different inner product terms involving z-directed basis and/or testing functions

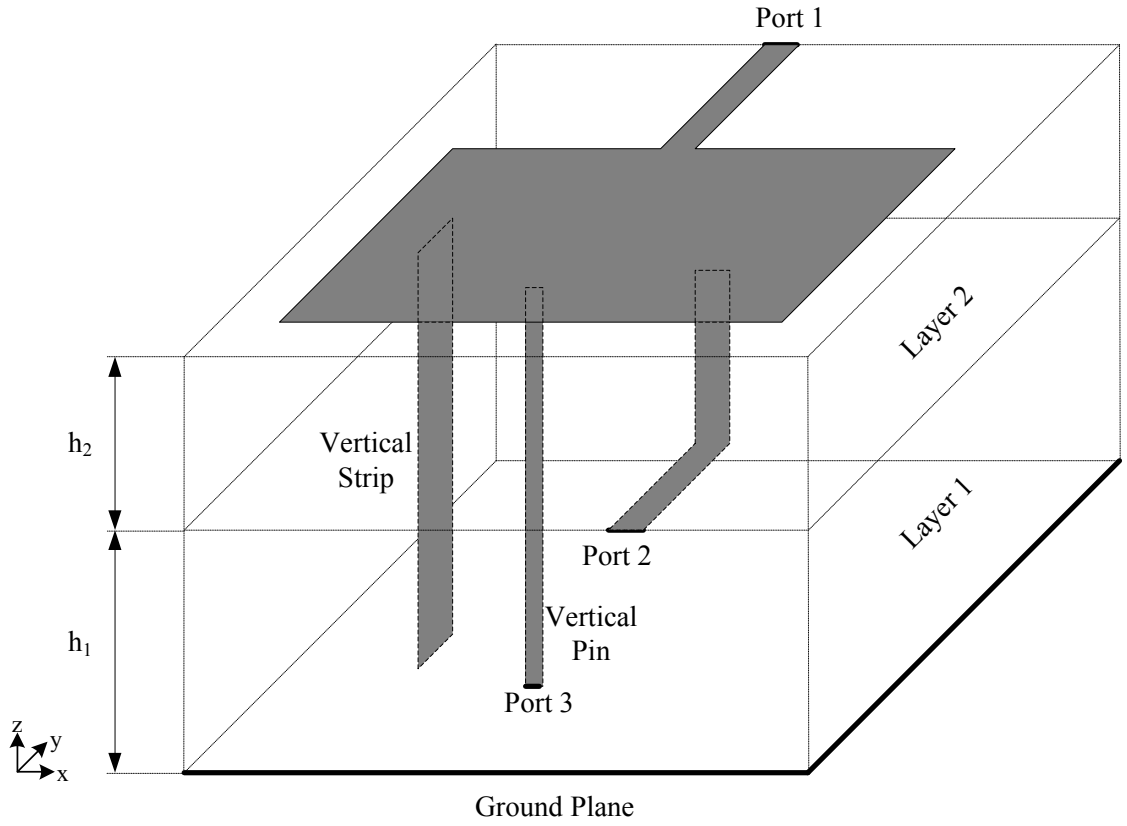

Figure 5.1: A general 3-D microstrip structure

.

among the MoM matrix entries, which are: $\left\langle T_{zi}, G_{zz}^{A} * B_{zj} \right\rangle$, $\left\langle \partial T_{zi}/\partial z, G_{z}^{q} * \partial B_{zj}/\partial z \right\rangle$ for Z_{zz}^{ij}; $\left\langle \partial T_{xi}/\partial x, G_{z}^{q} * \partial B_{zj}/\partial z \right\rangle$ for Z_{xz}^{ij}; $\left\langle T_{zi}, G_{zx}^{A} * B_{xj} \right\rangle$ and $\left\langle \partial T_{zi}/\partial z, G_{x}^{q} * \partial B_{xj}/\partial x \right\rangle$ for Z_{zx}^{ij}, where B_{xj}, B_{zj} and T_{xi}, T_{zi} denote the *j*-th basis and *i*-th testing functions used to expand the current density components in *x*- and *z*-directions, and G_{zx}^{A}, G_{zz}^{A}, G_{x}^{q} and G_{z}^{q} are the associated components of the Green's functions for vector and scalar potentials when the traditional form is used [22]. Since Green's functions – definitions, derivations in spectral domain for planar multilayer media, closed-form approximations in spatial domain – have been detailed in Chapter 2, they are not given here, except the ones required for the formulation. One of the

inner product terms given above, $\left\langle \partial T_{zm}/\partial z, G_z^q * \partial B_{zn}/\partial z \right\rangle$, which is one of the two contributing terms to Z_{zz}^{mn}, is used to demonstrate the formulation below, as it involves integrations over both z and z'. For the sake of completeness, the detailed formulations of other inner product terms are provided in Appendix B. Using the definitions of inner product and convolution integral, $\left\langle \partial T_{zm}/\partial z, G_z^q * \partial B_{zn}/\partial z \right\rangle$ can be written as

$$\left\langle \frac{\partial}{\partial z} T_{zm}(y,z), G_z^q * \frac{\partial}{\partial z} B_{zn}(y,z) \right\rangle = \iint dz dy \frac{\partial}{\partial z} T_{zm}(y,z) \cdot \iint dz' dy' G_z^q(x-x', y-y', z, z') \frac{\partial}{\partial z'} B_{zn}(y', z') \tag{5.1}$$

where x' and x denote the x-coordinates of the source and observation, respectively, both of which are constant at the vertical strip extending in y-direction for this inner product term. After some simple simulations, (5.1) can be cast into the following form

$$\left\langle \frac{\partial}{\partial z} T_{zm}(y,z), G_z^q * \frac{\partial}{\partial z} B_{zn}(y,z) \right\rangle = \int dy T_{zm}(y) \int dy' B_{zn}(y') \cdot \int dz \frac{\partial}{\partial z} T_{zm}(z) \int dz' G_z^q\left(|\boldsymbol{\rho} - \boldsymbol{\rho}'|, z, z'\right) \frac{\partial}{\partial z'} B_{zn}(z') \tag{5.2}$$

where the separability of the basis and testing functions is used, i.e., $B_{zn}(y, z) = B_{zn}(y)B_{zn}(z)$ and $T_{zm}(y, z) = B_{zm}(y)B_{zm}(z)$. At first, the spatial-domain Green's function in (5.2) is replaced by the spectral-domain Green's function by using the inverse Hankel transform relation as

$$F_z^q\left(|\boldsymbol{\rho} - \boldsymbol{\rho}'|\right) \overset{def}{=} \int dz dz' \frac{\partial}{\partial z} T_{zm}(z) \frac{1}{4\pi} \int_{SIP} dk_\rho k_\rho H_0^{(2)}\left(k_\rho |\boldsymbol{\rho} - \boldsymbol{\rho}'|\right) \tilde{G}_z^q\left(k_\rho; z, z'\right) \frac{\partial}{\partial z'} B_{zn}(z')$$
$$\cong \frac{1}{4\pi} \int_{SIP} dk_\rho k_\rho H_0^{(2)}\left(k_\rho |\boldsymbol{\rho} - \boldsymbol{\rho}'|\right) \cdot \iint dz dz' \frac{\partial}{\partial z} T_{zm}(z) \frac{\partial}{\partial z'} B_{zn}(z') \tilde{G}_z^q\left(k_\rho; z, z'\right) \tag{5.3}$$

where $\tilde{G}_z^q\left(k_\rho; z, z'\right)$ can be obtained analytically as an explicit function of z and z' in the source layer as

$$\tilde{G}_z^q = \frac{1}{2jk_{zi}\varepsilon_i} \left\{ e^{-jk_{zi}|z-z'|} - \tilde{R}_{TM}^{i,i+1} M_i^{TM} e^{-jk_{zi}(2d_i - z - z')} - e^{-jk_{zi}(z+z')} \tilde{R}_{TM}^{i,i-1} M_i^{TM} + \tilde{R}_{TM}^{i,i+1} \tilde{R}_{TM}^{i,i-1} M_i^{TM} e^{-jk_{zi}(2d_i - z + z')} + \tilde{R}_{TM}^{i,i-1} \tilde{R}_{TM}^{i,i+1} M_i^{TM} e^{-jk_{zi}(2d_i + z - z')} \right\} \tag{5.4}$$

and the generalized coefficients $\tilde{R}_{TM}^{i,i\pm1}$ and other terms like M_i^{TM} can be found in Chapter 2. Note that $\tilde{G}_z^q(k_\rho; z, z')$ and the other Green's functions can be written as explicit functions of z and z' not only in the source layer but in any layer, which is demonstrated in Chapter 4. After analytically evaluating z and z' integrals in (5.3), the auxiliary function F_z^q can be obtained in closed-form by the GPOF method as a function of $|\boldsymbol{\rho}-\boldsymbol{\rho}'|$. Hence, the inner product term (5.2) reduces to

$$\left\langle \frac{\partial T_{zm}}{\partial z}, G_z^q * \frac{\partial B_{zn}}{\partial z} \right\rangle = \int dy T_{zm}(y) \int dy' F_z^q\left(|\boldsymbol{\rho}-\boldsymbol{\rho}'|\right) B_{zn}(y') \tag{5.5}$$

and making the substitutions $x - x' = u$ and $y - y' = v$, the following expression is obtained

$$\left\langle \frac{\partial T_{zm}}{\partial z}, G_z^q * \frac{\partial B_{zn}}{\partial z} \right\rangle = \int dv F_z^q(u,v) \int dy' T_{zm}(y'+v) B_{zn}(y') \tag{5.6}$$

where the inner integral can be easily evaluated analytically, and the resulting outer integral of v can also be evaluated following [30]. It should be pointed out that, for this specific example, the auxiliary function $F_z^q(u,v)$ is an analytic function of independent variables u and v explicitly, although $u = x - x'$ is fixed at the distance between the vertical conductors (for a single y-spanning vertical strip, $u = x - x'$ is zero, because the x-coordinates of observation and source points are the same). In obtaining the auxiliary function F_z^q in (5.3), the GPOF method is applied to the function obtained analytically from the inner double integral of (5.3). This integral - the term that the GPOF is applied - can always be evaluated analytically because z and z' dependencies of spectral-domain Green's functions are always in exponential forms, and therefore, their products with most of the basis and testing functions used in EM simulations, and with their derivatives, are analytically integrable over z and z'. Consequently, the integrations over z and z' can be evaluated analytically once the spatial-domain Green's functions in the inner-product expressions are written in terms of their inverse transforms of their spectral-domain representations. Then, using the GPOF method (exponential approximation procedure) for the resulting spectral-domain function in

conjunction with the Sommerfeld identity, the auxiliary function $F_z^q(u,v)$ is obtained in closed-form, as a function of u and v. Once the auxiliary function $F_z^q(u,v)$ is obtained as such, it can be used for other vertical conductors by just evaluating it for different u and v values, provided that basis functions employed along the new vertical strips are the same as those used on the first strip. Therefore, adding new vertical strips would only require the evaluation of (5.6), which is done analytically and is the least time-consuming step of the inner-product calculations. Considering that all integrals in an inner-product term can be evaluated analytically (or semi-analytically), except using the GPOF method for the inverse Hankel transform in the evaluation of auxiliary functions, the GPOF method becomes the significant contributor to the matrix fill time.

Note that the basis and testing functions representing the current densities on the vertical strips may have different spans laterally, i.e., some may span in x-direction and others in y-direction, as shown in Fig. 5.2. Although the approach detailed above is quite general for any set of lengths of vertical conductors, the efficiency of the method for multiple vertical conductors can only be achieved when z and z' dependencies of the basis and testing functions for all vertical conductors are similar. To clarify this issue, i.e. why the efficiency is achieved for identical z and z' dependent basis and testing functions, one should refer to the analytic calculation of (5.3). In this equation, the GPOF method is applied to the integral of the product of the spectral domain Green's function and z- and z'-derivatives of the testing and basis functions. If one decides to use an additional vertical strip with more basis functions (as opposed to two used throughout this study and depicted in Fig. 5.2), then, these basis functions and corresponding testing functions would have different z dependencies, and would be integrated over different domains, resulting in different functions in (5.3) to be approximated by the GPOF method. Therefore, for every basis function with a different z domain dependency, the GPOF method needs to be implemented separately for all inner-product terms involving this basis and corresponding testing functions. The same argument also applies to the other matrix entries involving z directed basis and/or testing functions,

and, as a result, the matrix fill time increases in proportion to the number of basis functions with different z-domain representations, or, in other words, in proportion to the number of applications of the GPOF method.

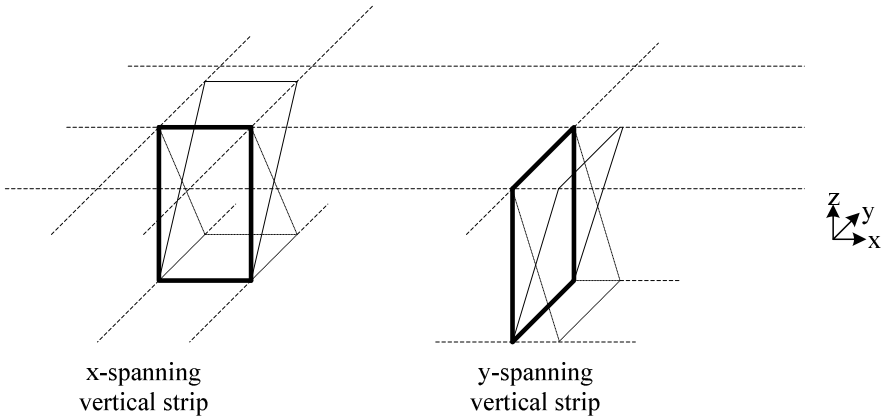

Figure 5.2: Basis functions on x-spanning and y-spanning vertical strips

Before closing the discussion on the implementation of the proposed approach, a possible question on how to implement it efficiently in cases of multiple vertical strips with different lateral spanning need to be clarified. Remember that basis and testing functions used in this work are separable functions, and can be written in terms of two independent functions; $B_{xn}(x, y) = B_{xn}(x)B_{xn}(y)$, $B_{yn}(x, y) = B_{yn}(x)B_{yn}(y)$, $B_{zn}(y, z) = B_{zn}(y)B_{zn}(z)$ and $B_{zn}(x, z) = B_{xn}(x)B_{xn}(z)$. Hence, using vertical strips with different spans does not pose a problem provided that their z dependencies are the same. Once the z dependencies are chosen to be identical, auxiliary functions can be evaluated, via the GPOF method, only once for every different z domain representation of the basis or testing functions. As the auxiliary functions are obtained in closed-form after the exponential approximation, they can be used repeatedly in the evaluations of the matrix entries corresponding to testing and/or basis functions with the same z and/or z' dependencies as those used originally in the evaluation of the corresponding auxiliary functions. For the sake of demonstration of the discussion presented here, let us consider the inner product term (5.1) whose evaluation has been detailed above.

Since only the z-dependencies of the testing and basis functions are involved in the evaluation of the auxiliary function (5.3), it does not matter if the strip spans on x- or y-directions. Therefore, for any additional vertical strip (regardless its direction of span) with different location on xy-plane but with the same z and z' representation, the same auxiliary function is to be used with different integration limits over x, y, u and v.

5.1.2 Demonstration

Once the formulation is set up, it would be nice and instructive to see how it is working on a simple and yet intuitive example, like a microstrip line with multiple shorting strips, Fig. 5.3. The widths of the microstrip line and vertical strips are chosen to be narrow, as compared to

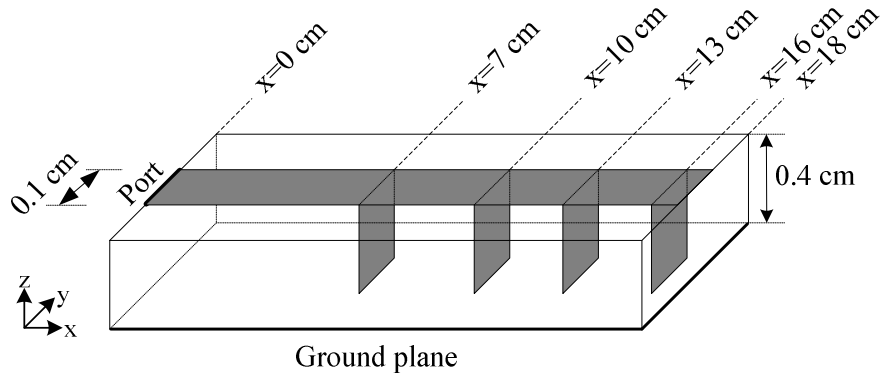

Figure 5.3: A microstrip line with multiple shorting strips over a substrate ($\varepsilon_r = 4.0$)

wavelength at the frequency of operation of f = 2.0 GHz, to facilitate the use of only longitudinal current density $J_x(x, y)$ on the microstrip line, for the sake of simplicity. So it would be enough to use rooftop basis functions, constant in y-direction and triangular in x-direction, to approximate the longitudinal current density along the line. Since the thicknesses of substrates used in microwave circuits and printed antennas are usually small as compared to wavelength, two basis functions would be sufficient to represent the current density $J_z(y, z)$ on each vertical strip. Using the same number of basis functions on every

vertical strip guarantees that the basis functions on each strip will have identical z-variations, which is the main requirement for the efficiency of the method as discussed above.

At first, to validate the proposed method, the current distribution along the microstrip line and S-Parameters with the real and imaginary parts are obtained and compared to that obtained from a commercial software, *em* by Sonnet, in Figs. 5.4-5.6. It is observed that the current distributions and scattering parameters are quite close to each other. The slight differences between the two results can be attributed to the difference between the environments that numerical techniques assume: "*em*" solves the geometry in shielded environment while the method proposed in this paper solves it in an open environment.

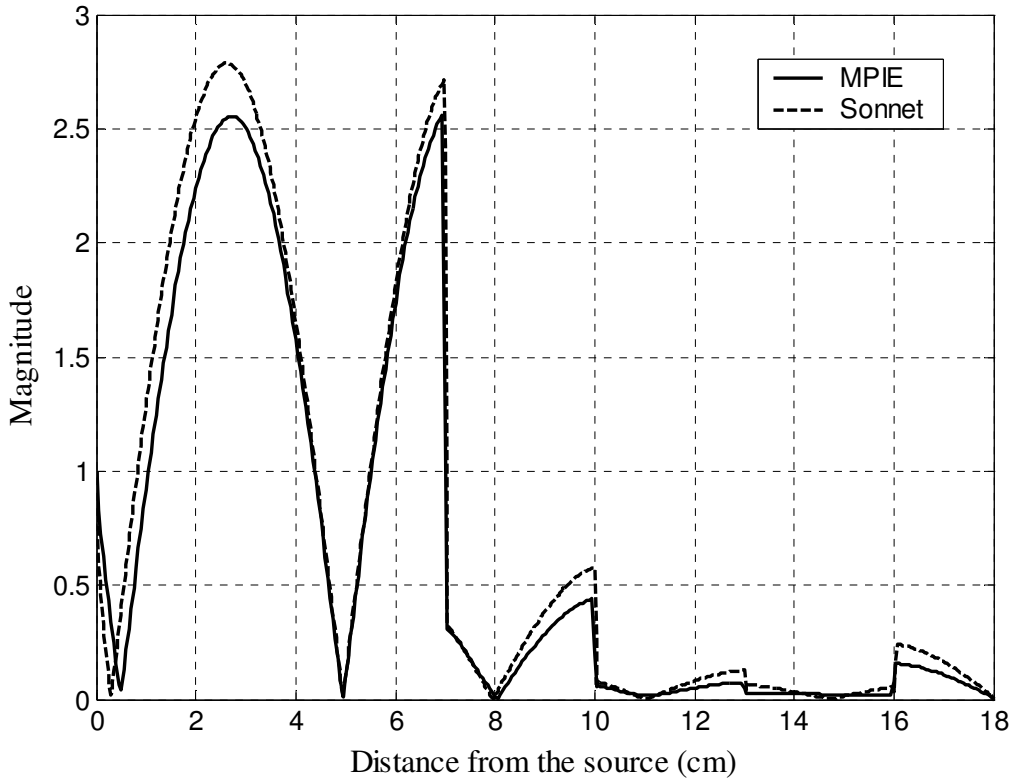

Figure 5.4: Current distributions along the microstrip-line circuits shown in Fig. 5.3

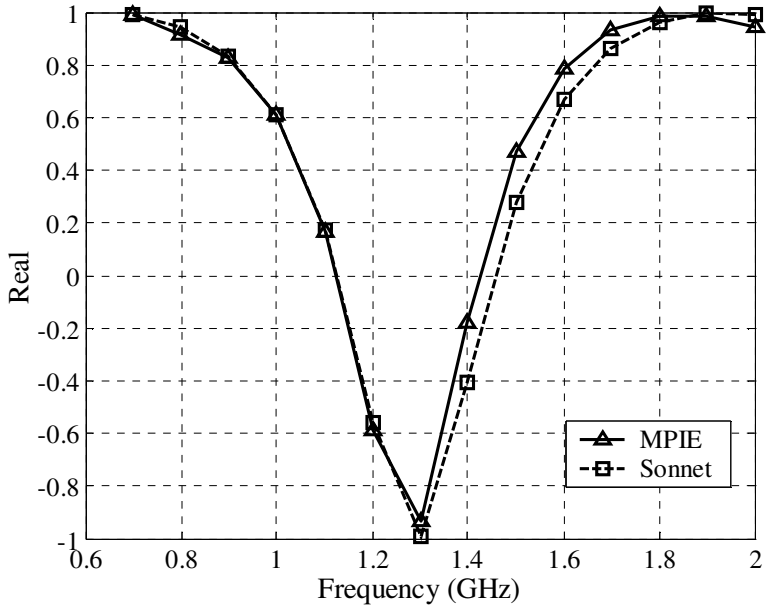

Figure 5.5: The real parts of S_{11} for the microstrip-line circuits shown in Fig. 5.3

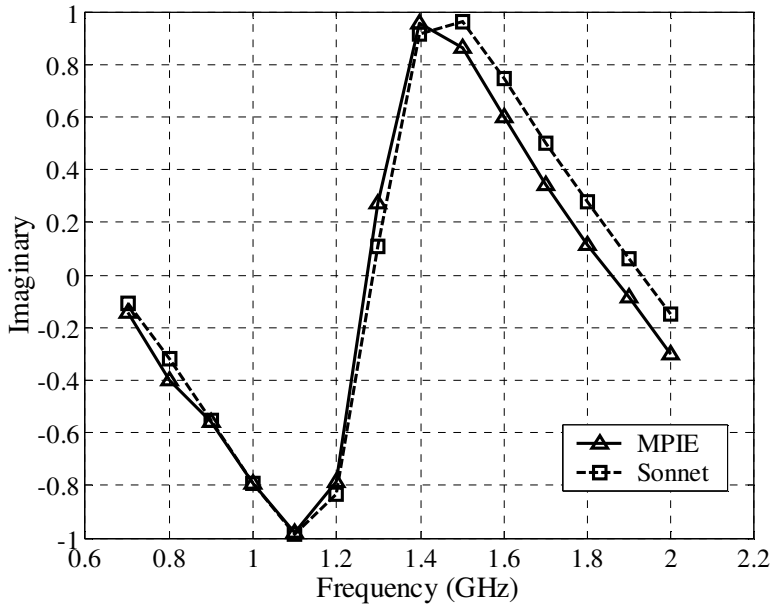

Figure 5.6: The imaginary parts of S_{11} for the microstrip-line circuits shown in Fig. 5.3

One more validation check may be the distance between the two minima of the current distribution, which is supposed to be equal to an half-wavelength and is about 4.55 cm. Using this information in the formula $\lambda = c/\sqrt{\varepsilon_{eff}}\, f$ results in an effective dielectric constant of 2.72, which is almost equal to the static effective dielectric constant of 2.71 obtained from the following well-known expression:

$$\varepsilon_{eff} = \frac{\varepsilon_r + 1}{2} + \frac{\varepsilon_r - 1}{2} \frac{1}{\sqrt{1 + 12h/w}} \tag{5.7}$$

where h and w are the thickness of the substrate and the width of the microstrip line, respectively, as given in Fig. 5.3.

Once the method is validated, the efficiency of the method for each additional vertical strip is assessed by studying the filling time of the MoM matrix entries corresponding to each added vertical strip, and provided in Table 5.1. In this study, the MoM matrix entries corresponding to horizontal part of the geometry are first filled, and then, the fill time of MoM matrix entries' corresponding to each additional vertical strip is recorded, for two different scenarios; the discretization on the horizontal plane is kept or varied with the addition of new vertical strips. In the former scenario, the necessary auxiliary functions need to be calculated only ones and used repeatedly, but for the latter, the auxiliary functions are calculated for every inner product term corresponding to each basis and testing functions introduced with the addition of new vertical strip. It is clearly observed from Table 5.1 that once one vertical strip is introduced into the formulation and MoM matrix is filled, adding new vertical strips requires almost no additional computational cost. To understand this, let us investigate the additional matrix entries and their constituents. The number of additional rows and columns for the MoM matrix, when a vertical strip is added, is equal to the number of basis functions on the strip. Since it was already mentioned that two basis functions on each vertical strip are employed, two rows and columns are to be filled in and included in the MoM matrix. However, if the Galerkin's method of Moments is used, only the columns or rows would be sufficient, due to the symmetry of MoM matrix.

Table 5.1: Matrix fill times for each additional vertical strip for the geometry in Fig. 5.3 by using 1.5 GHz Centrino CPU

Number of vertical strips	**MoM matrix fill-time for additional entries**	
	Fixed Discretization (sec)	**Variable Discretization (sec)**
1	20.8	20.2
2	1.1	20.4
3	1.3	20.6
4	1.7	21.0

For these new entries, there are five inner product terms to be evaluated for each distinct basis and testing functions, which are

$$\left\langle T_z, G_{zz}^A * B_z \right\rangle \text{ and } \left\langle \partial T_z/\partial z, G_z^q * \partial B_z/\partial z \right\rangle \text{ for } Z_{zz}$$

$$\left\langle \partial T_x/\partial x, G_z^q * \partial B_z/\partial z \right\rangle \text{ for } Z_{xz}$$

$$\left\langle T_z, G_{zx}^A * B_x \right\rangle \text{ and } \left\langle \partial T_z/\partial z, G_x^q * \partial B_x/\partial x \right\rangle \text{ for } Z_{zx}$$

Since they involve integration and/or differentiation on z and/or z' variables, the closed-form auxiliary functions are used instead of closed-form Green's functions in the evaluations of these inner-product terms. As the GPOF method is the main numerical block of the computation of the auxiliary functions, as demonstrated in (5.3), the number of GPOF implementation per vertical strip can be used as a measure of efficiency. To facilitate counting of the number of GPOF implementation, it should be noted that evaluation of each auxiliary function requires the calling of GPOF method three times, as three-level algorithm is used for the auxiliary functions and two-level algorithm for the Green's functions. Therefore, adding n-th vertical strip to already available (n-1) vertical strips requires the following counts of auxiliary function evaluations:

$$\underbrace{(3\times 2)}_{Z_{zz}^{(n,n)}} + (n-1)\underbrace{(3\times 2)}_{Z_{zz}^{(m,n)}} + \underbrace{(N\times 2)}_{Z_{xz}^{(n)}} \tag{5.8}$$

for Galerkin's MoM,

$$(2n-1)(4\times 2) + 3(N\times 2) \tag{5.9}$$

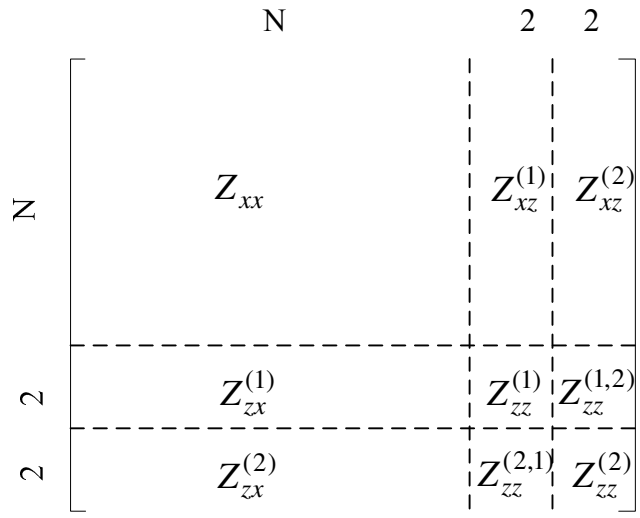

Figure 5.7: MoM matrix entries for Fig. 5.3 with two vertical strips

for MoM, where N is the number of basis function for the horizontal part of the geometry, as the partitions of the MoM matrix and their dimensions are shown in Fig. 5.7. Note that, in the derivations of these counts, two basis functions are assumed to be employed to represent the current density along each vertical strip, and the attachment basis functions are not included. To get an idea how the above counts are obtained for Galerkin's MoM, here are some numbers and their origins: for the 1-st vertical strip, the number of auxiliary function evaluations is (3x2)+(Nx2), where (3x2) corresponds to 3 different elements in $Z_{zz}^{(1)}$ with 2 inner-product terms in each, and (Nx2) is for the number of entries in $Z_{xz}^{(1)}$ with one inner-product term; for the second vertical strip, (3x2)+(3x2)+(Nx2) gives the additional number of auxiliary function evaluations, where the second term is due to the different entries in $Z_{zz}^{(1,2)}$.

Note that these counts have been obtained with the following assumptions: i) the matrix is symmetric as Galerkin's MoM is used; ii) attachment basis functions are not accounted for, which would further increase the number of auxiliary function evaluations; iii) auxiliary functions are re-calculated for each different term, as if MoM matrix is being filled using a

standard MoM approach. As the above formula and numbers provide the number of auxiliary function evaluation for the n-th additional vertical strip, the total number of evaluation for M additional vertical strips, in the case of Galerkin's MoM, can be easily calculated from (5.8) as $M(N\text{x}2)+3M(M+1)$. So, to get an idea on the order of auxiliary function evaluation, the following example represents the case provided in Fig. 5.3: 360 basis functions are used to approximate the current density over the horizontal conductor, N=360, and one vertical strip has already been added; adding 3 more vertical strips requires 2196 auxiliary function evaluations and 6588 (3x2196) GPOF implementations. However, with the use of the proposed method in Section 5.1.1, and considering that the additional vertical strips have the same length and the same number of basis functions as the first vertical strip, i.e., have identical z and z' dependent basis and testing functions, the auxiliary functions evaluated for the first vertical strip can be used repeatedly, with no need for additional evaluation of the auxiliary functions or implementations of the GPOF method. The only work left is to evaluate the auxiliary functions obtained for the first vertical strip at different ρ values, and perform x- and/or y-integrations analytically. Therefore, for vertical conductors expanded by 2 basis functions, (3x2)+2 auxiliary function evaluations will be sufficient for any number of vertical conductors. Note that (3x2) is for 3 different elements in $Z_{zz}^{(1)}$ with two inner-product terms each, and 2 is for two different basis functions with different z and z' variations out of (Nx2) elements of $Z_{xz}^{(1)}$ with one inner-product term. As a conclusion, in terms of exponential approximation via GPOF method, inclusion of any number of vertical conductors does not increase the computational complexity of the technique provided that the z and z' dependences of the basis and testing functions are chosen to be identical.

5.2 Discussion on Matrix Solution Time

In the previous section, it has been demonstrated that addition of multiple vertical strips with identical z dependence does not require the implementation of the GPOF method more than once for each distinct basis and/or testing functions along z-direction. As a result, a

substantial improvement in the matrix fill time of the spatial-domain MoM is achieved for multiple vertical conductors. However, as it is well known, the matrix fill time is only a dominating factor for small to moderate size geometries, and is not the only factor that affects the computational efficiency of an analysis method. The matrix solution time, which used to be a dominating factor for large geometries with thousands of unknowns, has become a dominating factor even for smaller geometries with substantially less unknowns with the advent of efficient fill-in algorithms. Therefore, the matrix solution algorithms need some mention for the specific problems of adding more vertical strips with a view of optimization the performance of printed circuits.

Once the MoM matrices are filled, the solution of the matrix equations can be obtained by using the computationally expensive LU decomposition, with $O(n^3)$ computational complexity. If the optimization of the geometry is also considered in addition to the analysis, then the use of LU decomposition at every iteration during the optimization will dominate the overall solution time. But as it is well known, the major part of the geometry, and in turn, the most entries of the MoM matrix, does not change with iteration for typical optimization problems. Instead, at each step, new parts are added to or deleted from a main body, which constitutes the larger part of the whole geometry and corresponds to addition or deletion of a few new rows and columns. Using this fact, the LU decomposition of the original geometry can be used repeatedly for each iteration of the optimization process. As an example, assume that the circuit performance will be optimized by inclusion or deletion of vertical strips into a horizontal printed structure, for which the locations and the number of vertical strips are the optimization parameters. Since there is no modification on the horizontal part of the geometry during the optimization, the corresponding matrix entries will not change. Therefore, LU decomposition of the part of the matrix corresponding to the unmodified part during the optimization can be used repeatedly, after each iteration, to find the LU decomposition of the whole matrix. This can be achieved by using the Order Recursive Gaussian Elimination (ORGE) method [55], which was developed to improve the

computational efficiency of solving the matrix equations for modified geometries. Since optimization is not studied in this thesis, the use of ORGE method is not employed. But since the optimization is the next step after developing an efficient method for the solution of 3-D general planar geometries, the ORGE method should be used in conjunction with an optimization algorithm in the future work.

5.3 Numerical Examples

So far, an electromagnetic based simulation algorithm was introduced together with its demonstration on a simple example with thorough discussions on its efficiency when multiple vertical strips were involved. In this section, the proposed algorithm is applied to more practical printed circuits, and its results, like S-parameters and current distributions, are compared to those obtained from a well-known commercially available full-wave EM simulator, *em* by SONNET, and to available experimental results in the literature.

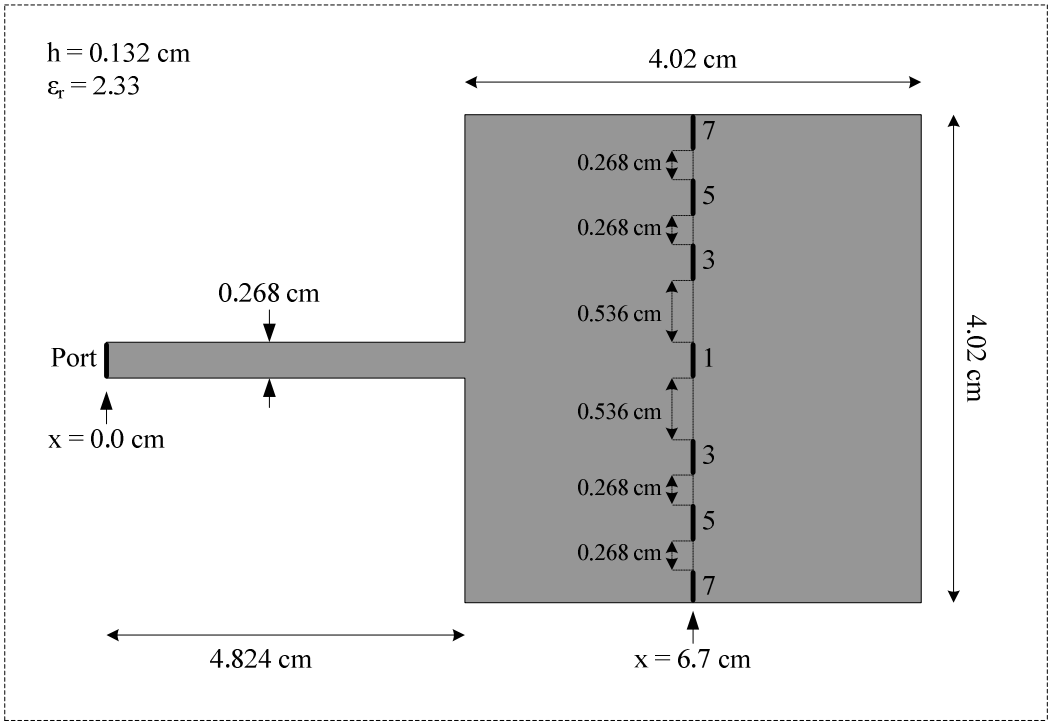

Figure 5.8: Geometry of a patch antenna using multiple vertical conductors

To start with, let us consider a patch antenna whose geometry and dimensions are given in Fig. 5.8, where the thickness h and dielectric constant ε_r of the substrate are set to 0.132 cm and 2.33, respectively. Note that, vertical strips employed in this study are chosen to be spanning in y-direction with the same width of 0.268 cm, and all are located at x = 6.7 cm to approximate short-circuiting the patch at a distance of 1.876 cm from its left edge. All vertical strips have the same length (equals to the thickness of the substrate) as they are short-circuiting the patch to ground, and therefore, the basis and testing functions have the same z and z' dependences, enabling the algorithm to efficiently analyze the effects of multiple vertical strips. The choice of a patch antenna with vertical strips, as an example, is motivated by the facts that: i) vertical strips are used to achieve multi-function antennas, like dual-band, dual-polarized antennas; and ii) the results expected and achieved could be interpreted intuitively, as the patch would be expected to have resonances (according to the cavity model) at the frequencies of 2.48 GHz ($=c/(2\times 4.02\times\sqrt{\varepsilon_{eff}}$) and 2.65 GHz ($=c/(4\times 1.876\times\sqrt{\varepsilon_{eff}}$) with no shorting strip, and with full short-circuiting at a distance of 1.876 cm from the feeding edge, respectively where ε_{eff} is calculated heuristically using the formulations in Appendix C. As the first step, the implementation of the algorithm requires meshing the horizontal and vertical conductors in the geometry: the square patch is meshed into 15×15 cells, employing 420 (=2×15×14) basis functions for the current densities on the patch, J_x and J_y together; 18 basis functions for the feeding line; and 2 basis functions for each vertical strip. Once the algorithm is applied to the geometry depicted in Fig. 5.8, with the necessary information as provided above, s_{11} is obtained from the immediate result of the algorithm, the current density, as described in Chapter 3, over a band of frequency. To observe the effect of the shorting strips, the geometry is first analyzed with 0, 1 and 3 vertical strips, and then, strips with number 5, and number 7 are added consecutively, where the numbers appear just next to the strips in Fig. 5.8. The magnitudes of s_{11} are provided in Figs. 5.9 and 5.10, respectively, and the resonant frequencies of the patch with no vertical strip and

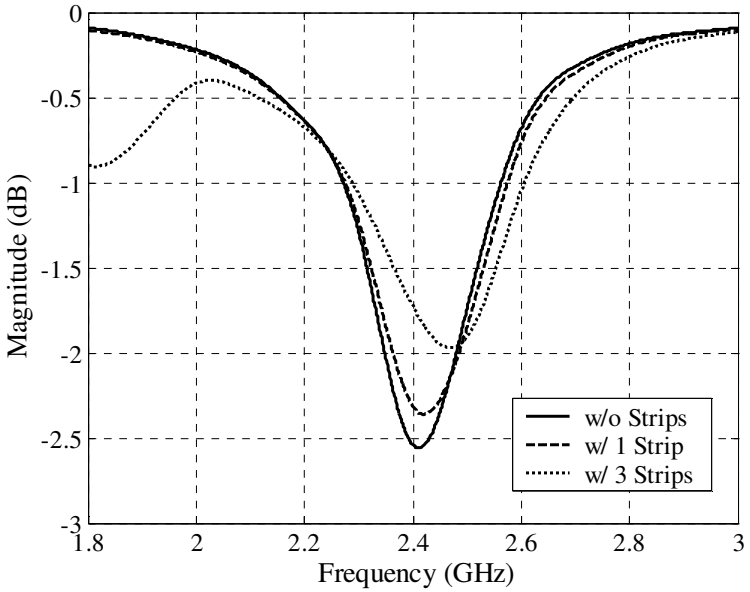

Figure 5.9: Magnitude of s_{11} for the patch in Fig. 5.8, with 0, 1 and 3 shorting strips

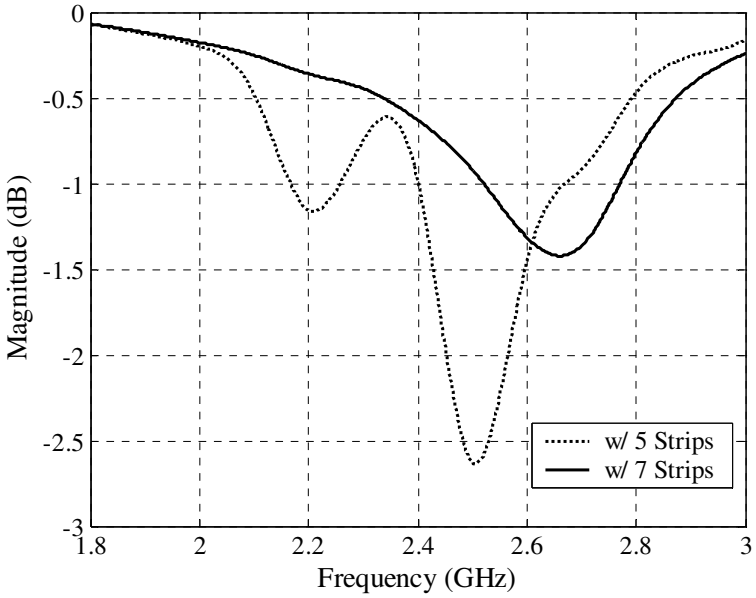

Figure 5.10: Magnitudes of s_{11} for the patch in Fig. 5.8, with 5 and 7 shorting strips

with 7 vertical strips are observed to be about 2.42 GHz, and 2.65 GHz, which are in good agreement with the above predicted resonant frequencies.

Since the main objective of this section is to demonstrate the efficiency of the method, rather than characterization of different structures, the matrix-fill time for the entries corresponding to each additional vertical strip is studied and provided in Table 5.2. Note that adding the first vertical strip requires almost half a minute, while adding six more vertical strips uses up to 12 seconds total, to fill up the corresponding entries in the MoM matrix when no symmetry argument of the geometry is used to further reduce the time.

Table 5.2: Matrix-fill times for each additional vertical strip for the geometry in Fig. 5.8

Number of vertical strips	**MoM matrix fill-time for additional entries**	
	Fixed Discretization (sec)	**Variable Discretization (sec)**
1	35.4	35.4
2	1.0	37.2
3	1.3	37.4
4	1.6	38.3
5	2.0	39.9
6	2.4	40.6
7	3.1	41.5

In Chapter 4, the same patch geometry with multiple vertical conductors has been analyzed in a multilayer environment. Verification of the technique presented in this thesis has been provided for this geometry in example 4.3.3. Now, the method used in this thesis is compared in terms of efficiency with the results obtained from the analysis of multilayered patch geometry whose layer information is given in Fig. 5.11.

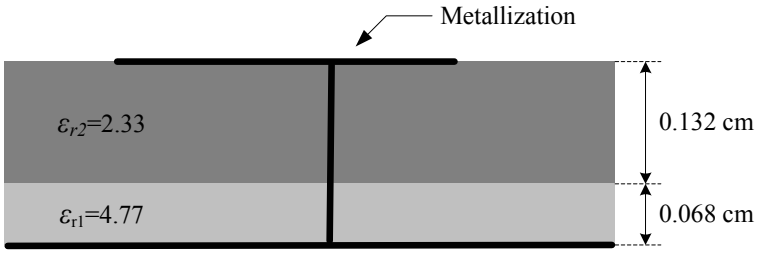

Figure 5.11: Side view of the multilayered patch antenna with shorting strips

The surface of the patch antenna is discretized in such a way that the total number of horizontal basis functions used on the patch surface is 438. Since it was already demonstrated in Chapter 4, for the analysis of this patch geometry with multiple vertical strips, three basis functions on each vertical strip are employed to represent the current flow in the vertical direction. In fact, two half-rooftop basis functions at the substrate-substrate intersection are treated as a rooftop function. However, in the evaluation of auxiliary functions, integrations are performed with the half-rooftop basis functions. Hence, Table 5.3 shows the time it takes and the number of GPOF employed for the evaluation of the Green's or auxiliary functions (for four half-rooftop basis functions in this case) for the given multilayered geometry whose top and side views are given in Figs. 5.8 and 5.11 respectively. Furthermore, the efficiency of the method for each additional vertical strip for a fixed discretization is provided in Table 5.4. This example gives a significant insight for the effects of using additional basis functions along vertical conductors are demonstrated.

Table 5.3: Computation times for the evaluation of Green's functions for the geometry of the multilayered patch antenna whose side view is shown in Fig. 5.11. Frequency of operation is 1.0 GHz and results are obtained by using 1.5 GHz Centrino CPU

Green's or Auxiliary Functions involving	**Time (sec) (for ε_{r1} =4.77, ε_{r2} =2.33)**	**Number of GPOF employed**
No z or z' integrations	2.3	16
Only z or z' integrations	8.4	36
Both z and z' integrations	14.2	96

Table 5.4: Matrix fill times for each additional vertical strip for the multilayered patch geometry whose top and side views are given in Fig. 5.8 and Fig. 5.11

Number of vertical strips	**MoM matrix fill-time for additional entries**
	Fixed Discretization (sec)
1	116.0
2	2.9
3	3.9
4	5.3
5	6.9
6	8.8
7	10.2

As a final example, we have implemented the PIFA antenna in a single layer medium which was studied in [38]. In this case, the patch has been set to lie on top of the layers, and has been short-circuited along its left edge to the ground plane as shown in Fig. 5.12a. The dimensions of the patch and the location of the feed (modeled as a thin strip) are given in Fig. 5.12b. In [38], geometry is shorted with a wide vertical plate along its left edge. As mentioned in the first example, to extract the circuit parameters, implementation of the delta-gap excitation model with assuming the shorted edge as a terminal may end with erroneous results. Therefore, the wide shorting plate is discretized and modeled as a set of 15 narrow vertical strips.

Input impedance of this probe-fed patch antenna between 2.6 and 2.95 GHz is evaluated using the proposed technique and compared with those obtained from [38], as shown in Fig. 5.13. The simulation results obtained with MoM formulation agree well with the measurements. It can be concluded that the qualitative behavior is well predicted with the use of MoM in conjunction with the closed-form Green's functions. Note here the systematic small shift in frequency. This shift can be attributed to the dissimilarities between the conditions on experimental and simulation setup.

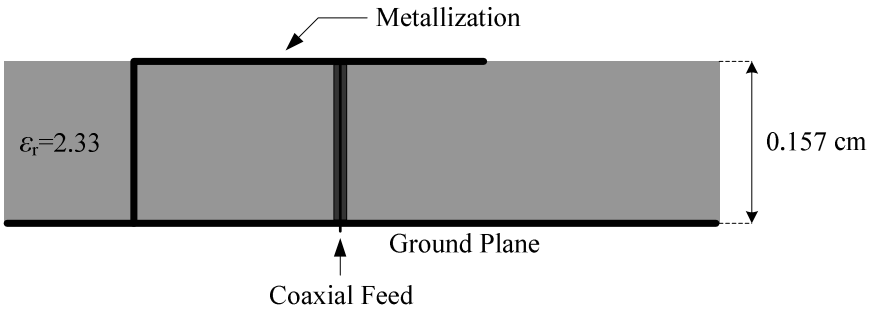

(a)

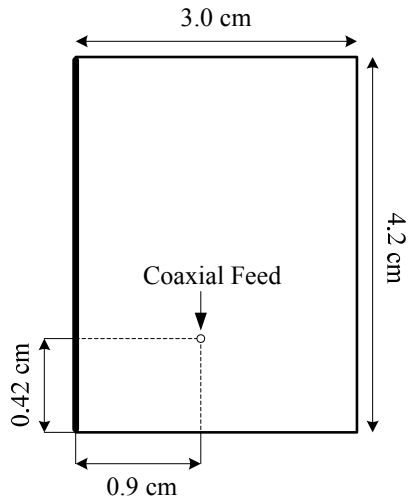

(b)

Figure 5.12: Single layered patch antenna (a) Side view (b) Top view

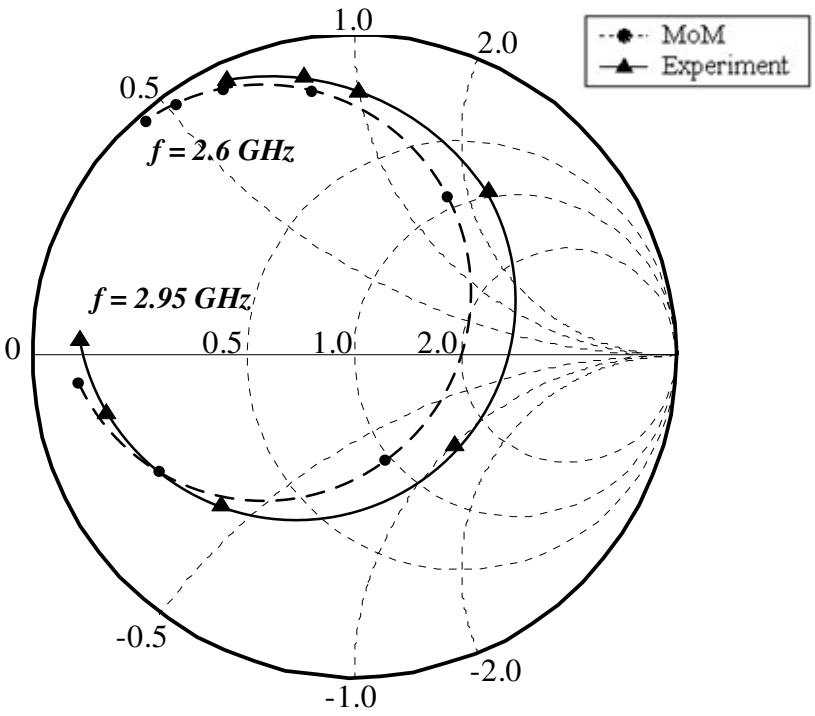

Figure 5.13: The input impedance of the short-circuited microstrip patch antenna between 2.6 and 2.95 GHz(step = 0.05 GHz)

As the ultimate measure for the efficient handling of multiple vertical metallization, in addition to the first one, increase in the matrix fill time for additional vertical strips are listed in Table 5.5. It is observed that adding new vertical strips to the existing ones has almost no effect on the computational complexity of the whole method. This can be stated with adding 15 strips to the microstrip line with one vertical strip costs about 37.0 seconds. Therefore, for a fixed discretization, once the matrix entries are obtained corresponding to addition of one vertical strip to a horizontal geometry, filling the additional entries with the inclusion of new strips having the same z and z' dependence almost do not require additional cost.

Table 5.5: Matrix fill times for each additional vertical strip for the probe-fed patch geometry whose top and side views are given in Fig. 5.12

Number of vertical strips	**MoM matrix fill-time for additional entries**
	Fixed Discretization (sec)
1 (Feed)	109
2	0.7
3	0.9
4	1.2
5	1.5
6	1.7
7	2.0
8	2.3
9	2.5
10	2.7
11	3.0
12	3.2
13	3.4
14	3.7
15	4.0
16	4.2

Chapter 6

Conclusions

Printed circuits or antennas over multilayer planar media with multiple vertical conductors have become quite popular to facilitate the connectivity between the circuits on different layers as well as to achieve some complex operations. Therefore, parallel to such developments in real-life applications, efficient simulation tools based on full-wave methods have attracted a great deal of interest, mainly to reduce the cost, to study different configurations, and to use with an optimization tool to achieve multi-purpose operations from a circuit or antenna. In this thesis, a computationally efficient spatial-domain MoM formulation is proposed and demonstrated for the analysis of printed geometries with multiple vertical metallization spanning more than one layer. The main contributions of the thesis can be stated as follows: the method proposed i) can efficiently analyze printed circuits with vertical conductors spanning more than one layer; and ii) can handle multiple vertical conductors with extreme efficiency, that is, the computational cost of additional vertical conductors, in addition to the cost of the analysis of a single vertical conductor, becomes almost negligible.

The method presented in this thesis for the analysis of planar multilayer geometries with vertical metallizations is based on the spatial-domain MoM in conjunction with the closed-form Green's functions for the solution of the mixed-potential integral equation (MPIE). It was already demonstrated that the use of spatial-domain Green's functions has significantly decreased the matrix-fill time, even before the use of the robust multi-level approach [26] and analytical integrations of the MoM entries [30]. However, implementing the same

method for printed circuits with vertical metallization had some difficulties, as outlined and resolved in [28]. As soon as the difficulties have been overcome, it was recognized that the method can be tailored to efficiently analyze printed circuits with more than one vertical conductor. Moreover, the same approach, with a little modification, can handle vertical conductors extending over multiple layers in a multilayer environment. To validate the assessment, a method based on MoM-DCIM is developed to analyze such structures and demonstrated over some examples. Scattering parameters and relevant circuit parameters are extracted for those examples and compared to those presented in literature and to those obtained from the commercial software *em* by SONNET. Furthermore, in order to verify the accuracy of the proposed physical model developed for the analysis of multilayer printed structures, current distributions obtained from the analysis are compared to the ones obtained from *em* by SONNET. As a final statement, the method proposed and implemented in this thesis leads to an efficient CAD simulation software for the design of microwave circuits and microstrip antennas involving multiple vertical metallization. As a possible extension of this work for future study, the method can be modified to handle slots in the ground plane, and metallization in oblique directions.

Appendix A

Derivation of MoM Matrix Entries

In the application of the spatial-domain MoM to the solution of MPIE for the analysis of planarly layered geometries, the surface current densities on the conductors are written in terms of linear combination of known basis functions and unknown amplitudes corresponding to each basis function. At the intersections of horizontal and vertical conductors, attachment functions are defined to satisfy the current continuity. After the testing procedure, the amplitudes of the current densities are found using the matrix equation given in (3.15). The general form of surface current densities for each direction can be written as follows:

$$J_x(x,y)=\sum_m\sum_n I_x^{(m,n)}B_x^{(m,n)}(x,y)+\sum_n I_{xS}^{(n)}B_{xS}^{(n)}(x,y) \tag{A.1}$$

$$J_y(x,y)=\sum_m\sum_n I_y^{(m,n)}B_y^{(m,n)}(x,y)+\sum_m I_{yS}^{(m)}B_{yS}^{(m)}(x,y) \tag{A.2}$$

$$\begin{aligned}J_z(x,y,z)=&\sum_m\sum_l I_{z(l)}^{x(m,n)}B_{z(l)}^{x(m,n)}(y,z)+\sum_m\sum_n I_{xSP}^{(m,n)}B_{xSP}^{(m,n)}(x,y)+\\&\sum_n\sum_k I_{z(k)}^{y(m,n)}B_{z(k)}^{y(m,n)}(x,z)+\sum_m\sum_n I_{ySP}^{(m,n)}B_{ySP}^{(m,n)}(x,y)\end{aligned} \tag{A.3}$$

where $B_{xS}^{(n)}$ and $B_{yS}^{(m)}$ represent the source terms in the x- and y-directions, respectively whereas $B_{xSP}^{(m,n)}$ and $B_{ySP}^{(m,n)}$ denote the horizontal attachment functions introduced at the junctions of vertical and horizontal conductors to satisfy the charge conservation in the circuit. Note that in (A.3), the first and the last two terms represent the vertical current density along the yz- and xz-spanning vertical strips. Note also that the mathematical formulations for the basis functions in the z-direction are already given in (3.14) and (3.15).

Using the definition of current densities given above and the electric field expressions, the derivation of the MoM matrix entries corresponding to horizontal and vertical metallizations are evaluated as shown in the following sections.

A.1. Z_{xx}, Z_{xy} and Z_{xz} Entries

The tangential electric field on the *x*-direction is given as below:

$$E_x = -j\omega G_{xx}^A * J_x + \frac{1}{j\omega}\frac{\partial}{\partial x}\left(G_x^q * \frac{\partial}{\partial x} J_x + G_y^q * \frac{\partial}{\partial y} J_y + G_z^q * \frac{\partial}{\partial z} J_z \right) \tag{A.4}$$

Substituting the surface current density expressions into (A.4), the following equation is obtained:

$$\begin{aligned} E_x = & -j\omega G_{xx}^A \left\{ \sum_m \sum_n I_x^{(m,n)} B_x^{(m,n)} + \sum_n I_{xS}^{(n)} B_{xS}^{(n)} \right\} \\ & + \frac{1}{j\omega}\frac{\partial}{\partial x}\left[G_x^q * \frac{\partial}{\partial x}\left\{ \sum_m \sum_n I_x^{(m,n)} B_x^{(m,n)} + \sum_n I_{xS}^{(n)} B_{xS}^{(n)} + \sum_m \sum_n I_{xSP}^{(m,n)} B_{xSP}^{(m,n)} \right\} \right] \\ & + \frac{1}{j\omega}\frac{\partial}{\partial x}\left[G_y^q * \frac{\partial}{\partial y}\left\{ \sum_m \sum_n I_y^{(m,n)} B_y^{(m,n)} + \sum_m I_{yS}^{(m)} B_{yS}^{(m)} + \sum_m \sum_n I_{ySP}^{(m,n)} B_{ySP}^{(m,n)} \right\} \right] \\ & + \frac{1}{j\omega}\frac{\partial}{\partial x}\left[G_z^q * \frac{\partial}{\partial z}\left\{ \sum_m \sum_l I_{z(l)}^{x(m,n)} B_{z(l)}^{x(m,n)} + \sum_n \sum_k I_{z(k)}^{y(m,n)} B_{z(k)}^{y(m,n)} \right\} \right] \end{aligned} \tag{A.5}$$

Although attachment functions are the components of vertical basis functions to represent the vertical current density, they are *x*- or *y*-directed horizontal saw-tooth functions. So, their derivatives should be taken over the horizontal directions. After arranging the terms, the above equation can be written as:

$$\begin{aligned} E_x = & -j\omega \sum_m \sum_n I_x^{(m,n)} \left\{ G_{xx}^A * B_x^{(m,n)} + \frac{1}{\omega^2}\frac{\partial}{\partial x}\left[G_x^q * \frac{\partial}{\partial x} B_x^{(m,n)} \right] \right\} \\ & - j\omega \sum_m \sum_n I_{xSP}^{(m,n)} \left\{ G_{xx}^A * B_{xSP}^{(m,n)} + \frac{1}{\omega^2}\frac{\partial}{\partial x}\left[G_x^q * \frac{\partial}{\partial x} B_{xSP}^{(m,n)} \right] \right\} \\ & - j\omega \sum_n I_{xS}^{(n)} \left\{ G_{xx}^A * B_{xS}^{(n)} + \frac{1}{\omega^2}\frac{\partial}{\partial x}\left[G_x^q * \frac{\partial}{\partial x} B_{xS}^{(n)} \right] \right\} + \frac{1}{j\omega} \sum_m \sum_n I_y^{(m,n)} \left\{ \frac{\partial}{\partial x}\left[G_y^q * \frac{\partial}{\partial y} B_y^{(m,n)} \right] \right\} \\ & + \frac{1}{j\omega} \sum_m \sum_n I_{ySP}^{(m,n)} \left\{ \frac{\partial}{\partial x}\left[G_y^q * \frac{\partial}{\partial y} B_{ySP}^{(m,n)} \right] \right\} + \frac{1}{j\omega} \sum_m I_{yS}^{(m)} \left\{ \frac{\partial}{\partial x}\left[G_y^q * \frac{\partial}{\partial y} B_{yS}^{(m)} \right] \right\} \\ & + \frac{1}{j\omega} \sum_m \sum_l I_{z(l)}^{x(m,n)} \left\{ \frac{\partial}{\partial x}\left[G_z^q * \frac{\partial}{\partial z} B_{z(l)}^{x(m,n)} \right] \right\} + \frac{1}{j\omega} \sum_n \sum_k I_{z(k)}^{y(m,n)} \left\{ \frac{\partial}{\partial x}\left[G_z^q * \frac{\partial}{\partial z} B_{z(k)}^{y(m,n)} \right] \right\} \end{aligned} \tag{A.6}$$

The next step is the testing of above equation with all the testing functions $T_x^{(m',n')}$ and setting the resulting equation to zero. Testing of E_x, i.e. applying boundary conditions in the integral sense on the horizontal conductor is denoted as follows:

$$\left\langle T_x^{(m',n')}, E_x \right\rangle = 0 \tag{A.7}$$

where $\langle , \rangle$ denote the inner product and its definition is given as

$$\left\langle f(x,y), g(x,y) \right\rangle = \iint dxdy f(x,y) \cdot g(x,y) \tag{A.8}$$

After testing E_x with $T_x^{(m',n')}$, the following equation is obtained

$$\begin{aligned}
0 = & \sum_m \sum_n I_x^{(m,n)} \left\{ \left\langle T_x^{(m',n')}, G_{xx}^A * B_x^{(m,n)} \right\rangle + \frac{1}{\omega^2} \left\langle T_x^{(m',n')}, \frac{\partial}{\partial x} \left[G_x^q * \frac{\partial}{\partial x} B_x^{(m,n)} \right] \right\rangle \right\} \\
& + \frac{1}{\omega^2} \sum_m \sum_n I_y^{(m,n)} \left\{ \left\langle T_x^{(m',n')}, \frac{\partial}{\partial x} \left[G_y^q * \frac{\partial}{\partial y} B_y^{(m,n)} \right] \right\rangle \right\} \\
& + \frac{1}{\omega^2} \sum_m \sum_l I_{z(l)}^{x(m,n)} \left\{ \left\langle T_x^{(m',n')}, \frac{\partial}{\partial x} \left[G_z^q * \frac{\partial}{\partial z} B_{z(l)}^{x(m,n)} \right] \right\rangle \right\} \\
& + \sum_m \sum_n I_{xSP}^{(m,n)} \left\{ \left\langle T_x^{(m',n')}, G_{xx}^A * B_{xSP}^{(m,n)} \right\rangle + \frac{1}{\omega^2} \left\langle T_x^{(m',n')}, \frac{\partial}{\partial x} \left[G_x^q * \frac{\partial}{\partial x} B_{xSP}^{(m,n)} \right] \right\rangle \right\} \\
& + \frac{1}{\omega^2} \sum_n \sum_k I_{z(k)}^{y(m,n)} \left\{ \left\langle T_x^{(m',n')}, \frac{\partial}{\partial x} \left[G_z^q * \frac{\partial}{\partial z} B_{z(k)}^{y(m,n)} \right] \right\rangle \right\} \\
& + \frac{1}{\omega^2} \sum_m \sum_n I_{ySP}^{(m,n)} \left\{ \left\langle T_x^{(m',n')}, \frac{\partial}{\partial x} \left[G_y^q * \frac{\partial}{\partial y} B_{ySP}^{(m,n)} \right] \right\rangle \right\} \\
& + \sum_n I_{xS}^{(n)} \left\{ \left\langle T_x^{(m',n')}, G_{xx}^A * B_{xS}^{(n)} \right\rangle + \frac{1}{\omega^2} \left\langle T_x^{(m',n')}, \frac{\partial}{\partial x} \left[G_x^q * \frac{\partial}{\partial x} B_{xS}^{(n)} \right] \right\rangle \right\} \\
& + \frac{1}{\omega^2} \sum_m I_{yS}^{(m)} \left\{ \left\langle T_x^{(m',n')}, \frac{\partial}{\partial x} \left[G_y^q * \frac{\partial}{\partial y} B_{yS}^{(m)} \right] \right\rangle \right\}
\end{aligned} \tag{A.9}$$

Impedance and excitation matrix entries can be extracted from the above equation. It should be noted that, unknown attachment function amplitudes are related with the amplitudes of their associated vertical half rooftop basis functions, which are defined at the horizontal and

vertical conductor intersections in order to satisfy the conservation of the charge at the junction region. Therefore their contributions are included in the Z_{xz} submatrix entries of the MoM impedance matrix. Recall that the relations between the attachment functions and the vertical basis functions at the junctions are already given in Chapter 3. To summarize, impedance and excitation matrix entries obtained due to E_x are given as follows:

$$Z_{xx}^{(m',n')(m,n)} = \left\langle T_x^{(m',n')}, G_{xx}^{A} * B_x^{(m,n)} \right\rangle + \frac{1}{\omega^2} \left\langle T_x^{(m',n')}, \frac{\partial}{\partial x} \left[G_x^q * \frac{\partial B_x^{(m,n)}}{\partial x} \right] \right\rangle \tag{A.10}$$

$$Z_{xy}^{(m',n')(m,n)} = \frac{1}{\omega^2} \left\langle T_x^{(m',n')}, \frac{\partial}{\partial x} \left[G_y^q * \frac{\partial B_y^{(m,n)}}{\partial y} \right] \right\rangle \tag{A.11}$$

$$\begin{aligned} Z_{xz}^{(m',n')(l)} = {} & \frac{1}{\omega^2} \left\langle T_x^{(m',n')}, \frac{\partial}{\partial x} \left[G_z^q * \frac{\partial B_{z(l)}^{x(m,n)}}{\partial z} \right] \right\rangle \\ & - \frac{1}{2} \left\{ \left\langle T_x^{(m',n')}, G_{xx}^{A} * B_{xSP}^{(m,n)} \right\rangle + \frac{1}{\omega^2} \left\langle T_x^{(m',n')}, \frac{\partial}{\partial x} \left[G_x^q * \frac{\partial B_{xSP}^{(m,n)}}{\partial x} \right] \right\rangle \right\} \end{aligned} \tag{A.12}$$

$$\begin{aligned} Z_{xz}^{(m',n')(k)} = {} & \frac{1}{\omega^2} \left\langle T_x^{(m',n')}, \frac{\partial}{\partial x} \left[G_z^q * \frac{\partial B_{z(k)}^{y(m,n)}}{\partial z} \right] \right\rangle \\ & - \frac{1}{2} \left\{ \frac{1}{\omega^2} \left\langle T_x^{(m',n')}, \frac{\partial}{\partial x} \left[G_y^q * \frac{\partial B_{ySP}^{(m,n)}}{\partial y} \right] \right\rangle \right\} \end{aligned} \tag{A.13}$$

$$\begin{aligned} V_x^{(m',n')(l)} = {} & -\left\langle T_x^{(m',n')}, G_{xx}^{A} * B_{xS}^{(n)} \right\rangle - \frac{1}{\omega^2} \left\langle T_x^{(m',n')}, \frac{\partial}{\partial x} \left[G_x^q * \frac{\partial}{\partial x} B_{xS}^{(n)} \right] \right\rangle \\ & - \frac{1}{\omega^2} \left\langle T_x^{(m',n')}, \frac{\partial}{\partial x} \left[G_y^q * \frac{\partial}{\partial y} B_{yS}^{(m)} \right] \right\rangle \end{aligned} \tag{A.14}$$

Note that (A.12) and (A.13) are for the basis functions on the vertical strips spanning in the *yz*- and *xz*-directions, respectively.

A.2. Z_{yx}, Z_{yy} and Z_{yz} Entries

The matrix entries obtained from E_y is derived using the same procedure followed for the derivation for the E_x case. Therefore only the resulting impedance and excitation matrix entries are given here.

$$Z_{yy}^{(m',n')(m,n)} = \left\langle T_y^{(m',n')}, G_{yy}^{A} * B_y^{(m,n)} \right\rangle + \frac{1}{\omega^2} \left\langle T_y^{(m',n')}, \frac{\partial}{\partial y} \left[G_y^q * \frac{\partial B_y^{(m,n)}}{\partial y} \right] \right\rangle \tag{A.15}$$

$$Z_{yx}^{(m',n')(m,n)} = \frac{1}{\omega^2} \left\langle T_y^{(m',n')}, \frac{\partial}{\partial y} \left[G_x^q * \frac{\partial B_x^{(m,n)}}{\partial x} \right] \right\rangle \tag{A.16}$$

$$\begin{aligned} Z_{yz}^{(m',n')(k)} = & \frac{1}{\omega^2} \left\langle T_y^{(m',n')}, \frac{\partial}{\partial y} \left[G_z^q * \frac{\partial B_{z(k)}^{y(m,n)}}{\partial z} \right] \right\rangle \\ & - \frac{1}{2} \left\{ \left\langle T_y^{(m',n')}, G_{yy}^{A} * B_{ySP}^{(m,n)} \right\rangle + \frac{1}{\omega^2} \left\langle T_y^{(m',n')}, \frac{\partial}{\partial y} \left[G_y^q * \frac{\partial B_{ySP}^{(m,n)}}{\partial y} \right] \right\rangle \right\} \end{aligned} \tag{A.17}$$

$$\begin{aligned} Z_{yz}^{(m',n')(l)} = & \frac{1}{\omega^2} \left\langle T_y^{(m',n')}, \frac{\partial}{\partial y} \left[G_z^q * \frac{\partial B_{z(l)}^{x(m,n)}}{\partial z} \right] \right\rangle \\ & - \frac{1}{2} \left\{ \frac{1}{\omega^2} \left\langle T_y^{(m',n')}, \frac{\partial}{\partial y} \left[G_x^q * \frac{\partial B_{xSP}^{(m,n)}}{\partial x} \right] \right\rangle \right\} \end{aligned} \tag{A.18}$$

$$\begin{aligned} V_y^{(m',n')(l)} = & -\left\langle T_y^{(m',n')}, G_{yy}^{A} * B_{yS}^{(m)} \right\rangle - \frac{1}{\omega^2} \left\langle T_y^{(m',n')}, \frac{\partial}{\partial y} \left[G_y^q * \frac{\partial B_{yS}^{(m)}}{\partial y} \right] \right\rangle \\ & - \frac{1}{\omega^2} \left\langle T_y^{(m',n')}, \frac{\partial}{\partial y} \left[G_x^q * \frac{\partial B_{xS}^{(n)}}{\partial x} \right] \right\rangle \end{aligned} \tag{A.19}$$

where (A.17) and (A.18) are for the basis functions on the vertical strips spanning in the *xz*- and *yz*-directions, respectively. Note that entries involving attachment functions exist only if there is a vertical and horizontal conductor intersection.

A.3. Z_{zx}, Z_{zy} and Z_{zz} Entries

Remember that the electric field representation for the analysis of planarly layered media is given as below:

$$\mathbf{E} = -j\omega\left(\overline{\mathbf{G}}^{A} * \mathbf{J}\right) - \nabla\left[G^{q} * \left(\frac{-1}{j\omega}\nabla\cdot\mathbf{J}\right)\right] \tag{A.20}$$

Substituting (A.1)-(A.3) into above equation results in the following expression:

$$\begin{aligned}
\mathbf{E} = & -j\omega\overline{\mathbf{G}}^{\mathbf{A}} * \hat{x}\left\{\sum_m\sum_n I_x^{(m,n)}B_x^{(m,n)} + \sum_n I_{xS}^{(n)}B_{xS}^{(n)} + \sum_m\sum_n I_{xSP}^{(m,n)}B_{xSP}^{(m,n)}\right\} \\
& - j\omega\overline{\mathbf{G}}^{\mathbf{A}} * \hat{y}\left\{\sum_m\sum_n I_y^{(m,n)}B_y^{(m,n)} + \sum_m I_{yS}^{(m)}B_{yS}^{(m)} + \sum_m\sum_n I_{ySP}^{(m,n)}B_{ySP}^{(m,n)}\right\} \\
& - j\omega\overline{\mathbf{G}}^{\mathbf{A}} * \hat{z}\left\{\sum_m\sum_l I_{z(l)}^{x(m,n)}B_{z(l)}^{x(m,n)} + \sum_n\sum_k I_{z(k)}^{y(m,n)}B_{z(k)}^{y(m,n)}\right\} \\
& + \frac{1}{j\omega}\frac{\partial}{\partial z}\left[G_x^q * \frac{\partial}{\partial x}\left\{\sum_m\sum_n I_x^{(m,n)}B_x^{(m,n)} + \sum_n I_{xS}^{(n)}B_{xS}^{(n)} + \sum_m\sum_n I_{xSP}^{(m,n)}B_{xSP}^{(m,n)}\right\}\right] \\
& + \frac{1}{j\omega}\frac{\partial}{\partial z}\left[G_y^q * \frac{\partial}{\partial y}\left\{\sum_m\sum_n I_y^{(m,n)}B_y^{(m,n)} + \sum_m I_{yS}^{(m)}B_{yS}^{(m)} + \sum_m\sum_n I_{ySP}^{(m,n)}B_{ySP}^{(m,n)}\right\}\right] \\
& + \frac{1}{j\omega}\frac{\partial}{\partial z}\left[G_z^q * \frac{\partial}{\partial z}\left\{\sum_m\sum_l I_{z(l)}^{x(m,n)}B_{z(l)}^{x(m,n)}(y,z) + \sum_n\sum_k I_{z(k)}^{y(m,n)}B_{z(k)}^{y(m,n)}(x,z)\right\}\right]
\end{aligned} \tag{A.21}$$

where $\overline{\mathbf{G}}^{\mathbf{A}} = G_{xx}^{A}\hat{x}\hat{x} + G_{yy}^{A}\hat{y}\hat{y} + G_{zx}^{A}\hat{z}\hat{x} + G_{zy}^{A}\hat{z}\hat{y} + G_{zz}^{A}\hat{z}\hat{z}$ is the dyadic traditional form Green's functions for vector potential. Now, test $\mathbf{E}$ with testing functions $\left(T_{z(l')}^{x(m',n')} + T_{xSP}^{(m,n)}\right)$ or $\left(T_{z(k')}^{y(m',n')} + T_{ySP}^{(m,n)}\right)$ and set the equation to zero to satisfy the boundary condition. Note that, testing functions are the same functions with the basis functions. Therefore, they are represented as a half rooftop vertical function plus its associated attachment function. Testing procedure with $\left(T_{z(l')}^{x(m',n')} + T_{xSP}^{(m,n)}\right)$ is given as the following:

$$0 = \sum_m\sum_n I_x^{(m,n)}\left\{\left\langle T_{z(l')}^{x(m',n')}, G_{zx}^{A} * B_x^{(m,n)}\right\rangle + \frac{1}{\omega^2}\left\langle T_{z(l')}^{x(m',n')}, \frac{\partial}{\partial z}\left[G_x^q * \frac{\partial}{\partial x}B_x^{(m,n)}\right]\right\rangle\right\}$$

$$
\begin{aligned}
&+\sum_m\sum_n I_x^{(m,n)}\left\{\left\langle T_{xSP}^{(m',n')},G_{xx}^A * B_x^{(m,n)}\right\rangle+\frac{1}{\omega^2}\left\langle T_{xSP}^{(m',n')},\frac{\partial}{\partial x}\left[G_x^q * \frac{\partial}{\partial x}B_x^{(m,n)}\right]\right\rangle\right\}\\
&+\sum_m\sum_n I_y^{(m,n)}\left\{\left\langle T_{z(l')}^{x(m',n')},G_{zy}^A * B_y^{(m,n)}\right\rangle+\frac{1}{\omega^2}\left\langle T_{z(l')}^{x(m',n')},\frac{\partial}{\partial z}\left[G_y^q * \frac{\partial}{\partial y}B_y^{(m,n)}\right]\right\rangle\right\}\\
&+\sum_m\sum_n I_y^{(m,n)}\left\{\frac{1}{\omega^2}\left\langle T_{xSP}^{(m',n')},\frac{\partial}{\partial x}\left[G_y^q * \frac{\partial}{\partial y}B_y^{(m,n)}\right]\right\rangle\right\}\\
&+\sum_m\sum_l I_{z(l)}^{x(m,n)}\left\{\left\langle T_{z(l')}^{x(m',n')},G_{zz}^A * B_{z(l)}^{x(m,n)}\right\rangle+\frac{1}{\omega^2}\left\langle T_{z(l')}^{x(m',n')},\frac{\partial}{\partial z}\left[G_z^q * \frac{\partial}{\partial z}B_{z(l)}^{x(m,n)}\right]\right\rangle\right\}\\
&+\sum_m\sum_n I_{xSP}^{(m,n)}\left\{\left\langle T_{z(l')}^{x(m',n')},G_{zx}^A * B_{xSP}^{(m,n)}\right\rangle+\frac{1}{\omega^2}\left\langle T_{z(l')}^{x(m',n')},\frac{\partial}{\partial z}\left[G_x^q * \frac{\partial}{\partial x}B_{xSP}^{(m,n)}\right]\right\rangle\right\}\\
&+\sum_m\sum_l I_{z(l)}^{x(m,n)}\left\{\frac{1}{\omega^2}\left\langle T_{xSP}^{(m',n')},\frac{\partial}{\partial x}\left[G_z^q * \frac{\partial}{\partial z}B_{z(l)}^{x(m,n)}\right]\right\rangle\right\}\\
&+\sum_m\sum_n I_{xSP}^{(m,n)}\left\{\left\langle T_{xSP}^{(m',n')},G_{xx}^A * B_{xSP}^{(m,n)}\right\rangle+\frac{1}{\omega^2}\left\langle T_{xSP}^{(m',n')},\frac{\partial}{\partial x}\left[G_x^q * \frac{\partial}{\partial x}B_{xSP}^{(m,n)}\right]\right\rangle\right\}\\
&+\sum_n\sum_k I_{z(k)}^{y(m,n)}\left\{\left\langle T_{z(l')}^{x(m',n')},G_{zz}^A * B_{z(k)}^{y(m,n)}\right\rangle+\frac{1}{\omega^2}\left\langle T_{z(l')}^{x(m',n')},\frac{\partial}{\partial z}\left[G_z^q * \frac{\partial}{\partial z}B_{z(k)}^{y(m,n)}\right]\right\rangle\right\}\\
&+\sum_m\sum_n I_{ySP}^{(m,n)}\left\{\left\langle T_{z(l')}^{x(m',n')},G_{zy}^A * B_{ySP}^{(m,n)}\right\rangle+\frac{1}{\omega^2}\left\langle T_{z(l')}^{x(m',n')},\frac{\partial}{\partial z}\left[G_y^q * \frac{\partial}{\partial y}B_{ySP}^{(m,n)}\right]\right\rangle\right\}\\
&+\sum_n\sum_k I_{z(k)}^{y(m,n)}\left\{\frac{1}{\omega^2}\left\langle T_{xSP}^{(m',n')},\frac{\partial}{\partial x}\left[G_z^q * \frac{\partial}{\partial z}B_{z(k)}^{y(m,n)}\right]\right\rangle\right\}\\
&+\sum_m\sum_n I_{xSP}^{(m,n)}\left\{\frac{1}{\omega^2}\left\langle T_{xSP}^{(m',n')},\frac{\partial}{\partial x}\left[G_y^q * \frac{\partial}{\partial y}B_{ySP}^{(m,n)}\right]\right\rangle\right\}\\
&+\sum_n I_{xS}^{(n)}\left\{\left\langle T_{z(l')}^{x(m',n')},G_{zx}^A * B_{xS}^{(n)}\right\rangle+\frac{1}{\omega^2}\left\langle T_{z(l')}^{x(m',n')},\frac{\partial}{\partial z}\left[G_x^q * \frac{\partial}{\partial x}B_{xS}^{(n)}\right]\right\rangle\right\}\\
&+\sum_n I_{xS}^{(n)}\left\{\left\langle T_{xSP}^{(m',n')},G_{xx}^A * B_{xS}^{(n)}\right\rangle+\frac{1}{\omega^2}\left\langle T_{xSP}^{(m',n')},\frac{\partial}{\partial x}\left[G_x^q * \frac{\partial}{\partial x}B_{xS}^{(n)}\right]\right\rangle\right\}\\
&+\sum_m I_{yS}^{(m)}\left\{\left\langle T_{z(l')}^{x(m',n')},G_{zy}^A * B_{yS}^{(m)}\right\rangle+\frac{1}{\omega^2}\left\langle T_{z(l')}^{x(m',n')},\frac{\partial}{\partial z}\left[G_y^q * \frac{\partial}{\partial y}B_{yS}^{(m)}\right]\right\rangle\right\}\\
&+\sum_m I_{yS}^{(m)}\left\{\frac{1}{\omega^2}\left\langle T_{xSP}^{(m',n')},\frac{\partial}{\partial x}\left[G_y^q * \frac{\partial}{\partial y}B_{yS}^{(m)}\right]\right\rangle\right\}
\end{aligned}
\tag{A.22}
$$

Using the relations between the attachment functions and the vertical basis functions at the junctions those are already given in Chapter 3, the matrix entries are obtained as

$$Z_{zx}^{x(m',n')(m,n)} = \left\langle T_{z(l')}^{x(m',n')}, G_{zx}^{A} * B_{x}^{(m,n)} \right\rangle + \frac{1}{\omega^2}\left\langle T_{z(l')}^{x(m',n')}, \frac{\partial}{\partial z}\left[G_{x}^{q} * \frac{\partial B_{x}^{(m,n)}}{\partial x} \right] \right\rangle$$
$$-\frac{1}{2}\left\{ \left\langle T_{xSP}^{(m',n')}, G_{xx}^{A} * B_{x}^{(m,n)} \right\rangle + \frac{1}{\omega^2}\left\langle T_{xSP}^{(m',n')}, \frac{\partial}{\partial x}\left[G_{x}^{q} * \frac{\partial}{\partial x} B_{x}^{(m,n)} \right] \right\rangle \right\} \tag{A.23}$$

$$Z_{zy}^{x(m',n')(m,n)} = \left\langle T_{z(l')}^{x(m',n')}, G_{zy}^{A} * B_{y}^{(m,n)} \right\rangle + \frac{1}{\omega^2}\left\langle T_{z(l')}^{x(m',n')}, \frac{\partial}{\partial z}\left[G_{y}^{q} * \frac{\partial}{\partial y} B_{y}^{(m,n)} \right] \right\rangle$$
$$-\frac{1}{2}\left\{ \frac{1}{\omega^2}\left\langle T_{xSP}^{(m',n')}, \frac{\partial}{\partial x}\left[G_{y}^{q} * \frac{\partial}{\partial y} B_{y}^{(m,n)} \right] \right\rangle \right\} \tag{A.24}$$

$$Z_{zz}^{x(m',n')x(m,n)} = \left\langle T_{z(l')}^{x(m',n')}, G_{zz}^{A} * B_{z(l)}^{x(m,n)} \right\rangle + \frac{1}{\omega^2}\left\langle T_{z(l')}^{x(m',n')}, \frac{\partial}{\partial z}\left[G_{z}^{q} * \frac{\partial}{\partial z} B_{z(l)}^{x(m,n)} \right] \right\rangle$$
$$-\frac{1}{2}\left\{ \left\langle T_{z(l')}^{x(m',n')}, G_{zx}^{A} * B_{xSP}^{(m,n)} \right\rangle + \frac{1}{\omega^2}\left\langle T_{z(l')}^{x(m',n')}, \frac{\partial}{\partial z}\left[G_{x}^{q} * \frac{\partial}{\partial x} B_{xSP}^{(m,n)} \right] \right\rangle \right\}$$
$$-\frac{1}{2}\left\{ \frac{1}{\omega^2}\left\langle T_{xSP}^{(m',n')}, \frac{\partial}{\partial x}\left[G_{z}^{q} * \frac{\partial}{\partial z} B_{z(l)}^{x(m,n)} \right] \right\rangle \right\}$$
$$+\frac{1}{4}\left\{ \left\langle T_{xSP}^{(m',n')}, G_{xx}^{A} * B_{xSP}^{(m,n)} \right\rangle + \frac{1}{\omega^2}\left\langle T_{xSP}^{(m',n')}, \frac{\partial}{\partial x}\left[G_{x}^{q} * \frac{\partial}{\partial x} B_{xSP}^{(m,n)} \right] \right\rangle \right\} \tag{A.25}$$

$$Z_{zz}^{x(m',n')y(m,n)} = \left\langle T_{z(l')}^{x(m',n')}, G_{zz}^{A} * B_{z(k)}^{y(m,n)} \right\rangle + \frac{1}{\omega^2}\left\langle T_{z(l')}^{x(m',n')}, \frac{\partial}{\partial z}\left[G_{z}^{q} * \frac{\partial}{\partial z} B_{z(k)}^{y(m,n)} \right] \right\rangle$$
$$-\frac{1}{2}\left\{ \left\langle T_{z(l')}^{x(m',n')}, G_{zy}^{A} * B_{ySP}^{(m,n)} \right\rangle + \frac{1}{\omega^2}\left\langle T_{z(l')}^{x(m',n')}, \frac{\partial}{\partial z}\left[G_{y}^{q} * \frac{\partial}{\partial y} B_{ySP}^{(m,n)} \right] \right\rangle \right\}$$
$$-\frac{1}{2}\left\{ \frac{1}{\omega^2}\left\langle T_{xSP}^{(m',n')}, \frac{\partial}{\partial x}\left[G_{z}^{q} * \frac{\partial}{\partial z} B_{z(k)}^{y(m,n)} \right] \right\rangle \right\}$$
$$+\frac{1}{4}\left\{ \frac{1}{\omega^2}\left\langle T_{xSP}^{(m',n')}, \frac{\partial}{\partial x}\left[G_{y}^{q} * \frac{\partial}{\partial y} B_{ySP}^{(m,n)} \right] \right\rangle \right\} \tag{A.26}$$

$$
\begin{aligned}
V_z^{x(m',n')(m,n)} = & -\left\langle T_{z(l')}^{x(m',n')}, G_{zx}^{A} * B_{xS}^{(n)} \right\rangle - \frac{1}{\omega^2}\left\langle T_{z(l')}^{x(m',n')}, \frac{\partial}{\partial z}\left[G_x^q * \frac{\partial}{\partial x} B_{xS}^{(n)} \right] \right\rangle \\
& -\left\langle T_{z(l')}^{x(m',n')}, G_{zy}^{A} * B_{yS}^{(m)} \right\rangle + \frac{1}{\omega^2}\left\langle T_{z(l')}^{x(m',n')}, \frac{\partial}{\partial z}\left[G_y^q * \frac{\partial}{\partial y} B_{yS}^{(m)} \right] \right\rangle \\
& + \frac{1}{2}\left\{ \left\langle T_{xSP}^{(m',n')}, G_{xx}^{A} * B_{xS}^{(n)} \right\rangle + \frac{1}{\omega^2}\left\langle T_{xSP}^{(m',n')}, \frac{\partial}{\partial x}\left[G_x^q * \frac{\partial}{\partial x} B_{xS}^{(n)} \right] \right\rangle \right\} \\
& + \frac{1}{2}\left\{ \frac{1}{\omega^2}\left\langle T_{xSP}^{(m',n')}, \frac{\partial}{\partial x}\left[G_y^q * \frac{\partial}{\partial y} B_{yS}^{(m)} \right] \right\rangle \right\}
\end{aligned} \tag{A.27}
$$

Note that (A.25) and (A.26) are for the basis functions on the vertical strips spanning in the *yz*- and *xz*-directions, respectively.

The above matrix entries are for the testing functions $T_{z(l')}^{x(m',n')}$ and $T_{xSP}^{(m',n')}$. When the matrix entries for the testing functions $T_{z(k')}^{y(m',n')}$ and $T_{ySP}^{(m',n')}$ are required, it is enough to replace $T_{z(l')}^{x(m',n')}$ and associated attachment testing function $T_{xSP}^{(m',n')}$ with the testing function $T_{z(k')}^{y(m',n')}$ and its associated attachment testing function $T_{ySP}^{(m',n')}$, respectively.

Appendix B

Analytical Evaluations of the Inner Product Terms

The general formulation for the spatial domain MoM by using the aforementioned basis and testing functions is demonstrated in Chapter 3. The MoM entries of the formulation, which are represented in terms of inner products, are given in Appendix A. Now in this appendix, the evaluation of inner product terms corresponding to implementation of vertical metallizations will be given.

B.1. Evaluation of $\left\langle \frac{\partial}{\partial z} T_z, G_x^q * \frac{\partial}{\partial x} B_x \right\rangle$

For this inner product term, integration and derivation with respect to z should be handled. The evaluation for $T_z(y, z)$ starts by writing the inner product term explicitly as

$$\left\langle \frac{\partial}{\partial z} T_z(y,z), G_x^q * \frac{\partial}{\partial x} B_x(x,y) \right\rangle = \iint dz dy \frac{\partial}{\partial z} T_z(y,z) \cdot \iint dx' dy' G_x^q(x-x', y-y', z, z') \frac{\partial}{\partial x'} B_x(x', y') \tag{B.1}$$

Using the separability of functions and after a bit of manipulation this equation becomes

$$\left\langle \frac{\partial}{\partial z} T_z(y,z), G_x^q * \frac{\partial}{\partial x} B_x(x,y) \right\rangle = \iint dx' dy' \frac{\partial}{\partial x'} B_x(x', y') \cdot \int dy T_z(y) \int dz \frac{\partial}{\partial z} T_z(z) G_x^q(x-x', y-y', z, z') \tag{B.2}$$

The innermost integral in (B.2) is taken by using the method explained in Chapter 3 by writing the spatial domain Green's function in terms of its spectral domain counterpart. The innermost integral results in the auxiliary function

$$F_x^q \overset{def}{=} \int dz \frac{\partial}{\partial z} T_z(z) \frac{1}{4\pi} \int_{SIP} dk_\rho k_\rho H_0^{(2)}\left(k_\rho |\rho - \rho'|\right) \tilde{G}_x^q\left(k_\rho, z, z' = cons\right)$$
$$\cong \frac{1}{4\pi} \int_{SIP} dk_\rho k_\rho H_0^{(2)}\left(k_\rho |\rho - \rho'|\right) \cdot GPOF\left\{ \int dz \frac{\partial}{\partial z} T_z(z) \tilde{G}_x^q\left(k_\rho, z, z' = cons\right) \right\} \tag{B.3}$$

where $\tilde{G}_x^q$ is the spectral domain Green's function. Spatial-domain auxiliary function is obtained with the exponential approximation of the innermost integration in (B.3). After the substitution of the spatial-domain auxiliary function in (B.2), the equation becomes

$$\left\langle \frac{\partial}{\partial z} T_z(y,z), G_x^q * \frac{\partial}{\partial x} B_x(x,y) \right\rangle = \int dy T_z(y) \iint dx' dy' F_x^q(x-x', y-y', z') \frac{\partial}{\partial x'} B_x(x', y') \quad \text{(B.4)}$$

Then by making the substitutions $x - x' = u$ and $y - y' = v$, the following expression is obtained:

$$\left\langle \frac{\partial}{\partial z} T_z(y,z), G_x^q * \frac{\partial}{\partial x} B_x(x,y) \right\rangle = -\iint du dv F_x^q(u,v,z') \int dy T_z(y) \frac{\partial}{\partial u} B_x(x-u, y-v) \quad \text{(B.5)}$$

where x is the x-coordinate of the vertical strip. Similarly, for the testing function on the xz-spanning vertical strip, $T_z(x, z)$, this inner product can be written as

$$\left\langle \frac{\partial}{\partial z} T_z(x,z), G_x^q * \frac{\partial}{\partial x} B_x(x,y) \right\rangle = -\iint du dv F_x^q(u,v,z') \int dx T_z(x) \frac{\partial}{\partial u} B_x(x-u, y-v) \quad \text{(B.6)}$$

where y is the y-coordinate of the vertical strip. Similar approach can be used in case of the basis function is a y-directed horizontal rooftop function.

B.2. Evaluation of $\left\langle T_z, G_{zx}^A * B_x \right\rangle$

This term involves integration over z direction. For the testing functions on the yz-spanning vertical strip, the inner product becomes

$$\left\langle T_z(y,z), G_{zx}^A * B_x(x,y) \right\rangle = \iint dz dy T_z(y,z) \iint dx' dy' G_{zx}^A(x-x', y-y', z, z') B_x(x', y') \quad \text{(B.7)}$$

Then this equation can be rearranged using the separability of functions as

$$\left\langle T_z(y,z), G_{zx}^A * B_x(x,y) \right\rangle = \int dy T_z(y) \iint dx' dy' B_x(x', y') \int dz T_z(z) G_{zx}^A(x-x', y-y', z, z') \quad \text{(B.8)}$$

To evaluate the innermost integral, a new auxiliary function is defined:

$$F_{zx}^A \overset{def}{=} \int dz T_z(z) \frac{1}{4\pi} \int_{SIP} dk_\rho k_\rho H_0^{(2)}(k_\rho |\rho - \rho'|) \frac{\tilde{G}_{zx}^A(k_\rho, z, z' = cons)}{-jk_x}$$

$$\cong \frac{1}{4\pi}\int_{SIP} dk_\rho k_\rho H_0^{(2)}\left(k_\rho\left|\rho-\rho'\right|\right)\cdot GPOF\left\{\int dz T_z(z)\frac{\tilde{G}_{zx}^A\left(k_\rho, z, z'=cons\right)}{-jk_x}\right\} \qquad \text{(B.9)}$$

Spectral-domain $\tilde{G}_{zx}^A$ is divided by $-jk_x$ to eliminate the multiplicative $-jk_x$ term existing in the explicit formulation of the Green's function $\tilde{G}_{zx}^A$. Therefore its effect is added as the derivative with respect to x' in the spatial domain representation. Then inner product becomes

$$\left\langle T_z(y,z), G_{zx}^A * B_x(x,y)\right\rangle = -\int dy T_z(y)\iint dx'dy' B_x(x',y')\frac{\partial}{\partial x'}F_{zx}^A(x-x', y-y', z') \qquad \text{(B.10)}$$

The following chain rule is applied to (B.10) as

$$\frac{\partial}{\partial x'}\left[B_x(x',y')F_{zx}^A\right] = \frac{\partial}{\partial x'}B_x(x',y')F_{zx}^A + B_x(x',y')\frac{\partial}{\partial x'}F_{zx}^A \qquad \text{(B.11)}$$

and the inner product is rewritten as

$$\begin{aligned}\left\langle T_z(y,z), G_{zx}^A * B_x(x,y)\right\rangle = &-\int dy T_z(y)\int dy'\left[B_x(x',y')F_{zx}^A(x-x', y-y', z')\right]\Big|_{x'\in\Omega_B} \\ &+\int dy T_z(y)\iint dx'dy' F_{zx}^A(x-x', y-y', z')\frac{\partial}{\partial x'}B_x(x',y')\end{aligned} \qquad \text{(B.12)}$$

where Ω_B is the boundary of the domain of the basis function. Then by making the substitutions $x-x'=u$ and $y-y'=v$, the following expression is obtained:

$$\begin{aligned}\left\langle T_z(y,z), G_{zx}^A * B_x(x,y)\right\rangle = &\int dv F_{zx}^A(u,v,z')\int dy\left[T_z(y)B_x(x-u, y-v)\right]\Big|_{x'\in\Omega_B} \\ &+\int du dv F_{zx}^A(u,v,z')\int dy T_z(y)\frac{\partial}{\partial x'}B_x(x-u, y-v)\end{aligned} \qquad \text{(B.13)}$$

where x is the x-coordinate of the yz-spanning vertical strip. Similarly, for the testing function on the xz- spanning vertical strip, $T_z(x, z)$, this inner product can be written as

$$\begin{aligned}\left\langle T_z(x,z), G_{zx}^A * B_x(x,y)\right\rangle = &\int dv F_{zx}^A(u,v,z')\int dx\left[T_z(x)B_x(x-u, y-v)\right]\Big|_{y'\in\Omega_B} \\ &+\int du dv F_{zx}^A(u,v,z')\int dx T_z(x)\frac{\partial}{\partial x'}B_x(x-u, y-v)\end{aligned} \qquad \text{(B.14)}$$

where y is the y-coordinate of the xz-spanning vertical strip.

B.3. Evaluation of $\left\langle \frac{\partial}{\partial x} T_x, G_z^q * \frac{\partial}{\partial z} B_z \right\rangle$

In this term, integration and derivation with respect to z' should be taken. The evaluation for the basis function on the vertical strip $B_z(y, z)$ starts by writing

$$\left\langle \frac{\partial}{\partial x} T_x(x,y), G_z^q * \frac{\partial}{\partial z} B_z(y,z) \right\rangle = \iint dxdy \frac{\partial}{\partial x} T_x(x,y) \cdot \iint dz'dy' G_z^q(x-x', y-y', z, z') \frac{\partial}{\partial z'} B_z(y', z') \tag{B.15}$$

After a little bit of manipulation this equation becomes

$$\left\langle \frac{\partial}{\partial x} T_x(x,y), G_z^q * \frac{\partial}{\partial z} B_z(y,z) \right\rangle = \iint dxdy \frac{\partial}{\partial x} T_x(x,y) \cdot \int dy' B_z(y') \int dz' \frac{\partial}{\partial z'} B_z(z') G_z^q(x-x', y-y', z, z') \tag{B.16}$$

The innermost integral is written in terms of the following auxiliary function

$$F_z^q \overset{def}{=} \int dz' \frac{\partial}{\partial z'} B_z(z') \frac{1}{4\pi} \int_{SIP} dk_\rho k_\rho H_0^{(2)}(k_\rho |\rho - \rho'|) \tilde{G}_z^q(k_\rho, z = cons, z') \cong \frac{1}{4\pi} \int_{SIP} dk_\rho k_\rho H_0^{(2)}(k_\rho |\rho - \rho'|) \cdot GPOF\left\{ \int dz' \frac{\partial}{\partial z'} B_z(z') \tilde{G}_z^q(k_\rho, z = cons, z') \right\} \tag{B.17}$$

After the substitution of the auxiliary functions in (B.16), the equation becomes

$$\left\langle \frac{\partial}{\partial x} T_x(x,y), G_z^q * \frac{\partial}{\partial z} B_z(y,z) \right\rangle = \int dy' B_z(y') \iint dxdy F_z^q(x-x', y-y', z) \frac{\partial}{\partial x} T_x(x,y) \tag{B.18}$$

Then by making the substitutions $x - x' = u$ and $y - y' = v$, the following is obtained:

$$\left\langle \frac{\partial}{\partial x} T_x(x,y), G_z^q * \frac{\partial}{\partial z} B_z(y,z) \right\rangle = \iint dudv F_z^q(u,v,z) \int dy B_z(y-v) \frac{\partial}{\partial x} T_x(x'+u, y) \tag{B.19}$$

where x' is the x-coordinate of the yz-spanning basis function. Similarly, for the basis function $B_z(x, z)$ the inner product can be expressed as follows:

$$\left\langle \frac{\partial}{\partial x} T_x(x,y), G_z^q * \frac{\partial}{\partial z} B_z(x,z) \right\rangle = \iint dudv F_z^q(u,v,z) \int dx B_z(x-u) \frac{\partial}{\partial x} T_x(x, y'+v) \tag{B.20}$$

where y' is the y-coordinate of the xz-spanning basis function.

B.4. Evaluation of $\left\langle T_z, G_{zz}^A * B_z \right\rangle$

This term involves integration in both z and z' directions. For the yz-spanning testing and basis functions, the inner product can be written as

$$\left\langle T_z(y,z), G_{zz}^A * B_z(y,z) \right\rangle = \iint dzdy T_z(y,z) \iint dz'dy' G_{zz}^A(x-x', y-y', z, z') B_z(y', z') \tag{B.21}$$

Then after manipulating the above equation, the following is obtained

$$\left\langle T_z(y,z), G_{zz}^A * B_z(y,z) \right\rangle = \int dy T_z(y) \int dy' B_z(y') \iint dzdz' T_z(z) B_z(z') G_{zz}^A(x-x', y-y', z, z') \tag{B.22}$$

The following auxiliary function is defined to evaluate the innermost integral in (B.22):

$$\begin{aligned} F_{zz}^A &\overset{def}{=} \int dzdz' T_z(z) B_z(z') \frac{1}{4\pi} \int_{SIP} dk_\rho k_\rho H_0^{(2)}\left(k_\rho |\rho - \rho'|\right) \tilde{G}_{zz}^A(k_\rho, z, z') \\ &\cong \frac{1}{4\pi} \int_{SIP} dk_\rho k_\rho H_0^{(2)}\left(k_\rho |\rho - \rho'|\right) \cdot GPOF\left\{ \iint dzdz' T_z(z) B_z(z') \tilde{G}_{zz}^A(k_\rho, z, z') \right\} \end{aligned} \tag{B.23}$$

After substituting the auxiliary function into (B.22), the inner product term reduces to

$$\left\langle T_z(y,z), G_{zz}^A * B_z(y,z) \right\rangle = \int dy T_z(y) \int dy' B_z(y') F_{zz}^A(x-x', y-y') \tag{B.24}$$

where x and x' are the x-coordinates of the testing and basis functions respectively. By making the substitution $y - y' = v$, the following expression is obtained:

$$\left\langle T_z(y,z), G_{zz}^A * B_z(y,z) \right\rangle = \int dv F_{zz}^A(u,v) \int dy' T_z(y'+v) B_z(y') \tag{B.25}$$

Similarly for testing function $T_z(x, z)$ and basis function $B_z(x, z)$, the inner product is

$$\left\langle T_z(x,z), G_{zz}^A * B_z(x,z) \right\rangle = \int du F_{zz}^A(u,v) \int dx' T_z(x') B_z(x'+u) \tag{B.26}$$

where y and y' are the y-coordinates of the testing and basis functions respectively. Likewise, for testing function $T_z(x, z)$ and basis function $B_z(y, z)$, the inner product is

$$\left\langle T_z(x,z), G_{zz}^A * B_z(y,z) \right\rangle = \iint dudv F_{zz}^A(u,v) T_z(x'+u) B_z(y-v) \tag{B.27}$$

where x' is the x-coordinate of the basis function whereas y is the y-coordinate of the testing function. Finally, the inner product for testing function $T_z(y, z)$ and basis function $B_z(x, z)$ is given as follows:

$$\left\langle T_z(y,z), G_{zz}^A * B_z(x,z) \right\rangle = \iint dudv F_{zz}^A(u,v) T_z(y'+v) B_z(x-u) \tag{B.28}$$

where y' is the y-coordinate of the basis function and x is the x-coordinate of the testing function.

B.5. Evaluation of $\left\langle \frac{\partial}{\partial z} T_z, G_z^q * \frac{\partial}{\partial z} B_z \right\rangle$

This term involves integration and derivation with respect to both z and z'. For the yz-spanning testing and basis functions, the evaluation starts by writing

$$\left\langle \frac{\partial}{\partial z} T_z(y,z), G_z^q * \frac{\partial}{\partial z} B_z(y,z) \right\rangle = \iint dz dy \frac{\partial}{\partial z} T_z(y,z) \cdot \iint dz' dy' G_z^q(x-x', y-y', z, z') \frac{\partial}{\partial z'} B_z(y', z') \tag{B.29}$$

After a little bit of manipulation, this equation can be expressed as:

$$\left\langle \frac{\partial}{\partial z} T_z(y,z), G_z^q * \frac{\partial}{\partial z} B_z(y,z) \right\rangle = \int dy T_z(y) \int dy' B_z(y') \cdot \iint dz dz' \frac{\partial}{\partial z} T_z(z) \frac{\partial}{\partial z'} B_z(z') G_z^q(x-x', y-y', z, z') \tag{B.30}$$

The innermost integral is written as the following auxiliary function

$$F_z^q \overset{def}{=} \int dz dz' \frac{\partial}{\partial z} T_z(z) \frac{\partial}{\partial z'} B_z(z') \frac{1}{4\pi} \int_{SIP} dk_\rho k_\rho H_0^{(2)}\left(k_\rho |\rho - \rho'|\right) \tilde{G}_z^q(k_\rho, z, z')$$
$$\cong \frac{1}{4\pi} \int_{SIP} dk_\rho k_\rho H_0^{(2)}\left(k_\rho |\rho - \rho'|\right) \cdot GPOF\left\{ \iint dz dz' \frac{\partial}{\partial z} T_z(z) \frac{\partial}{\partial z'} B_z(z') \tilde{G}_z^q(k_\rho, z, z') \right\} \tag{B.31}$$

Then by substituting the auxiliary function into (B.30), the inner product term is obtained as

$$\left\langle \frac{\partial}{\partial z} T_z(y,z), G_z^q * \frac{\partial}{\partial z} B_z(y,z) \right\rangle = \int dy T_z(y) \int dy' B_z(y') F_z^q(x-x', y-y') \tag{B.32}$$

where x and x' are the x-coordinates of the testing and basis functions respectively. By making the substitution $y - y' = v$, the following equation is obtained:

$$\left\langle \frac{\partial}{\partial z} T_z(y,z), G_z^q * \frac{\partial}{\partial z} B_z(y,z) \right\rangle = \int dv F_z^q(u,v) \int dy' T_z(y'+v) B_z(y') \tag{B.33}$$

Similarly for testing function $T_z(x, z)$ and basis function $B_z(x, z)$, the inner product becomes

$$\left\langle \frac{\partial}{\partial z} T_z(x,z), G_z^q * \frac{\partial}{\partial z} B_z(x,z) \right\rangle = \int du F_z^q(u,v) \int dx' T_z(x') B_z(x'+u) \tag{B.34}$$

where y and y' are the y-coordinates of the testing and basis functions respectively. And for the testing function $T_z(x, z)$ and basis function $B_z(y, z)$, the inner product is

$$\left\langle \frac{\partial}{\partial z} T_z(x,z), G_z^q * \frac{\partial}{\partial z} B_z(y,z) \right\rangle = \iint du dv F_z^q(u,v) T_z(x'+u) B_z(y-v) \tag{B.35}$$

where x' is the x-coordinate of the basis function whereas y is the y-coordinate of the testing function. Finally, the inner product for testing function $T_z(y, z)$ and basis function $B_z(x, z)$ is given as follows:

$$\left\langle \frac{\partial}{\partial z} T_z(y,z), G_z^q * \frac{\partial}{\partial z} B_z(x,z) \right\rangle = \iint du dv F_z^q(u,v) T_z(y'+v) B_z(x-u) \tag{B.36}$$

where y' is the y-coordinate of the basis function and x is the x-coordinate of the testing function.

B.6. Other Terms

Evaluation of the terms involving basis functions in the y-direction or attachment functions and source functions are similar to the ones discussed in this appendix. The only difference is the definition of the functions. Therefore they are not shown here.

Appendix C

Effective Dielectric Constant of Rectangular Patch Antennas

For a single layer microstrip patch antenna with the physical width *W*, physical length *L*, thickness *h*, dielectric constant ε_r, and strip conductor thickness *t*, the following frequency-dependent formulas are used for the calculation of effective dielectric constant [56]. The effective dielectric constant $\varepsilon_{eff}(f)$ as a function of frequency is computed using the following expressions:

$$\varepsilon_{\text{eff}}(f) = \varepsilon_r - [(\varepsilon_r - \varepsilon_{\text{eff}}(0))/(1+P)] \tag{C.1}$$

where $\varepsilon_{\text{eff}}(0)$ is the static effective dielectric constant, and is given by:

$$\varepsilon_{\text{eff}}(0) = \frac{1}{2}[\varepsilon_r + 1 + (\varepsilon_r - 1)G] \tag{C.2}$$

$$G = (1+10h/W)^{-AB} - \left[(\ln 4/\pi)\cdot\left(t\cdot(Wh)^{-1/2}\right)\right] \tag{C.3}$$

$$A = 1 + \frac{1}{49}\ln\left[\frac{(W/h)^4 + W^2/(52h)^2}{(W/h)^4 + 0.432}\right] + \frac{1}{18.7}\ln\left[1 + (W/18.1h)^3\right] \tag{C.4}$$

$$B = 0.564\exp[-0.2/(\varepsilon_r + 0.3)] \tag{C.5}$$

and

$$P = P_1 P_2 [(0.1844 + P_3 P_4) f_n]^{1.5763} \tag{C.6}$$

with

$$P_1 = 0.27488 + \left[0.6315 + \left\{0.525/(1+0.0157 f_n)^{20}\right\}\right]u - 0.065683\exp(-8.7513u)$$

$$P_2 = 0.33622[1 - \exp(-0.03442\varepsilon_r)]$$

$$P_3 = 0.0363\exp(-4.6u)\left\{1 - \exp\left[-(f_n/38.7)^{4.97}\right]\right\}$$

$$P_4 = 1 + 2.751\left\{1 - \exp\left[-(\varepsilon_r/15.916)^8\right]\right\}$$

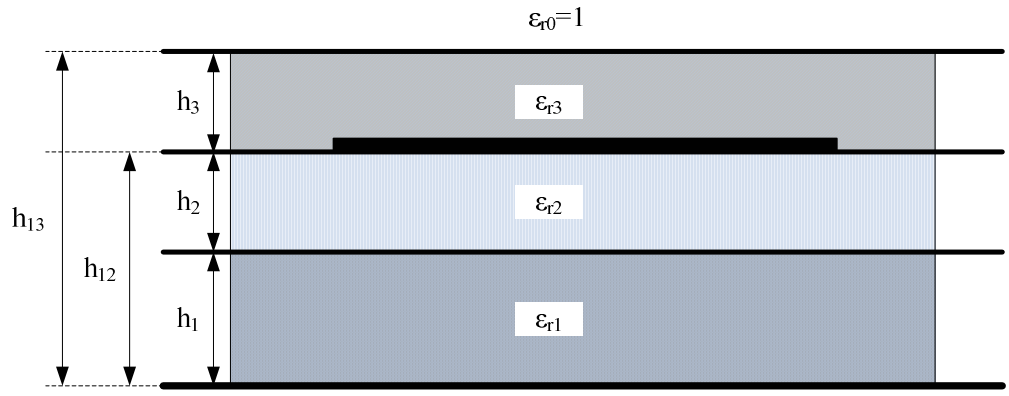

Figure C.1: A multilayer rectangular microstrip antenna

$$f_n = 47.713kh, \qquad \text{where } k = 2\pi/\lambda_0$$

$$u = \left[W + (dW - W)/\varepsilon_r\right]/h$$

$$dW = W + \frac{t}{\pi}\left[1 + \ln\left\{\frac{4}{(t/h)^{1/2}} + \frac{(1/\pi)^2}{(W/t + 1.1)^2}\right\}\right].$$

In the design of microstrip patches with multidielectric layers, as shown in Fig. C.1, the following relation for the quasistatic effective permittivity is used [57]:

$$\varepsilon_{eff} = \varepsilon_{r1}\varepsilon_{r2}\frac{(q_1 + q_2)^2}{\varepsilon_{r1}q_2 + \varepsilon_{r2}q_1} + \varepsilon_{r3}\frac{(1 - q_1 - q_2)^2}{\varepsilon_{r3}(1 - q_1 - q_2 - q_3) + q_3} \tag{C.7}$$

where q_1, q_2 and q_3 are expressed for a wide microstrip line ($W/h_{21} \geq 1$) as

$$q_1 = \frac{h_1}{2h_{12}}\left\{1 + \frac{\pi}{4} - \frac{h_{12}}{W_e}\ln\left[\frac{2W_e}{h_1}\sin\left(\frac{\pi h_1}{2h_{12}}\right) + \cos\left(\frac{\pi h_1}{2h_{12}}\right)\right]\right\},$$

$$q_2 = 1 - q_1 - \frac{h_{12}}{2W_e}\ln\left(\frac{\pi W_e}{h_{12}} - 1\right),$$

$$q_3 = 1 - q_1 - q_2 - \frac{h_{12} - v_e}{2W_e}\ln\left[\frac{2W_e}{2h_{13} - h_{12} + v_e}\cos\left(\frac{\pi v_e}{2h_{12}}\right) + \sin\left(\frac{\pi v_e}{2h_{12}}\right)\right]$$

in which the effective line width W_e and the quantity v_e are given by

$$W_e = W + \frac{2h_{12}}{\pi}\ln\left(17.08\left(\frac{W}{2h_{12}} + 0.92\right)\right),$$

$$v_e = \frac{2h_{12}}{\pi}\tan^{-1}\left[\frac{2\pi}{\pi W_e - 4h_{12}}\left(h_{13} - h_{12}\right)\right].$$

It should be noted that the dispersive behaviour of the effective dielectric constant is neglected in this calculation and one can refer [57] for the contribution of dispersion in the evaluation of effective dielectric constant.

BIBLIOGRAPHY

[1] J. R. James, and G. Andrasic, "Multifunction printed antennas," in *Advances in Microstrip and Printed Antennas*. , Kai Fong Lee and Wei Chen, Eds., John Wiley & Sons Inc., N.Y., 1997.

[2] Christian Johansson, Steffen Uhlig, Ola Tageman, Arne Alping, Joacim Haglund, Mats Robertsson, Michael Popall, and Lothar Frhlich, "Microwave Circuits in Multilayer Inorganic-Organic Polymer Thin Film Technology on Laminate Substrates," *IEEE Trans. Adv. Packag.*, vol. 26, pp. 81–89, Feb. 2003.

[3] Shahrooz Shahparnia and Omar M. Ramahi, "Electromagnetic Interference (EMI) Reduction From Printed Circuit Boards (PCB) Using Electromagnetic Bandgap Structures," *IEEE Trans. Electromagn. Compat.*, vol. 46, pp. 580–587, Nov. 2004.

[4] Chen Wang, Marco Leone, James L. Drewniak, and Antonio Orlandi, "Coupling Between Differential Signals and the DC Power-Bus in Multilayer PCBs," *IEEE Trans. Adv. Packag.*, vol. 28, pp. 337–345, May 2005.

[5] G. DeJean, R. Bairavasubramanian, D. Thompson, G. E. Ponchak, M. M. T entzeris, and J. Papapolymerou, "Liquid Crystal Polymer (LCP): A New Organic Material for the Development of Multilayer Dual-Frequency/Dual-Polarization Flexible Antenna Arrays," *IEEE Antennas Wireless Propagat. Lett.*, vol. 4, pp. 22–26, 2005.

[6] Tomohiro Seki, Naoki Honma, Kenjiro Nishikawa, and Kouichi Tsunekawa, "Millimeter-Wave High-Efficiency Multilayer Parasitic Microstrip Antenna Array on Teflon Substrate," *IEEE Trans. on Microwave Theory Tech.*, vol. 53, pp. 2101–2106, June 2005.

[7] N. Herscovici, "A wide-band single-layer patch antenna," *IEEE Trans. Antennas Propagat.*, Vol. 46, pp. 471-474, Apr. 1998.

[8] N. Herscovici, ”New Considerations in the design of microstrip antennas,” *IEEE Trans. Antennas Propagat.*, Vol. 46, pp. 807-812, June 1998.

[9] P. Silvester and P. Benedek, “Equivalent capacitance of microstrip open circuits,” *IEEE Trans. on Microwave Theory Tech.*, vol. 20, pp. 511–516, August 1972.

[10] ——, “Equivalent capacitance of microstrip gaps and steps,” *IEEE Trans. on Microwave Theory Tech.*, vol. 20, pp. 729–733, Nov. 1972.

[11] ——, “Equivalent discontinuities capacitances for right-angle bends, t-junctions and crossings,” *IEEE Trans. on Microwave Theory Tech.*, vol. 21, pp. 341–346, May 1973.

[12] R. F. Harrington, “Matrix methods for field problems,” *IEEE Proceedings*, vol. 55, pp. 136–149, Feb. 1967.

[13] ——, *Field Computation by Moment Methods*. The Macmillan Company, 1968.

[14] K. Kunz and R. Luebber, *The Finite Difference Time Domain method for Electomagnetics*. Boca Raton, FL: CRC press, 1993.

[15] J. Jin, *The Finite Element Method in Electomagnetics*. Newyork: John Wiley & Sons, Inc., 1993.

[16] M. J. Tsai, F. D. Flavis, O. Fordharn, and N. G. Alexopoulos, “Modeling planar arbitrarily shaped microstrip elements in multilayered media,” *IEEE Trans. on Microwave Theory Tech.*, vol. 45, pp. 330–337, March 1997.

[17] M. R. Abdul-Gaffoor, H. K. Smith, A. A. Kishk, and A. W. Glisson, “Simple and efficient full-wave modeling of electromagnetic coupling in realistic RF multilayer PCB layouts,” *IEEE Trans. Antennas Propagat.*, vol. 50, pp. 1445–1457, June 2002.

[18] J. Yeo and R. Mittra, “An algorithm for interpolating the frequency variations of method-of-moments matrices arising in the analysis of planar microstrip structures,” *IEEE Trans. on Microwave Theory Tech.*, vol. 51, pp. 1018–1025, March 2003.

[19] E. A. Soliman, M. H. Bakr, and N. K. Nikolova, “Neural networks-method of moments (NN-MoM) for the efficient filling of the coupling matrix,” *IEEE Trans. on Antennas and Propagation*, vol. 52, pp. 1521–1529, June 2004.

[20] J. R. Mosig and F. E. Gardiol, "General integral equation formulation for microstrip antennas and scatterers," *IEE Proceedings*, vol. 132, no. 7, pp. 424–432, December 1985.

[21] Juan R. Mosig, "Arbitrarily shaped microstrip structures and their analysis with a mixed potential integral equation," *IEEE Trans. on Microwave Theory Tech.*, vol. MTT-36, no. 2, pp. 314–323, Feb. 1988.

[22] K. A. Michalski and D. Zheng, "Electromagnetic scattering and radiation by surfaces of arbitrary shape in layered media, part 1: Theory," *IEEE Trans. Antennas Propagat.*, vol. 38, pp. 335–344, March 1990.

[23] Y. L. Chow, J. J. Yang, D. G. Fang, and G. E. Howard, "A closed-form spatial green's function for the thick microstrip substrate," *IEEE Trans. on Microwave Theory Tech.*, vol. 39, pp. 588–592, March 1991.

[24] M. I. Aksun and R. Mittra, "Derivation of closed-form green's functions for a general microstrip geometry," *IEEE Trans. on Microwave Theory Tech.*, vol. 40, pp. 2055–2062, Nov. 1992.

[25] G. Dural and M. I. Aksun, "Closed-form green's functions for general sources and stratified media," *IEEE Trans. on Microwave Theory Tech.*, vol. 43, pp. 1545–1552, July 1995.

[26] M. I. Aksun, "A robust approach for the derivation of closed-form green's functions," *IEEE Trans. on Microwave Theory Tech.*, vol. 44, no. 5, pp. 651–658, May 1996.

[27] M. I. Aksun and R. Mittra, "Estimation of spurious radiation from microstrip etches using closed-form green's functions," *IEEE Trans. on Microwave Theory Tech.*, vol. 40, pp. 2063–2069, November 1992.

[28] N. Kınayman and M. I. Aksun, "Efficient and accurate em simulation technique for analysis and design of mmics," *Int. J. MIMICAE*, vol. 7, pp. 344–358, September 1997.

[29] M. I. Aksun and G. Dural, "Clarification of Issues on the Closed-Form Green's Functions in Stratified Media," Accepted for publication in *IEEE Trans. on Antennas and Propagation*, Nov. 2005.

[30] L. Alatan, M. I. Aksun, K. Mahadevan, M. T. Birand, "Analytical evaluation of the mom matrix elements," *IEEE Trans. on Microwave Theory Tech.*, vol. 44, pp. 519–525, Apr 1996.

[31] Noyan Kınayman and M. I. Aksun, EMPLAN: Electromagnetic Analysis of Printed Structures in Planarly Layered Media, Artech House Publisher, 2000.

[32] M. I. Aksun and R. Mittra, "Efficient use of closed-form Green's functions for three-dimensional problems involving multilayered media," in Digest *IEEE AP-S Int. Symp.*, vol. 2, pp. 1354–1357, June 1994.

[33] K. A. Michalski and J. R. Mosig, "Discrete complex image MPIE analysis of coax-fed coupled vertical monopoles in grounded dielectric substrate: two formulations," *IEE Proceedings Microwaves, Antennas and Propagation*, Vol. 142, pp. 269–274, June 1995.

[34] Michalski, K.A.; Mosig, J.R., "Discrete complex image mixed-potential integral equation analysis of microstrip patch antennas with vertical probe feeds," *Electromagnetics*, Vol. 15, pp. 377–392, July/Aug. 1995.

[35] N. Kınayman and M. I. Aksun, "Efficient use of closed-form green's functions for the analysis of planar geometries with vertical connections," *IEEE Trans. on Microwave Theory Tech.*, vol. 45, pp. 593–603, May 1997.

[36] Yaxun Liu, Le-Wei Li, Tat-Soon Yeo, Mook-Seng Leong, "Application of DCIM to MPIE-MoM analysis of 3D PEC objects in multilayered media," *IEEE Trans. on Antennas Propagat.*, vol. 50, pp. 157–162, Feb. 2002.

[37] Feng Ling, Jian Liu and Jian-Ming Jin, "Efficient electromagnetic modeling of three-dimensional multilayer microstrip antennas and circuits," *IEEE Trans. on Microwave Theory Tech.*, vol. 50, pp. 1628–1635, June 2002.

[38] T. M. Grzegorczyk and J. R. Mosig, "Full-wave analysis of antennas containing horizontal and vertical metallizations embedded in planar multilayered media," *IEEE Trans. on Antennas Propagat.*, vol. 51, pp. 3047–3054, Nov. 2003.

[39] K. A. Michalski, "On the scalar potential of a point charge associated with a time-harmonic dipole in a layered medium," *IEEE Trans. on Microwave Theory Tech.*, vol. 35, no. 5, pp. 1299-1301, Nov 1987.

[40] W. C. Chew, *Waves and Fields in Inhomogeneous Media*. Van Nostrad Reinhold, 1990.

[41] A. Sommerfeld, *Partial Differential Equations in Physics*. New York: Academic, 1949.

[42] N. Kınayman, *A Novel CAD Algorithm for the Analysis of Printed Geometries*. PhD Thesis, Graduate College of the Bilkent University, Ankara, Turkey, 1997.

[43] Noyan Kınayman and M. I. Aksun, *Modern Microwave Circuits*. Boston: Artech House, Inc., 2005.

[44] J. R. Mosig and F. E. Gardiol, "Analytical and numerical techniques in the green's function treatment of microstrip antennas and scatterers," *IEE Proceedings*, vol. 130, pp. 175–182, Mar. 1983.

[45] Y. Hua and T. K. Sarkar, "Generalized pencil-of-function method for extracting poles of an EM system from its transient response," *IEEE Trans. Antennas Propagat.*, vol. 37, pp. 229-234, Feb. 1989.

[46] N. Kınayman and M. I. Aksun, "Efficient use of closed-form green's functions for the analysis of planar geometries with vertical connections," *IEEE Trans. on Microwave Theory Tech.*, vol. 45, pp. 593-603, May 1997.

[47] George V. Eleftheriades and Juan R. Mosig, "On the network characterization of planar passive circuits using the method of moments," *IEEE Trans. on Microwave Theory Tech.*, vol. 44, pp. 438-445, March 1996.

[48] S. S. Inc., *Sonnet User Guide*, 2003.

[49] S. Mutlu, *Hybrid Model for Probe-fed Rectangular Microstrip Antennas with Shorting Strips*. MS Thesis, Graduate College of the Bilkent University, Ankara, Turkey, 2001.

[50] D. H. Schaubert, D. M. Pozar and A. Adrian, "Effect of microstrip antenna substrate thickness and permittivity: Comparison of theories with experiment," *IEEE Trans. on Antennas Propagat.*, vol. 37, no. 6, pp. 677-682, June 1989.

[51] K. R. Carver and J. W. Mink, "Microstrip antenna technology," *IEEE Trans. on Antennas Propagat.*, vol. 29, pp. 2-24, Jan. 1981.

[52] D. M. Pozar, "Consideration for millimeter wave printed antennas," *IEEE Trans. on Antennas Propagat.*, vol. 31, pp. 740-747, Sept. 1983.

[53] K. A. Michalski and D. Zheng, "Electromagnetic scattering and radiation by surfaces of arbitrary shape in layered media, part 2: Implementation and results for contiguous half-spaces," *IEEE Trans. Antennas Propagat.*, vol. 38, pp. 345–352, March 1990.

[54] P. Gay-Balmaz and Juan R. Mosig, "Three-dimensional planar radiating structures in stratified media," Int. J. Microwave Millimeter-Wave Comput.-Aided Eng., vol. 7, pp. 330-343, Sep. 1997.

[55] K. Naishadham and P. Misra, "Order recursive gaussian elimination and efficient cad of microwave circuits," *IEEE Proceedings MTT-S International Microwave Symposium*, vol. 3, pp. 1435{1438, Orlando, May 16-20, 1995.

[56] K. P. Ray, and G. Kumar, "Determination of the resonant frequency of microstrip antennas," *Microwave Opt. Technol. Lett*., Vol. 23, pp. 114-117, 20 Oct. 1999.

[57] Shun-Shi Zhong, Gang Liu, Ghulam Qasim, "Closed form expressions for resonant frequency of rectangular patch antennas with multidielectric layers," *IEEE Trans. Antennas Propagat.*, Vol. 42, pp. 1360-1363, Sept. 1994.

VITA

Tayyar ÖNAL was born in Konya, Turkey on September 28, 1982. He received the B. Sc. Degree in Electrical and Electronics Engineering from Bilkent University, Ankara, 2003. In October 2003, he joined to the Electrical and Computer Engineering Department of Koç University, Istanbul, Turkey as a teaching and research assistant. His research area includes numerical analysis of printed structures, microwave and millimeter circuits, and microstrip antennas.